AFRL-AFOSR-JP-TR-2018-0023

Ga- and N-polar GaN Growths on SiC Substrate

Chih-Chung Yang
NATIONAL TAIWAN UNIVERSITY

03/15/2018
Final Report

Air Force Research Laboratory
AF Office Of Scientific Research (AFOSR)/ IOA
Arlington, Virginia 22203
Air Force Materiel Command

REPORT DOCUMENTATION PAGE

Form Approved
OMB No. 0704-0188

1. REPORT DATE *(DD-MM-YYYY)*	2. REPORT TYPE	3. DATES COVERED *(From - To)*
15-03-2018	Final	30 Sep 2014 to 29 Sep 2017

4. TITLE AND SUBTITLE
Ga- and N-polar GaN Growths on SiC Substrate

5a. CONTRACT NUMBER

5b. GRANT NUMBER
FA2386-14-1-4105

5c. PROGRAM ELEMENT NUMBER
61102F

6. AUTHOR(S)
Chih-Chung Yang

5d. PROJECT NUMBER

5e. TASK NUMBER

5f. WORK UNIT NUMBER

7. PERFORMING ORGANIZATION NAME(S) AND ADDRESS(ES)
NATIONAL TAIWAN UNIVERSITY
1, ROOSEVELT RD., SEC. 4
TAIPEI CITY, 10617 TW

8. PERFORMING ORGANIZATION REPORT NUMBER

9. SPONSORING/MONITORING AGENCY NAME(S) AND ADDRESS(ES)
AOARD
UNIT 45002
APO AP 96338-5002

10. SPONSOR/MONITOR'S ACRONYM(S)
AFRL/AFOSR IOA

11. SPONSOR/MONITOR'S REPORT NUMBER(S)
AFRL-AFOSR-JP-TR-2018-0023

12. DISTRIBUTION/AVAILABILITY STATEMENT
A DISTRIBUTION UNLIMITED: PB Public Release

13. SUPPLEMENTARY NOTES

14. ABSTRACT
The growth of a two-section, core-shell, InGaN/GaN quantum-well (QW) nanorod- (NR-) array light-emitting diode device based on a pulsed growth technique with metalorganic chemical vapor deposition (MOCVD) is demonstrated. A two-section n-GaN NR is grown through a tapering process for forming two uniform NR sections of different cross-sectional sizes. The cathodoluminescence (CL), photoluminescence (PL), and electrolumines-cence (EL) characterization results of the two-section NR structure are compared with those of a single-section NR sample, which is prepared under the similar condition to that for the first uniform NR section of the two-section sample. All the CL, PL, and EL spectra of the two-section sample (peaked between 520 and 525 nm) are red-shifted from those of the single-section sample (peaked around 490 nm) by >30 nm in wavelength. Also, the emitted spectral widths of the two-section sample become significantly larger than their counterparts of the single-section sample. The PL spectral full-width at half-maximum increases from ~37 to ~61 nm. Such variations are attributed to the higher indium incorporation in the sidewall QWs of the two-section sample due to the stronger strain relaxation in an NR section of a smaller cross-sectional size and the more constituent atom supply from the larger gap volume between neighboring NRs.

15. SUBJECT TERMS
nanotechnology, GaN, Coalescence overgrowth

16. SECURITY CLASSIFICATION OF:			17. LIMITATION OF ABSTRACT	18. NUMBER OF PAGES	19a. NAME OF RESPONSIBLE PERSON
a. REPORT	b. ABSTRACT	c. THIS PAGE			KNOPP, JEREMY
Unclassified	Unclassified	Unclassified	SAR	53	19b. TELEPHONE NUMBER *(Include area code)* 315-227-7006

Standard Form 298 (Rev. 8/98)
Prescribed by ANSI Std. Z39.18

Final Report for AOARD Grant AOARD 144105
"Ga- and N-polar GaN Growths on SiC Substrate"

November 13, 2017

PI: Chih-Chung (C. C.) Yang, ccycc@ntu.edu.tw
Graduate Institute of Photonics and Optoelectronics,
National Taiwan University, No. 1, Section 4, Roosevelt Road, 10617
Taipei, Taiwan

Period of Performance: 09/30/14 – 09/29/17

Abstract:

The growth of a two-section, core-shell, InGaN/GaN quantum-well (QW) nanorod- (NR-) array light-emitting diode device based on a pulsed growth technique with metalorganic chemical vapor deposition (MOCVD) is demonstrated. A two-section n-GaN NR is grown through a tapering process for forming two uniform NR sections of different cross-sectional sizes. The cathodoluminescence (CL), photoluminescence (PL), and electrolumines-cence (EL) characterization results of the two-section NR structure are compared with those of a single-section NR sample, which is prepared under the similar condition to that for the first uniform NR section of the two-section sample. All the CL, PL, and EL spectra of the two-section sample (peaked between 520 and 525 nm) are red-shifted from those of the single-section sample (peaked around 490 nm) by >30 nm in wavelength. Also, the emitted spectral widths of the two-section sample become significantly larger than their counterparts of the single-section sample. The PL spectral full-width at half-maximum increases from ~37 to ~61 nm. Such variations are attributed to the higher indium incorporation in the sidewall QWs of the two-section sample due to the stronger strain relaxation in an NR section of a smaller cross-sectional size and the more constituent atom supply from the larger gap volume between neighboring NRs.

The growth of regularly-patterned multi-section GaN NR arrays based on a pulsed growth technique with MOCVD is demonstrated. Such an NR with multiple sections of different cross-sectional sizes is formed by tapering a uniform cross section to another through the decrease of Ga supply duration stepwise for reducing the size of the catalytic Ga droplet. Contrast line structures are observed in either a scanning electron microscopy or a transmission electron microscopy image of an NR. Such a contrast line-marker corresponds to a thin Ga-rich layer formed at the beginning of GaN precipitation of a pulsed-growth cycle and illustrates the boundary between two successive growth cycles in pulsed growth. By analyzing the geometry variation of the contrast line-markers, the morphology evolution in the growth of a multi-section NR, including a tapering process, can be traced. Such a morphology variation is controlled by the size of the catalytic Ga droplet and its coverage range on the slant facets at the top of an NR. The comparison of emission spectrum between single-, two-, and three-section GaN NRs with sidewall InGaN/GaN QWs indicates that a multi-section NR can lead to a significantly broader sidewall emission spectrum.

A theoretical model for the growth process of a GaN NR based on the combined effect of vapor-liquid-solid (VLS) and vapor-solid (VS) modes in pulsed growth with MOCVD is proposed and formulated. In particular, the VS-growth mechanism for forming the gallium-rich line-markers, which provide us with the growth chronology of an NR, is proposed by introducing an incubation time for surface deposition. The evolutions of gallium-droplet base radius and aspect ratio and the increase of precipitated GaN volume during a transition process of a two-section NR are formulated and numerically studied to show the consistent results with experimental data. The relative contributions of the VLS and VS growths in such a transition process are also numerically illustrated. Besides, the experimentally observed decrease of the slant-facet angle from the {1-102}- to {1-101}-plane is modeled, formulated, and numerically simulated. In fitting the numerical results with experimental data, a few important kinetic parameters can be determined.

The anti-reflection functions of a surface nanostructure, including transparent conductive Ga-doped ZnO (GaZnO) nanoneedles (NNs), a GaZnO thin film, and buried Ag nanoparticles (NPs), on GaN and Si templates through the combination of the effects of gradient effective refractive index, index matching, and the surface plasmon (SP) resonances in the visible and infrared ranges are studied by

measuring its reflection, transmission, and scattering behaviors. The NNs are grown under different molecular beam epitaxy conditions with the low-temperature vapor-liquid-solid mode by using Ag NPs as growth catalyst. Based on the crystal structure study, it is found that the c-axis of a GaZnO NN is controlled by the local Ag (111) orientation of the un-melted portion of an Ag NP, which is influenced by the crystal structure of the growth template. On c-plane GaN, by using small and separate Ag NPs as catalyst, the alignment of GaN (002), Ag (111), and ZnO (002) leads to the growth of mostly vertical NNs for producing a strong anti-reflection effect. On Si (100), no crystal matching condition can be used such that the grown NNs are randomly oriented, leading to a relatively weaker anti-reflection effect. The GaZnO thin film and buried Ag NPs also make contributions to the anti-reflection function through the effects of index matching and SP resonance.

Keywords: GaN nanorod, pulsed growth, vapor-liquid-solid mode, vapor-solid mode, gallium droplet, InGaN/GaN quantum well, GaZnO nanoneedle, solar cell

Table of contents:

Chapter 1: Multi-section core-shell InGaN/GaN quantum-well nanorod light-emitting diode array

1. Introduction

The widely claimed advantageous features of a core-shell nitride nanorod (NR) light-emitting diode (LED) array include the dislocation-free GaN growth of NR, the larger effective emission area from the NR sidewalls, and the emission from the non-polar or semi-polar InGaN/GaN quantum wells (QWs) on the sidewalls and slant facets for minimizing the quantum-confined Stark effect (QCSE) [1-15]. Besides these features, the usually observed broad emission spectrum from such an NR-LED array represents an important property for the application of multi-color or white-light emission without using any phosphor [5, 6, 10, 16, 17]. The broad emission from the sidewall QWs in a core-shell NR structure can be attributed to the non-uniform distributions of QW structure and indium content on a sidewall, which are caused by the non-uniform supply of the constituent atoms at different heights in the gap volume between neighboring NRs [6]. It can also be due to the non-uniform strain relaxation condition on the sidewall of an NR such that indium incorporation efficiency for forming QWs varies along height on a sidewall. Strain relaxation is expected to be stronger in an NR of a smaller cross-sectional size. To increase the spectral variation range of the sidewall-QW emission in a core-shell NR LED, a multi-section NR of different cross-sectional sizes in different sections is a useful structure. In such a multi-section NR, the smaller cross-sectional size in an upper uniform section can lead to stronger strain relaxation for further increasing indium incorporation in sidewall-QW growth. Also, the reduced NR cross-sectional size can increase the gap volume size to accommodate more constituent atoms for sidewall-QW growth. The growth of a multi-section NR relies on the formation of a tapering section for reducing the cross-sectional size of the NR. More specifically, a hexagonal flat top-face of a size smaller than the cross section of the NR needs to be formed for the growth of the next section. Recently, based on a pulsed growth technique, this research team has successfully grown regularly-patterned, multi-section GaN NR arrays. After the growth of an NR of a uniform cross section based on the pulsed growth technique with constant supply durations of groups III and V sources, the supply duration of group III source is stepwise decreased for reducing the NR cross-sectional size. After this tapering process, a constant supply duration of group III source is resumed for forming the second uniform section of a smaller cross-sectional size.

In this chapter, we demonstrate the significant red-shift and broadening of emission spectrum of a two-section, core-shell, InGaN/GaN QW NR-LED array by comparing its performance with that of a single-section NR-LED array. The overall NR heights of the single- and two-section NR-LED samples are about the same. A two-section NR consists of four portions, including two uniform sections of different cross sectional sizes, a tapering section in between, and a pyramidal structure at the top. A single-section NR consists of two portions, including a uniform NR section and a pyramidal structure at the top. Three periods of InGaN/GaN QW are formed only on the *m*-plane NR sidewalls in both samples. Cathodoluminescence (CL) and photoluminescence (PL) measurements are undertaken for showing the consistent QW emission behaviors with that of electroluminescence (EL) measurement. In section 2 of this chapter, the NR growth and device fabrication procedures are presented. Then, the results of basic optical characterizations, including CL and PL measurements, are reported in section 3. Next, the LED performances of the NR samples are compared in section 4. Discussions are made in section 5. Finally, conclusions are drawn in section 6.

2. Nanorod growth and device fabrication

The growth of the regularly-patterned NR-LED samples starts with the formation of n-GaN NRs on an n-GaN template, which consists of a SiO_2 mask with a triangularly-arranged hole pattern. The hole diameter and hole array pitch are 350 and 1200 nm, respectively. The thickness of the SiO_2 mask is 80 nm. During the formation of n-GaN NRs, the growth temperature, TMGa, NH_3, and silane flow rates in the used metalorganic chemical vapor deposition (MOCVD) reactor are 1035 ^oC, 15 sccm, 500 sccm, and 12 sccm, respectively. The patterned holes are first filled with n-GaN through a continuous growth process of 30 sec in duration. The out-extended n-GaN NRs are formed through pulsed growth processes. For the single-section NR-LED array sample (sample S), the n-GaN NRs are formed by switching the TMGa and NH_3 flows on and off alternatively with the TMGa and NH_3 flow durations at 20 and 30 sec, respectively. A growth pause of 1 sec in duration right after a TMGa supply half-cycle is applied. The pulsed growth of n-GaN for 32 cycles leads to an NR height of 1530 nm in sample S. To avoid the growth of an InGaN/GaN QW structure on the NR top, a pointed pyramidal structure is formed at the top through a tapering-growth process by stepwise decreasing the duration of TMGa supply at 15

sec for 3 cycles, 10 sec for 3 cycle, and 5 sec for 20 cycles while the NH_3 supply duration is fixed at 30 sec. In this tapering process, the silane flow is turned off such that a pyramidal structure of un-doped GaN is formed at the top of each n-GaN NR. Figure 1(a) shows the tilted scanning electron microscopy (SEM) image of the n-GaN NR-core array of sample S. The pointed pyramidal structure can avoid the formation of a *c*-plane QW at the top. Also, because the growth rate on the slant facets ({1-101}-plane) of the pyramidal structure is very low, no *r*-plane QW is formed during the growth of sidewall *m*-plane QWs [17]. In other words, with the pyramidal structure, only the non-polar QWs can be formed in such an LED for minimizing the QCSE. The growth of un-doped GaN in the pyramidal structure can also increase the local resistance and hence minimize the injected current flow through this portion [17].

For the two-section NR-LED array sample (sample T), the condition for growing the n-GaN NR-core of sample S is used for forming the first NR section with the growth cycle number reduced to 15. Then, a tapering process is undertaken by stepwise reducing the TMGa supply duration at 15 sec for 3 cycles, 10 sec for 3 cycles, and 5 sec for 8 cycles. Again, the NH_3 supply and pause durations are fixed. After the tapering process, the pulsed growth with the constant TMGa supply duration at 20 sec is resumed for 15 cycles to form the second uniform NR section of n-GaN. In growing the second uniform NR section, the TMGa flow rate is reduced to 10.5 sccm. The NR-core growth of sample T is completed by forming an un-doped GaN pyramidal structure at the top following the same growth procedure as that for sample S. Figure 1(d) shows the tilted SEM image of the n-GaN NR-core array of sample T. Here, one can clearly see the smaller cross-sectional size in the second uniform NR section.

After the NR cores are completed, three periods of InGaN/GaN QW are deposited with the two-dimensional growth mode. Before QW deposition, the n-GaN NR arrays are dipped into buffer oxide etchant (BOE) for 15 sec to remove the thin SiN_x layer formed on NR sidewalls [18]. The SiN_x layer is formed during the n-GaN growth with a high silane flow rate. This SiN_x layer can actually hinder sidewall growth and accelerate the along-NR-axis growth. However, it needs to be removed for sidewall QW deposition. The BOE dipping duration (15 sec) is chosen for completely removing the sidewall SiN_x layer while preserving a certain SiO_2-mask thickness for minimizing current leakage in LED operation. The growth temperatures for the InGaN well and GaN barrier layers are 680 and 870 degrees, respectively. As discussed earlier, the design of the NR-core results in the growth of only *m*-plane QWs on the NR sidewalls. The QW-NR structures before p-GaN deposition are used for CL and PL measurements. The LED structures are completed by depositing a p-GaN layer on the sidewalls at the growth temperature of 960 degrees. Figures 1(b) and 1(e) show the tilted SEM images of the NR-LED arrays of samples S and T, respectively. Here, we can see that the contrast of the cross-section size between the two uniform sections becomes smaller in sample T after the depositions of the QWs and p-GaN layer. In other words, the layer thicknesses of the QWs and p-GaN are larger in the second uniform NR section, when compared with the first uniform section. Next, in a molecular beam epitaxy (MBE) reactor, a conformal, highly-conductive, Ga-doped ZnO (GaZnO) layer is deposited on the NRs at 200 ^oC in substrate temperature to serve as the transparent conductor for guiding injected current from the top to the NR sidewalls [16, 17, 19]. The GaZnO layer is thick enough to connect the neighboring NRs. Before depositing GaZnO, a copper grid with the opening size of 50 μm x 50 μm is placed on the top of an NR array to serve as the hard mask for forming the LED mesas. Figures 1(c) and 1(f) show the tilted SEM images of samples S and T, respectively, after GaZnO deposition. LED process is completed after depositing a layer of Ti (200 nm in thickness) and then a layer of Au (600 nm in thickness) on the top to serve as the p-contact. Also, the n-contact is formed in a region of exposed n-GaN-template surface with 10-nm Ti and 40-nm Au.

Figure 2(a) shows the transmission electron microscopy (TEM) image of an NR of LED sample T. Here, dashed lines are plotted to roughly indicate the boundaries of different materials. We can see that QWs and p-GaN are formed only on the NR sidewalls confirming the low growth rate on the {1-101} slant facets of the top pyramidal structure. The asymmetric GaZnO-layer thickness in the TEM image can be attributed to the removal of certain GaZnO regions left to the NR during TEM sample preparation with a focused-ion beam. This result can also be due to an unexpected atom flow pattern for depositing GaZnO in the MBE chamber. Figures 2(b)-2(d) show the magnified TEM images in the regions indicated by the three dotted-line squares. Here, one can clearly see the three QWs on the sidewalls of the two uniform NR sections as indicated by the (pink) arrows. As shown in Fig. 2(c), on the sidewall of the tapering section between the two uniform sections, the QW structure is unclear. However, a certain InGaN structure may exist. From the TEM image in Fig. 2(a), we can evaluate the surface area of the active region (the QW area on the sidewall) in an LED device of sample T. By reasonably assuming that the NR is roughly bisected for showing the TEM image in Fig. 2(a), we can estimate the lateral width and height of a rectangular sidewall in the first uniform section of the n-GaN

NR-core of sample T to give ~300 and ~510 nm, respectively. Also, those of a rectangular sidewall in the second uniform section are estimated to give ~220 and ~860 nm, respectively. Meanwhile, a trapezoidal sidewall in the tapering section has the upper and lower widths of ~220 and ~300 nm, respectively, and the height of ~187 nm. Based on those estimated scales, we can evaluate the total sidewall area of an n-GaN NR-core. This sidewall area is used for approximating the QW surface area on an NR. By multiplying this QW surface area on an NR by the NR density (0.8012 μm^{-2}) and the mesa area (2500 μm^2), we can obtain the total QW surface area of an LED device in sample T to give 4696 μm^2. A similar evaluation can be applied to sample S with a rectangular sidewall of ~300 and ~1530 nm in width and height, respectively, to give 5516 μm^2 in the total QW surface area of an LED device.

3. Optical characterization results

Figure 3(a) shows the cross-sectional SEM image of a QW-NR array of sample S with height at ~1.86 μm. Three locations for local CL spectral measurements are marked as 1-3. The CL spectra with the spatial resolution of 40 nm x 30 nm at these locations are shown in Fig. 3(b). Here, the spectral peaks of QW emission at locations 1-3 are 496, 488, and 486 nm, respectively. Because the excitation depths of the n-GaN core and hence the CL emission intensities of GaN are about the same at different sidewall locations, the spectra in Fig. 3(b) are normalized with respect to the individual peak levels of GaN around 366 nm. Here, we can see that the QW emission intensity is the highest at location 2, which is at the middle height on the NR sidewall, followed by that at locations 1 and then 3. The emission of the QWs near the NR bottom is quite weak. The difference of CL spectral peak wavelength between locations 1 and 3 in sample S is 10 nm. The spectrum peaked at 488 nm labeled by "Cross-section" in Fig. 3(b) shows the result of overall sidewall-QW emission. It is obtained by using a large electron beam of about 2.25 μm × 3 μm in size for excitation. Figure 4(a) shows the cross-sectional SEM image of a QW-NR array of sample T with height at ~1.81 μm. Here, locations 1-3 at about the same heights as those in Fig. 3(a) are marked for local CL measurements. Locations 1 and 2 are on the sidewall of the second uniform NR section while location 3 lies on the sidewall of the first uniform section. Location 4 on the tapering section is also marked for CL measurement. Figure 4(b) shows five CL spectra for locations 1-4 and the whole sidewall-QW emission in sample T, which are all normalized with respect to their individual GaN peak levels around 366 nm. The spectral peak wavelengths for locations 1-3 are 530, 514, and 492 nm, respectively, indicating the longer emission wavelengths and the larger spectral difference between the QW portions near the NR top and bottom, when compared with sample S. The difference in spectral peak wavelength between locations 1 and 3 is as large as 38 nm in sample T (only 10 nm in sample S). The spectral peak of the emission from the whole sidewall QWs is 520 nm. Regarding the CL spectrum taken at location 4, the emission is weak and its peak is unclear, confirming the unclear QW structure on the sidewall of the tapering section in sample T. Figures 5(a) and 5(b) show the panchromatic, cross-sectional CL-mapping images of samples S and T, respectively, overlaid on the individual cross-sectional SEM images. Here, we can see that the emission of sample S is generally stronger than that of sample T. In both samples, the top and middle portions of an NR emit more strongly, when compared with the bottom portion. In sample T, the tapering section is essentially dark. It is noted that in Fig. 5(a), although the top and middle portions may look equally bright in CL emission, the middle portion is actually brighter as indicated by the normalized spectral intensity shown in Fig. 3(b).

Figure 6 shows the PL spectra of the two samples at 10 and 300 K. The PL measurement is excited by a 405-nm InGaN laser diode from the sapphire-substrate side of both QW-NR samples at 6 mW in power. The PL spectral peaks of sample S (T) at 10 and 300 K are 470.7 and 490.9 nm (501.4 and 522.1 nm), respectively. At both temperatures, the PL spectral peak of sample T is red-shifted by more than 30 nm from that of sample S. Also, the spectral full-width at half-maximum (FWHM) is increased from 34.1 nm in sample S to 60.2 nm in sample T (from 36.6 nm in sample S to 61.1 nm in sample T) at 10 (300) K. Figure 7 shows the variations of normalized PL intensity (the left ordinate) and PL spectral peak energy (the right ordinate) with temperature of the two QW-NR samples. From the variations of normalized PL intensity, we can evaluate the internal quantum efficiencies to give 19.6 and 14.3 % for samples S and T, respectively. The monotonically decreasing PL spectral peak energy in both samples indicates that their behaviors of carrier localization are weak [20, 21].

4. Characterization results of light-emitting diode arrays

Figure 8 shows the relations between injected current density and applied voltage (J-V curves) of the two NR-LED samples. The current density is obtained via dividing the injected current by the

sidewall active area discussed in section 2 for both samples. Here, one can see that the leakage currents under reverse bias up to -5 V are small in both samples (1.07 and 0.97 A/cm^2 for samples S and T, respectively, at -5 V). The turn-on voltages for both samples are around 3 V. The device resistance levels of samples S and T are 154 and 195 Ω, respectively. The large resistance levels of the devices are due to their smaller active areas. The device resistivity, which is defined as the product of the active area with device resistance, of sample S (T) is 8.49 x 10^{-3} (9.15 x 10^{-3}) Ω-cm^2. These device resistivity levels are slightly smaller than that of another single-section NR-LED array (1.09 x 10^{-2} Ω-cm^2) published earlier by the same group [17]. All of them are smaller than that of a planar *c*-plane LED (1.33 x 10^{-2} Ω-cm^2), indicating the reasonable electrical properties in the fabricated NR-LED arrays. The insets of Fig. 8 show the photographs of lit devices of samples S and T when the applied voltage is 8 V.

Figure 9 shows the normalized output intensities per unit active area as functions of injected current density of the two samples. The output intensity per unit active area of sample S is higher than that of sample T. The quasi-linear curves in Fig. 9 indicate that the device heating effects in both samples are weak. Figure 10 shows the variations of normalized efficiency with injected current density of the two samples. The normalized efficiencies of both samples are evaluated via the division of the output intensity per unit active area by the product of the corresponding voltage and injected current density, and then normalized with respect to the maximum level. From the results shown in Fig. 10, one can see that the current density for the maximum efficiency of sample T is slightly larger than that of sample S. The droop slopes with current density in the two samples are about the same. Therefore, we can conclude that the efficiency droop behaviors in the two samples are quite similar.

Figure 11 shows the LED output spectra at two injected current densities (95 and 325 A/cm^2) of the two samples. Again, the spectra of sample T are red-shifted from the corresponding ones of sample S. Also, the spectral widths of sample T are larger than the corresponding values of sample S at both injected current densities. Figure 12 shows the output spectral peak wavelengths as functions of injected current density of the two samples. Here, one can see that in both samples the emission spectra blue-shift with increasing injected current density. This blue-shift trend is not due to the screening of the QCSE. The QCSE is weak in our NR-LED structures with non-polar QWs on the *m*-plane sidewalls. Instead, it is caused by the extension of the sidewall range covered by injected current from the top at low injected current to the bottom at high injected current [17]. As shown in Figs. 3 and 4, in both samples, the upper portion of an NR emits light of a longer wavelength. The emission wavelength becomes shorter in the lower portion of an NR. The variation range of emission wavelength in the two-section NR sample is significantly larger than that in the single-section NR sample. The longer-wavelength emission in the upper portion is attributed to the thicker well layer and higher indium content of the QWs in this region. The thicker QWs in the upper portion (the second uniform NR section) of an NR in sample T have been seen in the TEM images shown in Fig. 2. At low injected current, the current mainly flows into the sidewall QWs in the top portion of an NR, which has a relatively lower potential, leading to longer-wavelength emission. As injected current increases, current spreads into the lower portion of an NR for exciting the QWs to emit shorter-wavelength light. As shown in Fig. 12, in the illustrated current density ranges, the blue-shift ranges of samples S and T are 3.8 and 13.8 nm, respectively. The significantly larger blue-shift range in sample T, when compared with sample S, is consistent with the larger difference of CL spectral peak between locations 1 and 3, shown in Figs. 3 and 4, and the broader PL spectrum, shown in Fig. 6, of this sample. In Fig. 13, with the left (right) ordinate, we show the variations of spectral FWHM with injected current density of the two samples in terms of meV (nm). Again, the spectral FWHM of sample T is significantly larger than that of sample S. In particular, in terms of meV, the difference in spectral FWHM between the two samples increases with injected current density.

5. Discussions

It is noted that the EL spectra measured in the NR-LED structures are red-shifted from those in the PL and CL measurements with the QW-NR structures. This is so because the p-i-n configuration in an LED structure and the applied forward-biased voltage in EL measurement can tilt the potentials of the non-polar QWs for red-shifting the emission spectrum. Also, the overgrowth of the p-GaN layer at a high temperature (960 ^{o}C) can produce a thermal annealing effect on the QWs for further red-shifting the emission spectrum [22]. From the PL and EL measurements, we can observe the larger emission spectral width in the two-section NR sample. From the local CL measurement, we can see that this broader emission spectral width is caused by the larger emission spectral difference between the top and bottom portions of the sidewall QWs. This larger difference is attributed to the formation of the second

uniform section of a smaller cross-sectional size. Actually, the growth of the two-section NR leads to the red-shifts and broadenings of emission spectra from the QW portions at all heights (see Figs. 3 and 4). It is speculated that the indium contents of the QW portions at all heights become higher in sample T, when compared with sample S. The increased indium content in sample T may have two causes, including the stronger strain relaxation and the larger gap volume in the two-section structure. An NR section of a smaller cross-sectional size is expected to be more strain relaxed such that indium incorporation can be enhanced. Also, because of the larger gap volume between NRs, more indium atoms can fall into this volume for being adsorbed by the NR sidewalls. Since more constituent atoms are available in the upper portion of the NR array, the QW thickness and indium content can be larger in this QW portion, leading to a longer emission wavelength. The atom supplies for depositing the sidewall layers, including QWs and p-GaN, have two sources: (1) the direct downward flow of constituent atoms from the top and (2) those constituent atoms flowing downward to the bottom in the gap region between NRs and then migrating upward along the NR sidewalls. The first contribution of direct downward-flow atoms can be more important in determining the sidewall layer thickness. Therefore, the sidewall layers are usually thicker in the upper portion of an NR. In a multi-section NR, the smaller cross-sectional size of the upper portion results in a larger gap volume and hence more atom supply for sidewall deposition to produce even thicker sidewall layers. Regarding the thin sidewall-QW layer in the tapering section, it is simply due to the low growth rate on an *r*-plane surface.

In Figs. 3(b), 4(b), 5(a), and 5(b), we can see that on a sidewall, the strongest emission is distributed around middle height in both samples. The height on a sidewall for the strongest emission depends on QW growth temperature [10]. When the sidewall QWs are grown at a lower temperature, more abundant constituent atoms are available near the bottom of the gap volume such that the QW quality in this portion can be higher for stronger emission. As QW growth temperature increases, the higher kinetic energy of the constituent atoms results in a more abundant supply for forming higher-quality QWs and hence stronger emission at a higher position on a sidewall. To achieve overall longer-wavelength emission from such an NR-LED device, the QW growth temperature needs to be reduced for increasing indium incorporation. In this situation, the QW quality in the lower portion of an NR is higher and can dominate the overall emission spectrum. Nevertheless, in any situation, indium content decreases with decreasing height on a sidewall. This variation trend can counterbalance the effect of spectral red shift by decreasing the QW growth temperature. Therefore, the formation of a multi-section NR by stepwise decreasing the cross-sectional size can be a more effective method for elongating the emission wavelength. By keeping the QW growth temperature at a certain high value, the smaller cross-sectional size of an upper NR section can lead to an effective red shift of the overall sidewall emission spectrum. Besides, the overall emission spectral width can be increased for implementing a multi-color or white-light LED device without using a phosphor.

It is also noted that the difference in PL spectral FWHM at room temperature between the two samples is quite large (61.1 nm in sample T versus 36.6 nm in sample S). However, that in EL spectral FWHM is relatively smaller. For instance, at ~325 A/cm^2 in injected current density, the EL spectral FWHMs of samples S and T are ~45 and ~55 nm, respectively. The weaker spectral broadening in EL emission, when compared with PL emission, is attributed to the non-uniform current coverage on the sidewall QWs. It is speculated that in the QW portion of stronger CL emission shown in Fig. 5(a) or 5(b), the higher QW quality can lead to lower local resistance such that more injected current flows through this region for further increasing its emission intensity. In other words, besides the higher emission efficiency (higher QW quality), the higher local current density makes the predominant contribution of EL emission intensity from this portion such that the overall EL spectral width cannot be significantly increased in sample T. The uniformity of QW quality on a sidewall of an NR needs to be improved.

6. Summary

In summary, we have demonstrated the growth of a two-section, core-shell, InGaN/GaN QW NR-array LED device based on a pulsed growth technique with MOCVD. A two-section n-GaN NR was grown through a tapering process for forming two uniform NR sections of different cross-sectional sizes. The CL, PL, and EL characterization results of the two-section NR structure were compared with those of a single-section NR sample, which was prepared under the similar condition to that for the first uniform NR section of the two-section sample. It was found that all the CL, PL, and EL spectra of the two-section sample (peaked between 520 and 525 nm) were red-shifted from those of the single-section sample (peaked around 490 nm) by >30 nm in wavelength. Also, the emitted spectral widths of the two-section sample became significantly larger than their counterparts of the single-section sample. The PL

spectral FWHM increased from ~37 to ~61 nm. Such variations were attributed to the higher indium incorporation in the sidewall QWs of the two-section sample due to the stronger strain relaxation in an NR section of a smaller cross-sectional size and the more constituent atom supply from the larger gap volume between neighboring NRs.

References

1. S. D. Hersee, X. Sun, and X. Wang, "The controlled growth of GaN nanowires," Nano Lett. **6**, 1808-1811 (2006).
2. X. Wang, X. Sun, M. Fairchild, and S. D. Hersee, "Fabrication of GaN nanowire arrays by confined epitaxy," Appl. Phys. Lett. **89**, 233115 (2006).
3. Y. S. Chen, W. Y. Shiao, T. Y. Tang, W. M. Chang, C. H. Liao, C. H. Lin, K. C. Shen, C. C. Yang, M. C. Hsu, J. H. Yeh, and T. C. Hsu, "Threading dislocation evolution in patterned GaN nanocolumn growth and coalescence overgrowth," J. Appl. Phys. **106**, 023521 (2009).
4. T. Y. Tang, W. Y. Shiao, C. H. Lin, K. C. Shen, J. J. Huang, S. Y. Ting, T. C. Liu, C. C. Yang, C. L. Yao, J. H. Yeh, T. C. Hsu, W. C. Chen, and L. C. Chen, "Coalescence overgrowth of GaN nanocolumns on sapphire with patterned metal organic vapor phase epitaxy," J. Appl. Phys. **105**, 023501 (2009).
5. C. H. Liao, W. M. Chang, H. S. Chen, C. Y. Chen, Y. F. Yao, H. T. Chen, C. Y. Su, S. Y. Ting, Y. W. Kiang, and C. C. Yang, "Geometry and composition comparisons between *c*-plane disc-like and *m*-plane core-shell InGaN/GaN quantum wells in a nitride nanorod," Opt. Express **20**, 15859-15871 (2012).
6. C. H. Liao, W. M. Chang, Y. F. Yao, H. T. Chen, C. Y. Su, C. Y. Chen, C. Hsieh, H. S. Chen, C. G. Tu, Y. W. Kiang, and C. C. Yang, "Cross-sectional sizes and emission wavelengths of regularly patterned GaN and core-shell InGaN/GaN quantum-well nanorod arrays," J. Appl. Phys. **113**, 054315 (2013).
7. W. Bergbauer, M. Strassburg, Ch. Kölper, N. Linder, C. Roder, J. Lähnemann, A. Trampert, S. Fündling, S. F. Li, H. H. Wehmann, and A. Waag, "N-face GaN nanorods: continuous-flux MOVPE growth and morphological properties," J. Cryst. Growth **315**, 164-167 (2011).
8. W. Bergbauer, M. Strassburg, Ch. Kölper, N. Linder, C. Roder, J. Lähnemann, A. Trampert, S. Fündling, S. F. Li, H. H. Wehmann, and A. Waag, "Continuous-flux MOVPE growth of position-controlled N-face GaN nanorods and embedded InGaN quantum wells," Nanotechnology **21**, 305201 (2010).
9. X. Wang, S. F. Li, M. S. Mohajerani, J. Ledig, H. H. Wehmann, M. Mandl, M. Strassburg, U. Steegmüller, U. Jahn, J. Lähnemann, H. Riechert, I. Griffiths, D. Cherns, and A. Waag, "Continuous-flow MOVPE of Ga-Polar GaN column arrays and core–shell LED structures," Cryst Growth Des. **13**, 3475-3480 (2013).
10. C. H. Liao, C. G. Tu, W. M. Chang, C. Y. Su, P. Y. Shih, H. T. Chen, Y. F. Yao, C. Hsieh, H. S. Chen, C. H. Lin, C. K. Yu, Y. W. Kiang, and C. C. Yang, "Dependencies of the emission behavior and quantum well structure of a regularly-patterned, InGaN/GaN quantum-well nanorod array on growth condition," Opt. Express **22**, 17303-17319 (2014).
11. Y. T. Lin, T. W. Yeh, and P. D. Dapkus, "Mechanism of selective area growth of GaN nanorods by pulsed mode metalorganic chemical vapor deposition," Nanotechnology **23**, 465601 (2012).
12. T. W. Yeh, Y. T. Lin, L. S. Stewart, P. D. Dapkus, R. Sarkissian, J. D. O'Brien, B. Ahn, and S. R. Nutt, "InGaN/GaN multiple quantum wells grown on nonpolar facets of vertical GaN nanorod arrays," Nano Lett. **12**, 3257-3262 (2012).
13. Y. T. Lin, T. W. Yeh, Y. Nakajima, and P. D. Dapkus, "Catalyst-free GaN nanorods synthesized by selective area growth," Adv. Funct. Mater. **24**, 3162-3171 (2014).
14. B. O. Jung, S. Y. Bae, Y. Kato, M. Imura, D. S. Lee, Y. Honda, and H. Amano, "Morphology development of GaN nanowires using a pulsed-mode MOCVD growth technique," CrystEngComm **16**, 2273-2282 (2014).
15. B. O. Jung, S. Y. Bae, S. Y. Kim, S. Lee, J. Y. Lee, D. S. Lee, Y. Kato, Y. Honda, and H. Amano, "Highly ordered catalyst-free InGaN/GaN core–shell architecture arrays with expanded active area region," Nano Energy **11**, 294-303 (2015).
16. H. S. Chen, Y. F. Yao, C. H. Liao, C. G. Tu, C. Y. Su, W. M. Chang, Y. W. Kiang, and C. C. Yang, "Light-emitting device with regularly patterned growth of an InGaN/GaN quantum-well nanorod light-emitting diode array," Opt. Lett. **38**, 3370-3373 (2013).
17. C. G. Tu, C. H. Liao, Y. F. Yao, H. S. Chen, C. H.Lin, C. Y. Su, P. Y. Shih, W. H. Chen, E. Zhu, Y. W. Kiang, and C. C. Yang, "Regularly patterned non-polar InGaN/GaN quantum-well nanorod light-

emitting diode array," Opt. Express **22**, A1799-A1809 (2014).
18. C. Tessarek, M. Heilmann, E. Butzen, A. Haab, H. Hardtdegen, C. Dieker, E. Spiecker, S. Christiansen, "The role of Si during the growth of GaN micro- and nanorods," Cryst. Growth Des. **14**, 1486-1492 (2014).
19. Y. F. Yao, H. T. Chen, C. Y. Su, C. Hsieh, C. H. Lin, Y. W. Kiang, and C. C. Yang, "Phosphor-free, white-light LED under alternating-current operation," Opt. Lett. **39**, 6371-6374 (2014).
20. M. Kubota, K. Okamoto, T. Tanaka, and H. Ohta, "Temperature dependence of polarized photoluminescence from nonpolar *m*-plane InGaN multiple quantum wells for blue laser diodes," Appl. Phys. Lett. **92**, 011920 (2008).
21. Y. S. Lin, K. J. Ma**,** C. Hsu, S. W. Feng, Y. C. Cheng, C. C. Liao, C. C. Yang, C. C. Chuo, C. M. Lee, and J. I. Chyi, "Dependence of composition fluctuation on indium content in InGaN/GaN multiple quantum wells," Appl. Phys. Lett. **77**, 2988 (2000).
22. C. Y. Chen, C. Hsieh, C. H. Liao, W. L. Chung, H. T. Chen, W. Cao, W. M. Chang, H. S. Chen, Y. F. Yao, S. Y. Ting, Y. W. Kiang, C. C. Yang, and X. Hu, "Effects of overgrown p-layer on the emission characteristics of the InGaN/GaN quantum wells in a high-indium light-emitting diode," Opt. Express **20**, 11321-11335 (2012).

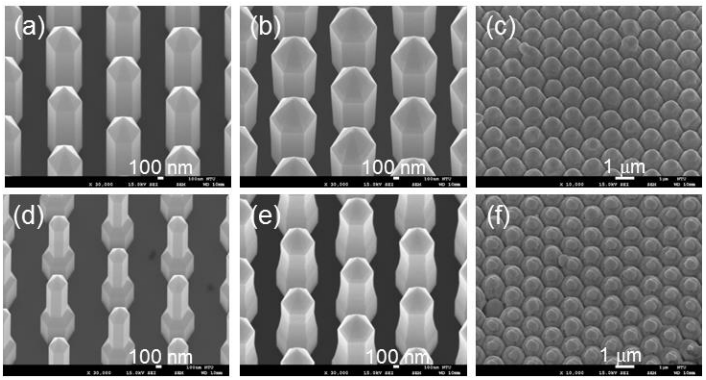

Fig. 1. (a): Tilted SEM image of the n-GaN NR-core array of sample S. (b): Tilted SEM image of the NR-LED array of sample S. (c): Tilted SEM image of the NR-LED array of sample S after GaZnO deposition. (d)-(f): Similar to parts (a)-(c), respectively, except for sample T.

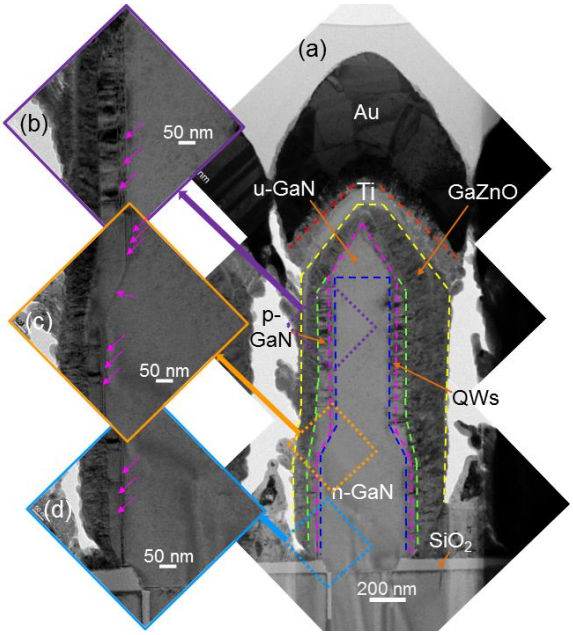

Fig. 2. (a): TEM image of an NR of LED sample T. Dashed lines are plotted to roughly indicate the boundaries of different materials. (b)-(d): Magnified TEM images in the regions indicated by the three dotted-line squares. Three QWs on the sidewalls of the two uniform NR sections are indicated by the (pink) arrows.

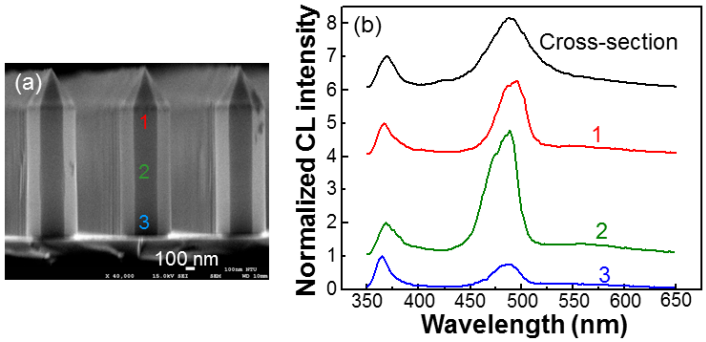

Fig. 3. (a): Cross-sectional SEM image of a QW-NR array of sample S with three locations for local CL spectral measurements being marked as 1-3. (b): CL spectra at locations 1-3, as marked in part (a), and the overall cross-sectional CL spectrum (labeled by "Cross-section").

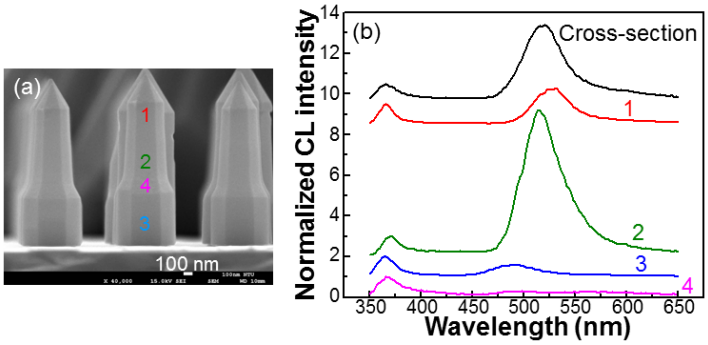

Fig. 4. (a): Cross-sectional SEM image of a QW-NR array of sample T with four locations for local CL spectral measurements being marked as 1-4. (b): CL spectra at locations 1-4, as marked in part (a), and the overall cross-sectional CL spectrum (labeled by "Cross-section").

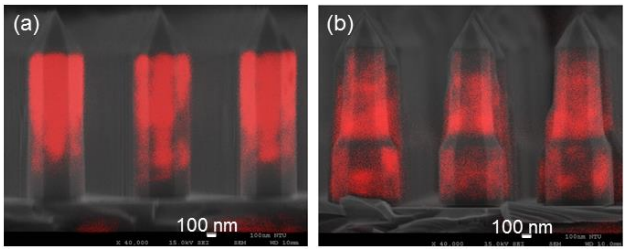

Fig. 5 (a) and (b): Cross-sectional CL mapping images of samples S and T, respectively, overlaid on the individual cross-sectional SEM images.

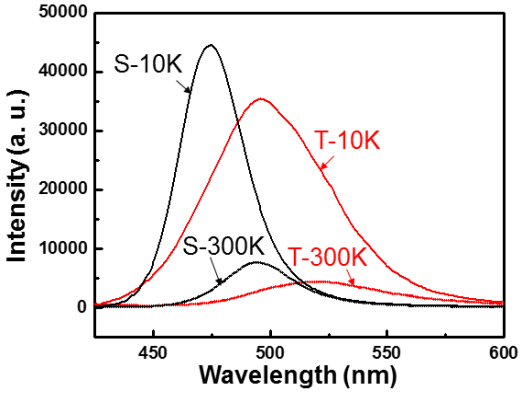

Fig. 6. PL spectra of samples S and T at 10 and 300 K.

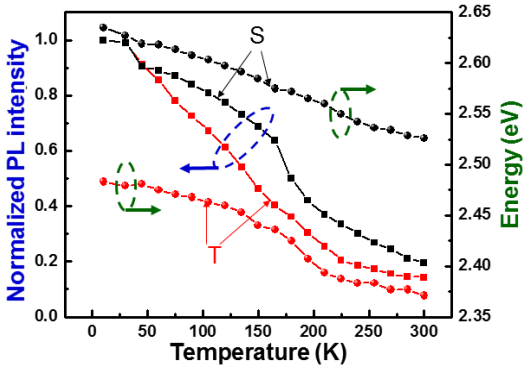

Fig. 7. Variations of normalized PL intensity (the left ordinate) and PL spectral peak energy (the right ordinate) with temperature of the two QW-NR samples.

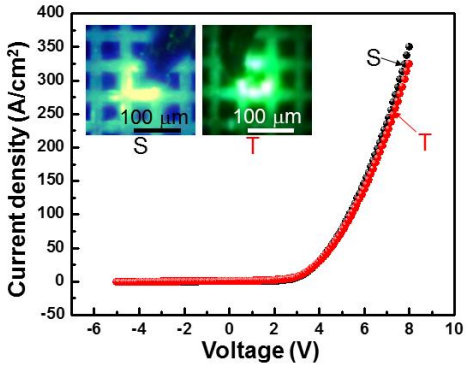

Fig. 8. Relations between injected current density and applied voltage (J-V curves) of the two NR-LED samples. The insets show the photographs of lit devices of samples S and T when the applied voltage is 8 V.

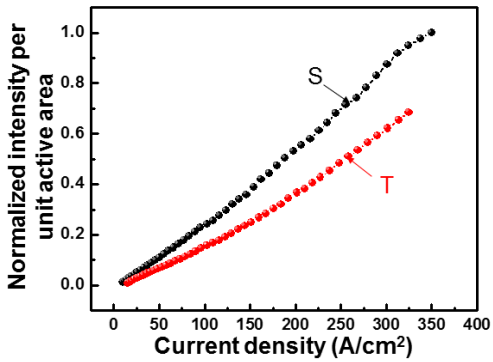

Fig. 9. Output intensities per unit active area as functions of injected current density of the two NR-LED samples.

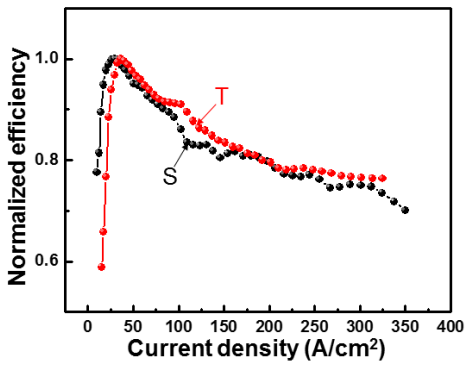

Fig. 10. Variations of normalized efficiency with injected current density of the two NR-LED samples.

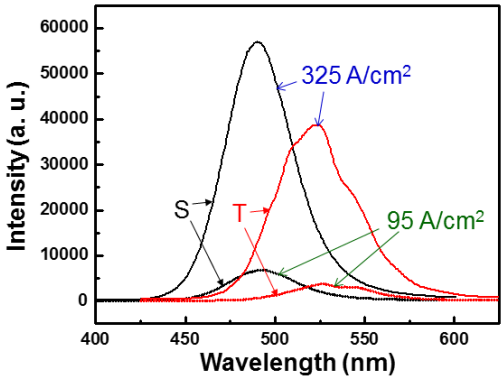

Fig. 11. Output spectra at two injected current densities (95 and 325 A/cm^2) of the two NR-LED samples.

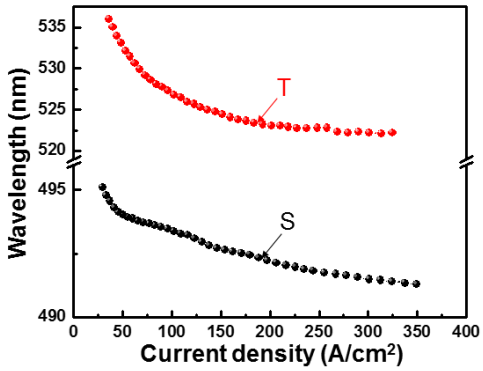

Fig. 12. Output spectral peak wavelengths as functions of injected current density of the two NR-LED samples.

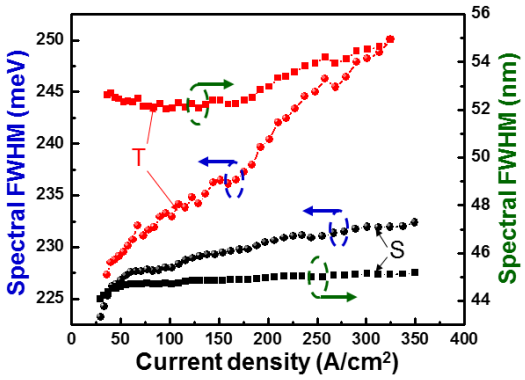

Fig. 13. Variations of EL spectral FWHM with injected current density of the two NR-LED samples in terms of meV (nm) with the left (right) ordinate.

Chapter 2: Regularly-patterned multi-section GaN nanorod arrays grown with a pulsed growth technique

1. Introduction

Due to the advantages of higher crystal quality, reduced quantum-confined Stark effect (QCSE), and larger emission area (sidewall emission), randomly-distributed and regularly-patterned GaN nanorod (NR) light-emitting diode (LED) arrays with either along-axis disk-like or sidewall core-shell InGaN/GaN quantum-well (QW) structures have been widely grown with molecular beam epitaxy [1-11] and metalorganic chemical vapor deposition (MOCVD) [12-30]. Although a randomly-distributed NR array can provide us with a platform for understanding the characteristics of such an NR LED [1-6, 12-19], its random distributions of NR location and geometry make the control of emission specifications difficult in lighting application. For lighting application, a regularly-patterned NR LED array grown with MOCVD is more attractive [20-34]. With MOCVD growth, regularly-patterned NR LED arrays can be formed through the continuous [26-28] and pulsed growth modes [20-25, 29-34]. In the pulsed growth mode, either the supply of group III or V source, or both are modulated. Under the condition of switching on and off alternatively the supplies of group III (TMGa) and group V (NH_3) sources, the Ga supply in the first half-cycle leads to the formation of Ga droplets at the selected NR growth locations for serving as the catalyst in precipitating GaN when NH_3 is supplied in the second half-cycle. With such a pulsed growth mode, an n-GaN NR of a uniform cross-sectional size can be formed on a patterned GaN template. Then, InGaN/GaN QWs and a conformal p-GaN layer can be deposited on the *m*-plane sidewalls, *r*-plane slant facets ({1-101} planes), and *c*-plane top face with the ordinary two-dimensional (2-D) growth mode for forming an LED structure. The deposition of non-polar *m*-plane QWs or semi-polar *r*-plane QWs can lead to the advantages of reduced QCSE and hence higher emission efficiency.

Based on the pulsed growth mode with MOCVD, regularly-patterned NR LED arrays of controllable NR cross-sectional sizes, NR heights, and pitches have been fabricated by this research team [24, 25, 29]. After the growth an n-GaN NR array, the NR top is flat (*c*-plane) except the small {1-102}-plane slant facets at the edge. On such an n-GaN NR, *c*-plane top-face QWs and *m*-plane sidewall QWs can be formed. In this situation, after an NR LED array is fabricated, non-polar emission is mixed with polar emission in the LED output [35]. If a pyramidal GaN structure can be formed at the NR top before QW deposition, the growth of *c*-plane QW can be avoided such that only non-polar sidewall QWs are formed since the deposition rate on the slant facets of the pyramidal structure ({1-101}-plane) is low. In this situation, the completely non-polar emission can be obtained from such an NR LED array [36].

Although phosphors have been widely used for converting photon wavelengths to mix into multi-color or white light, phosphor-free broad-spectral light source is still an attractive issue for saving the energy loss during light color conversion. In a core-shell QW NR structure, because of the non-uniform constituent atom supply for QW growth at different heights on a sidewall, usually a broader emission spectrum can be obtained, when compared to a planar LED structure. Quite broad emission spectra from core-shell QW NR or NR LED structures have been reported. Although broad distributions of emission wavelength (>100 nm) based on cathodoluminescence (CL) mapping on NR sidewalls have been reported, the spectral full-widths at half-maximum (FHHMs) of their overall NR emissions are generally smaller than ~60 nm [16, 28, 31, 34, 37-40]. In particular, some of the previously reported spectra consist of the emissions from the InGaN nanostructures grown on more than one crystal facet [37]. Efforts are needed for further increasing the emission spectral FWHM for developing phosphor-free multi-color or white light techniques [41]. In particular, broad-spectrum emission completely from *m*-plane, non-polar QWs is preferred for high-efficiency, QCSE-free white-light application.

The formation of an NR segment in a pulsed-growth cycle by switching TMGa and NH_3 supplies on and off alternatively is controlled by the size of the Ga droplet. The size of the Ga droplet is determined by the TMGa supply duration and flow rate. Therefore, during pulsed growth, if the TMGa supply duration or flow rate is varied, the NR cross-sectional size can be changed. Such an NR tapering technique should be useful for increasing device versatility when NRs are used for the fabrications of sensing, electronics, and other optoelectronics devices [42-44]. Also, because the compressive strain condition of an InGaN well layer on an NR is related to its cross-sectional size, the depositions of QWs on the sidewalls of the NR sections of different cross-sectional sizes can lead to different QW structures and/or indium compositions for emitting lights of different wavelengths. In this chapter, we report the study results of tapering the cross section of an n-GaN NR through the variation of TMGa supply duration in pulsed growth. After a tapering process, another uniform NR section of a smaller cross-

sectional size is grown for forming a multi-section NR. The NR morphology evolution during a tapering process is demonstrated by analyzing the contrast line structures observed in a scanning electron microscopy (SEM) image. Such a contrast line-marker, which is formed with a thin Ga-rich layer, corresponds to the boundary between two successive cycles in pulsed growth. By comparing the CL and photoluminescence (PL) spectra of single-, 2-, and 3-section QW NR arrays, we show that a multi-section NR can lead to a significantly broader sidewall-QW emission spectrum. In section 2 of this chapter, the growth conditions and results of regularly-patterned single-section n-GaN NR arrays are presented. In section 3, the growth conditions and results of tapering processes and multi-section n-GaN NR arrays are reported. Then, in section 4, the SEM image showing the tapering scenarios is analyzed. The tapering mechanism is discussed in section 5. Emission behaviors from the sidewall QWs on single- and multi-section NRs are compared in section 6. Finally, conclusions are drawn in section 7.

2. Growth of single-section n-GaN nanorod arrays

The growth of regularly-patterned n-GaN NR arrays starts with the fabrication of a patterned-hole template, which consists of a 2-μm thick un-doped GaN layer and then a 2-μm thick n-type GaN layer on a *c*-plane sapphire substrate. The template for NR-array growth is formed by first depositing a SiO_2 layer of ~40 nm in thickness and then patterning a 2-D hole array through nano-imprint lithography and reactive ion etching. Figure 1(a) shows the plan-view SEM image of a hole pattern. Here, one can see that the n-GaN layer of the template is exposed at the hole bottom. Before forming an NR structure, the patterned holes need to be filled up with n-GaN for serving as the seed of the following pulsed growth. The hole-filling process is undertaken with the ordinary 2-D growth mode for 24 sec at 1050 degrees in growth temperature. Due to the high growth selectivity, GaN can be grown only in the patterned holes. The duration for hole-filling is chosen to be the shortest for forming a hexagonal geometry at a patterned hole, as shown in the plan-view SEM image of Fig. 1(b). In this process, the TMGa, NH_3, and silane flow rates for n-GaN growth are 20, 1500, and 12 sccm, respectively. To form an n-GaN NR array, the supplies of TMGa and NH_3 are switched on and off alternatively, as schematically demonstrated in Fig. 1(c). In a growth cycle, a melting Ga droplet is formed at the top of a designated location (an NR) during the first half-cycle for TMGa supply, as schematically demonstrated in Fig. 1(d). The tilted SEM image in Fig. 1(e) shows the Ga droplets at the tops of individual n-GaN structures when the pulsed growth is aborted during the first half-cycle for TMGa supply [25]. The Ga droplets are used out during the second half-cycle for NH_3 supply to precipitate n-GaN for forming an incremental layer of n-GaN. As shown in Fig. 1(c), between the supply of TMGa for a duration of t_{III} and the supply of NH_3 for a duration of t_V, a pause is applied for a duration of t_p. During the pulsed growth, the silane supply for forming n-type GaN is continuous at 12 sccm. The pulsed growth can lead to the formation of an n-GaN NR of a uniform hexagonal cross section, as shown in the plan-view and tilted SEM images in Figs. 1(f) and 1(g), respectively. For growing this NR sample, we use t_{III} = 20 sec, t_V = 30 sec, t_p = 1.5 sec, and the cycle number of pulsed growth at 37. Also, the growth temperature is kept at ~1040 degrees throughout the pulsed growth process. Meanwhile, the flow rates of TMGa and NH_3 are 15 and 500 sccm, respectively. The cross-sectional size of the NRs is controlled by the patterned hole diameter and is weakly related to the patterned pitch and NR height [25]. As shown in Fig. 1(g) and also schematically depicted in Fig. 1(d), the top face of an n-GaN NR is flat except the slant facets at the edge. These slant facets correspond to the {1-102}-planes. After the formation of n-GaN NRs, InGaN/GaN QWs can be deposited on the *c*-plane top face and *m*-plane sidewalls, as schematically shown in Fig. 2(a) with three QW periods. In this QW growth process, a pyramidal or truncated-pyramidal structure at the NR top is formed. The slant facets of this NR top structure correspond to {1-101}-planes. Figures 2(b) and 2(c) show the plan-view and tilted SEM images, respectively, of such a QW NR array.

3. Tapering growth and multi-section n-GaN nanorod arrays

A constant supply duration of TMGa as depicted in Fig. 1(c) leads to the NR growth of a uniform cross-sectional size. As schematically demonstrated in Fig. 3(a), when the supply duration of TMGa, t_{III}, decreases with cycle number while the supply duration of NH_3, t_V, is kept constant, the cross-sectional size of an NR can be tapered. Figure 3(b) shows the tilted SEM image of an n-GaN NR array with the growth procedure of varying the TMGa supply duration, t_{III}, as: 20 sec for 37 cycles, 15 sec for 3 cycles, 10 sec for 3 cycles, then 5 sec for 6 cycles. Other conditions of t_V = 30 sec and t_p = 1.5 sec are fixed. Here, one can see that a truncated-pyramidal structure is formed at the NR top with the slant facets corresponding to {1-101}-planes. At the top, a small flat area is left. Following the same growth conditions except that the cycle number of 5-sec TMGa supply is increased to 20, a pointed-pyramidal structure is formed at the NR top, as shown in the SEM image of Fig. 3(c). A stepwise decreasing TMGa

supply duration combining with a constant NH_3 supply duration in the pulsed growth process can lead to an NR of a tapered cross-sectional size. In particular, the tapering process can be controlled for forming a flat top-face of a designated size. This flat top-face can be used as the base for growing another uniform NR section of a smaller cross-sectional size. In the following discussions of this chapter, all samples are grown under the fixed conditions of t_V = 30 sec, t_p = 1.5 sec, V/III ratio at 33.3, silane flow rates at 12 sccm, and the n-GaN growth temperature at ~1040 degrees. The TMGa flow rate is usually fixed at 15 sccm unless particularly specified. In every tapering process discussed below, it always includes 3 cycles of 15-sec, 3 cycles of 10-sec, and then a designated cycle number of 5-sec TMGa supplies. In forming an NR section of a uniform cross section, a designated cycle number of 20-sec TMGa supply is used.

Figure 4(a) shows the tilted SEM image of an array of n-GaN NR with two uniform sections of different cross-sectional sizes. Each uniform section is formed with 20 cycles of 20-sec TMGa supply. For forming the tapering section between the two uniform sections, 3 cycles of 5-sec TMGa supply are used. Figure 4(b) shows a schematic drawing of such a 2-section n-GaN NR. Here, one can see that a tapering section exists between the two sections of uniform cross section. Because no tapering process is applied to the top of the second uniform section, the NR has a flat top with {1-102} slant facets at the edge. The similar growth procedure can be repeated for forming 3- and 4-section NRs, as shown in the SEM images of Figs. 4(c) and 4(d), respectively. The 3-section n-GaN NRs are formed by increasing the cycle number of 5-sec TMGa supply to 6 in either one of the two tapering processes. The 4-section n-GaN NRs are fabricated with the cycle number of 5-sec TMGa supply kept at 3 in any one of the three tapering processes.

In the tilted SEM images of Figs. 5(a)-5(c), we compare the morphologies of three 3-section n-GaN NR arrays, in which three processes of 20-cycle of 20-sec TMGa supply are followed by three different tapering processes with 3, 6, and 9 cycles of 5-sec TMGa supply for the results in Figs. 5(a)-5(c), respectively. With 6 cycles of 5-sec supply [see Fig. 5(b)], the tapering range is larger such that the differences in cross-sectional size between the three uniform sections are larger, when compared with those of the NR array with 3 cycles of 5-sec supply [see Fig. 5(a)]. With a smaller cross-sectional size, the NR section becomes higher. However, with 9 cycles of 5-sec TMGa supply, only two uniform sections can be clearly seen in Fig. 5(c). The tapering process between the second and third uniform sections is unclear in this sample. The cause for such a growth result will be discussed later.

4. Tapering process in a multi-section n-GaN nanorod

Figure 6(a) shows the cross-sectional SEM image of three 3-section NRs. Each NR includes three uniform sections and three tapering sections. Each uniform section consists of 10 cycles of 20-sec TMGa supply for n-GaN growth. Each tapering section consists of 3 cycles of 15-sec, 3 cycles of 10-sec, and then 6 cycles of 5-sec TMGa supplies. The flow rate of TMGa for the first uniform and first tapering sections is 15 sccm. That for the second (third) uniform and second (third) tapering sections is reduced to 10.5 (6) sccm. Three periods of QW are grown on the sidewalls. However, they are not the issues for discussion here. In preparing this sample for cross-sectional SEM observation, the central NR in Fig. 6(a) is bisected such that the interior structure of this 3-section NR can be observed. As shown in Fig. 6(a), dark line patterns can be seen in the central NR. Each line, which is to be called a line-marker, includes the central horizontal segment and the two quasi-symmetric tilted segments on both sides. It is supposed to be corresponding to the boundary between two successive cycles in pulsed growth, as to be discussed in detail later in this section. To more clearly show the patterns of those line-markers of pulsed growth, we plot dashed lines following the traces of those line-markers in the first and second uniform sections and the first tapering section, as shown in Fig. 6(b). Here, the dashed lines of different colors represent presumably different growth cycles of different TMGa supply durations. The line plotting may not be very accurate; however, it can provide us with reasonably accurate information about the morphology evolution of the NR growth. Here, the horizontal dashed line at the bottom corresponds to the starting level of pulsed growth after hole filling. In the first cycle of pulsed growth, a truncated pyramidal structure is formed on the top of the filled hole. The lateral size of the truncated pyramidal structure is increased to the NR cross-sectional size in the second cycle. Then, the size of the flat top-face keeps increasing until the end of this stage of a constant TMGa supply duration (10 cycles of 20-sec supply). In this uniform section, the tilted segments of the line-markers form an angle of ~43 degrees with respect to the horizontal plane (*c*-plane). In the first tapering process, as the TMGa supply duration decreases stepwise, the size of the flat top-face increases first and then keeps decreasing. Meanwhile, the angle with respect to the *c*-plane of the tilted segments keeps increasing to reach ~62 degrees. This tilted angle returns gradually to ~43 degrees after the growth stage for the

second uniform section starts. It is noted that in the growth stage of 6 cycles of 5-sec TMGa supply, the line-markers for the flat top-face are unclear. The dashed lines in Fig. 6(b) are plotted by equally dividing the total grown thickness into 6 layers. Because the thickness of such a layer is quite small, this part of plotting does not affect the understanding of the NR morphology evolution during the tapering process. Because the line-markers become too dense for us to differentiate one from the other after the second uniform section, the dashed-line plotting stops at the top of this section. It is noted that the vertical bright stripes on the NR sidewalls correspond to the three *m*-plane QWs. NR bisection leads to the unsmooth NR sidewalls in Fig. 6(a) or 6(b). The vertical boundaries of the n-GaN NR core are roughly indicated by the vertical (blue) dotted lines.

In Figs. 7(a)-7(d), we show the variations of the slant-facet (tilted line-marker segment) angle, flat-top width, flat-top thickness, and projected area, respectively, during NR growth based on the line-marker plotting in Fig. 6(b). Here, the projected area can provide us with the information of n-GaN growth volume in a growth cycle. In Fig. 7(a), one can indeed observe that the tilted angle of the slant facet keeps at ~43 degrees in the first 10 cycles of the constant TMGa supply duration. This angle increases during the 3 cycles of 15-sec and 3 cycles of 10-sec supplies and saturates at ~62 degrees during the 6 cycles of 5-sec supply. When the TMGa supply duration returns to 20 sec for growing the second uniform section, the tilted angle decreases back to ~43 degrees in 4-5 cycles. In Fig. 7(b), we can see that the flat-top width increases first slowly and then rapidly in the first 10 cycles for growing the first uniform section. The flat-top width is essentially kept constant at ~370 nm during the 3 cycles of 15-sec supply. Then, during the 3 cycles of 10-sec and 6 cycles of 5-sec supplies, the flat-top width keeps decreasing, but with different decreasing slopes. When the TMGa supply duration returns to 20 sec, the flat-top width increases to a level of ~280 nm and saturates there. In Fig. 7(c), we can see that the flat-top thickness first increases and then decreases during the growth of the first uniform section. During the 15-sec and 10-sec supplies, the flat-top thickness essentially increases. However, it reaches a minimum during the process of 6 cycles of 5-sec supply. Although the values of the flat-top thickness during this process cannot be so reliable, for sure it reaches a minimum during this process. In Fig. 7(d), the variation of the projected area is similar to that of the flat-top thickness. The grown n-GaN volume increases first and then decreases in the first 10 cycles for growing the first uniform section. It slightly increases during the 15-sec and 10-sec supply stages, and decreases to a minimum level during the 5-sec supply stage. After the TMGa supply duration returns to 20 sec, the growth volume is increased and then decreased to saturate at a certain level.

The line-markers for illustrating the boundaries between successive growth cycles can also be seen in a high angle annular dark field (HAADF) image of an NR in transmission electron microscopy (TEM) observation. Figure 8(a) shows the TEM HAADF image around the first tapering section of a 3-section QW NR. Here, besides the bright lines on the sidewalls corresponding to the three QWs, bright line-markers including the *c*-plane segments at the center and the slant-facet segments on both sides can be seen. In a tapering process of this sample, the growth procedure includes 3 cycles of 15-sec, 3 cycles of 10-sec, and then 3 cycles of 5-sec TMGa supplies. Each uniform section consists of 20 cycles of 20-sec TMGa supply. The TMGa flow rate is kept constant during its supply throughout the whole growth process of this NR. Figure 8(b) shows the same TEM HAADF image, but with dashed lines plotted for tracing the line-markers. Here, one can see that the evolution of NR morphology during the tapering process is similar to that shown in Fig. 6(b). It is noted that a region of a heavier atom distribution or a higher-concentration distribution of heavy atom shows a brighter contrast in a HAADF image. Also, a metal-rich region may result in locally higher conductivity and hence a darker contrast in an SEM image. Therefore, the dark line-markers in Fig. 6(a) and the bright line-markers in Fig. 8(a) correspond to thin layers of Ga-rich growth. It is speculated that at the beginning of GaN precipitation when the super-saturation condition of N atoms in a Ga droplet is reached, a thin layer of Ga-rich GaN is formed in each growth cycle. Hence, a thin Ga-rich layer or a line-marker indicates the boundary between two successive growth cycles.

5. Mechanism of a tapering process

The evolution of NR morphology during a tapering process is controlled by the size of the catalytic Ga droplet and its coverage range at the NR top. In Figs. 9(a)-9(j), we schematically demonstrate the morphology evolution of an NR with the speculated Ga droplet geometry for simulating the tapering process shown in Fig. 6(b). As shown in Fig. 9(a), during the growth stage of the constant TMGa supply duration of 20 sec, the melting Ga droplet is large and covers at least the major portion of a slant facet. In this situation, during the half-cycle for NH_3 supply, GaN is precipitated on the flat-top and slant facets for the growths along both *c*- and *m*-axis such that the {1-102}-plane slant facets of 43.22 degrees in

tilted angle with respect to the *c*-plane are maintained during the growth process of the uniform section. When the supply duration of TMGa is reduced to 15 sec, the size of Ga droplet becomes smaller such that it covers only a small portion of a slant facet, as shown in Figs. 9(b) and 9(c). In this situation, on a slant facet, GaN precipitation can occur only around its top edge such that the pulsed growth leads to relatively more lateral growth there and hence the increase of the tilted angle of the slant facet. Meanwhile, the flat-top size is slightly increased. At this stage, the flat-top thickness in a growth cycle is small. When the TMGa supply duration is further reduced to 10 sec, the size of the Ga droplet is further decreased such that it covers only the central portion of the flat-top, as shown in Figs. 9(d) and 9(e). In this situation, GaN precipitation can occur only in the central portion of the flat top such that the flat-top width is reduced and its thickness is increased. Under this condition, the tilted angle of a slant facet is effectively increased. Then, when the TMGa supply duration is reduced to 5 sec, the size of the Ga droplet is further decreased for covering only the flat top of a reduced width, as shown in Figs. 9(f) and 9(g). At this stage, the tilted angle saturates at 61.98 degrees, corresponding to the {1-101}-plane. Also, the flat-top width decreases for maintaining the {1-101}-plane in a slant facet. Meanwhile, the increment of NR height is small. The change of a slant facet from the {1-102}-plane into the {1-101}-plane is caused by the variation of the relative growth rate between the vertical and lateral directions. When the TMGa supply duration is returned to 20 sec for growing the second uniform section, the size of the Ga droplet becomes large. However, it should be smaller than that formed during the growth of the first uniform section because the TMGa flow rate is reduced to 70 %. Nevertheless, its dimension is still larger than the flat-top width such that it covers a large portion of a {1-101}-plane slant facet, as shown in Fig. 9(h). In this situation, the GaN precipitation in the Ga-droplet coverage range on the slant facet leads to the growth along the *m*-axis and the formations of a segment of *m*-plane vertical sidewall plus a slant facet with a reduced tilted angle, as shown in Fig. 9(i). At this stage, both the flat-top width and thickness first increase and then saturate to form the second uniform section, as shown in Fig. 9(j). In Figs. 9(a)-9(i), the key portions of the slant facets are circled to attract attention.

From the discussions above, one can see that the used 15-sec and 10-sec cycles are important for shaping the slant facets and shrinking the flat-top width such that the small Ga droplet formed during the 5-sec supply can continue to reduce the flat-top width or the NR cross-sectional size. In Fig. 5(c), we see the result of a 2-section NR array even though the growth procedure is designed for a 3-section NR array. In this NR-array sample, after the first tapering process with 9 cycles of 5-sec TMGa supply, the cross-sectional size of the second uniform section becomes quite small, as shown in Fig. 5(c). In this situation, during the second tapering process again with 9 cycles of 5-sec TMGa supply, the flat top-face becomes too small to support the Ga droplet such that it covers all over the slant facets. Hence, the GaN precipitation on the whole slant facets leads to the *m*-axis growth for forming the *m*-plane sidewalls with the same hexagonal cross-sectional size as that of the second uniform section plus the {1-102}-plane slant facets. In other words, the second tapering structure is not successfully formed for further reducing the NR cross-sectional size.

As shown in Figs. 2(a)-2(c), when the MOCVD growth is switched into the 2-D growth mode after the formation of an NR for depositing a QW structure, a pointed- or truncated-pyramidal structure is grown at the NR top with {1-101}-plane slant facets besides the growth on the sidewalls. Therefore, we can conclude that at the top of a *c*-oriented GaN NR, a process of continuous growth along the *c*-axis will lead to the formation of a pyramidal structure with {1-101}-plane slant facets unless GaN precipitation can occur on the slant facets through catalyst coverage. GaN precipitation on a slant facet to maintain its {1-102}-plane is the key point for growing an NR of a uniform cross section. Without the catalytic Ga droplet covering the slant facets, a pyramid, instead of an NR, is formed at the beginning of the whole growth procedure. In this regard, a process of 2-D growth can also lead to a tapering structure. However, in this situation, *m*-plane growth on the sidewalls also occurs leading to an NR of a larger cross-sectional size. It is noted that because a thin SiN layer can be formed on a sidewall in n-GaN NR growth, the quality of sidewall GaN growth is usually poor [17]. Such a SiN layer can be removed through buffered oxide etching after the growth of an n-GaN NR is completed and the NR is ready for QW deposition.

Recently, a growth model has been proposed for explaining the GaN NR growth results based on a pulsed growth process including a growth pause stage after either Ga or N supply duration [30, 31, 33, 34]. In this model, the pause stage right after Ga supply is applied for the Ga adatoms on the *m*-plane sidewalls of an NR to be desorbed such that Ga adatoms are mainly distributed on the *c*-plane top face and hence NR growth can continue. The pause stage right after N supply is used to evacuate NH_3 in the growth chamber before the next growth cycle for avoiding the continuous growth condition. The concept of Ga adatom distribution mainly on the *c*-plane top face is consistent with our model of Ga

droplet at the NR top. Based on our explanation for the tapering process above, the larger tilted angles of the slant facets (close to the {1-101}-plane) in the cited results [30, 31, 33, 34], when compared with ours (the {1-102}-plane), during the growth of an NR of a uniform cross section can be attributed to their smaller Ga droplets formed on the *c*-plane top face because of their shorter Ga supply durations. Although the concept of their model is basically consistent with ours, two growth results of ours cannot be explained with their model. First, in our growth, once a pointed-pyramidal top structure with {1-101}-plane slant facets is formed on an NR, a further increase of NR height becomes difficult. However, because their model does not exclude the Ga adatoms on the {1-101}-plane, the continuous growth of an NR seems to be possible. Second, in the tapering process discussed above, on a truncated-pyramidal top, another uniform section of a smaller cross section can be formed when we switch the TMGa supply duration back to a larger value (20 sec in the condition above). However, their model may imply the continuous growth of the NR with the same cross section size.

6. Broadening emission spectrum in a multi-section nanorod array

One of the important applications of a multi-section GaN NR is to increase the emission spectral width from its sidewall QWs. Because of the non-uniform supply of QW constituent atoms among different heights on the sidewalls of an NR of a uniform cross section, the QW structures and compositions at different heights are different, leading to a certain emission spectral width from the sidewall QWs [24]. If such a spectral width can be further increased, a phosphor-free multi-color or white-light LED can be implemented. In a multi-section NR, because of the different strain relaxation conditions of deposited InGaN/GaN QWs in different sections of different cross-sectional sizes, we expect larger differences in sidewall-QW structure and composition between two different sections and hence a larger sidewall-QW emission spectral width. Figures 10(a)-10(d) show the tilted SEM images of a single-section, two 2-section, and one 3-section n-GaN NR arrays, respectively. For growing the single-section NR array (sample S) shown in Fig. 10(a), 24 cycles of 20-sec Ga supply are used for fabricating the uniform section and then 3, 3, and 20 cycles of 15-, 10-, and 5-sec Ga supplies, respectively, are used for forming the pyramidal top. For growing the 2-section n-GaN NR array shown in Fig. 10(b) [Fig. 10(c)], which is designated as sample T1 (T2), after 10 cycles of 20-sec Ga supply for forming the first uniform section, 3, 3, 6 cycles (3, 3, and 12 cycles) of 15-, 10-, and 5-sec Ga supplies, respectively, are used for forming the tapering section, followed by 12 cycles of 20-sec Ga supply for forming the second uniform section and the same process for fabricating the pyramidal top. The contrast of cross-sectional size between the two uniform sections in sample T2 is larger than that in sample T1. For fabricating the 3-section n-GaN NR array shown in Fig. 10(d), which is designated as sample T3, the same tapering process as that in sample T1 is repeated between three uniform sections of 10 growth cycles of 20-sec TMGa supply in each section. The similar pyramidal top is also formed in sample T3. The TMGa flow rate for growing sample S and the first uniform sections of samples T1-T3 is 15 sccm. That for growing the second sections of samples T1-T3 is 10.5 sccm. Meanwhile, that for growing the third section of sample T3 is 7.5 sccm. Figures 10(e)-10(h) show the tilted SEM images after three periods of InGaN/GaN QWs (with the growth temperature for InGaN at 680 ^{o}C) are grown on the sidewalls of the NRs in samples S and T1-T3, respectively. Figures 10(i)-10(l) show the cross-sectional SEM images of the QW NR arrays in samples S and T1-T3, respectively. Here, on the central NR in each image, numbers 1-3 are marked for indicating the locations of local CL measurements. The NR heights of samples S, T1, and T2 are about the same at ~1.9 μm. That of sample T3 is larger at ~2.8 μm. Figures 11(a)-11(d) show the local CL spectra at the three locations for samples S and T1-T3, respectively, when the electron accelerating voltage is 5 kV. The spatial resolution of a local CL spectral measurement is 30 nm x 40 nm. Here, one can see that the emission intensity of the bottom portion or the first uniform sections in all the four samples are relatively weaker, when compared with those of other portions or sections. The CL spectral peak wavelengths at those three sidewall locations of the four samples are listed in rows 2-4 of Table 1. Although the sidewall QWs in all the samples are grown under the same MOCVD condition, here one can see that the emission wavelengths become longer in the upper uniform sections of the multi-section NRs. The CL spectral peak differences between locations 1 and 3 of the four samples are listed in row 5 of Table 1. Here, one can see that this spectral difference is larger in a multi-section NR. It increases from 4 nm in sample S to 22 nm in sample T1, to 38 nm in sample T2, and then to 46 nm in sample T3, indicating that the overall emission spectral width of sidewall QWs can become larger in a multi-section NR. A larger contrast of cross-sectional size in a multi-section NR can lead to a larger emission spectral width.

Figure 12 shows the normalized PL spectra of the QW NRs in samples S and T1-T3. The PL measurements are excited by a 406-nm laser of 5 mW in power. Here, one can see that the PL spectral

peak red-shifts in multi-section samples. Also, the spectral widths are increased in multi-section samples. The PL spectral peak wavelengths and FWHMs of those samples are listed in rows 6 and 7 of Table 1, respectively. Here, one can see that the PL spectral peak red-shifts by 47.4 nm from sample S to T3. Also, the spectral FWHM increases from 54.1 nm in sample S to 92.6 nm in sample T3. It is noted that the long-wavelength tail in the PL spectrum of sample S is caused by defect emission. If the defect emission intensity is kept at this level in sample T3, its contribution to the broad emission spectrum of this sample is unimportant. The PL spectral FWHM of 92.6 nm represents the broadest sidewall QW emission spectrum in an NR ever reported. Such results can be attributed to the different QW strain conditions and different constituent atom supply conditions between different sections in a multi-section NR. The weaker compressive strain in the sidewall QWs in an upper section can lead to higher indium incorporation for emitting light of a longer wavelength. It is noted that although the n-GaN NR core can be fully strain-relaxed in the whole NR [45], a smaller NR cross-sectional size can lead to a weaker compressive strain in the sidewall InGaN well layers such that In incorporation efficiency can be increased [41, 46, 47]. Meanwhile, with the smaller cross-sectional size in an upper section, the larger gap volume between neighboring NRs allows more supply of the constituent atoms at this height for forming thicker QWs in this section and hence emitting light of a longer wavelength [25]. It is noted that the aforementioned line-markers correspond to Ga-rich line structures, which may form defects for producing current leakage and light absorption when such an NR is used for LED application. Although single- and multi-section NRs with their sidewall-QW internal quantum efficiencies ranging between 14 and 21 % in the blue-green through green spectral range have been used for successfully fabricating LED arrays of reasonably high emission efficiencies [36, 48], the effect of the Ga-rich line-markers on emission efficiency is an issue deserving further investigation.

7. Summary

In summary, we have demonstrated the growth of regularly-patterned multi-section GaN NR arrays based on a pulsed growth technique with MOCVD. Such an NR with multiple sections of different cross-sectional sizes was formed by tapering a uniform cross section to another through the decrease of Ga supply duration stepwise for reducing the size of the catalytic Ga droplet. Contrast line-markers were discovered in either an SEM or a TEM image of an NR to illustrate the boundaries between two successive growth cycles in pulsed growth. It was found that a line-marker corresponded to a thin Ga-rich layer formed at the beginning of GaN precipitation of a pulsed-growth cycle. By analyzing the geometry variation of the line-marker, the morphology evolution in the growth of a multi-section NR, including a tapering process, was traced. During such a process, the slant facets first changed gradually from the {1-102}-plane in a section of a uniform cross-sectional size into the {1-101}-plane, and then returned to the {1-102}-plane when the next uniform section of a smaller cross section was formed. Such a morphology variation was controlled by the size of the catalytic Ga droplet and its coverage range on the slant facets at the top of an NR. The comparison of emission spectrum between single-, 2-, and 3-section GaN NRs with sidewall InGaN/GaN QWs indicated that a multi-section NR could lead to a significantly broader sidewall emission spectrum. The sidewall QWs in a 3-section QW NR array could emit light of >90 nm in spectral FWHM.

References:

1. Tu L W, Hsiao C L, Chi T W, Lo I, Hsieh K Y 2003 *Appl. Phys. Lett.* **82** 1601.
2. Chèze C, Geelhaar L, Jenichen B, Riechert H 2010 *Appl. Phys. Lett.* **97** 153105.
3. Lin H W, Lu Y J, Chen H Y, Lee H M, Gwo S 2010 *Appl. Phys. Lett.* **97** 073101.
4. Guo W, Zhang M, Banerjee A, Bhattacharya P 2010 *Nano Lett.* **10** 3355.
5. Guo W, Banerjee A, Bhattacharya P, Ooi B S 2011 *Appl. Phys. Lett.* **98** 193102.
6. Nguyen H P T, Djavid M, Woo S Y, Liu X, Connie A T, Sadaf S, Wang Q, Botton G A, Shih I, Mi Z 2015 *Sci. Rep.* **5** 8332.
7. Kawakami Y, Suzuki S, Kaneta A, Funato M, Kikuchi A, Kishino K 2006 *Appl. Phys. Lett.* **89** 163124.
8. Kishino K, Sekiguchi H, Kikuchi A 2009 *J. Cryst. Growth* **311** 2063.
9. Yanagihara A, Ishizawa S, Kishino K 2014 *Appl. Phys. Express* **7** 112102.
10. Albert S, Bengoechea-Encabo A, Kong X, Sanchez-Garcia M A, Calleja E, Trampert A 2013 *Appl. Phys. Lett.* **102** 181103.
11. Gačević Ž, Sánchez D G, Calleja E 2015 *Nano Lett.* **15** 1117.
12. Song T, Park W I, Paik U 2010 *Appl. Phys. Lett.* **96** 011105.
13. Chen X J, Perillat-Merceroz G, Sam-Giao D, Durand C, Eymery J 2010 *Appl. Phys. Lett.* **97** 151909.

14. Ra Y H, Navamathavan R, Park J H, Lee C R 2013 *CrystEngComm* **15** 1874.
15. Ra Y H, Navamathavan R, Park J H, Lee C R 2013 *Nano Lett.* **13** 3506.
16. Ra Y H, Navamathavan R, Yoo H I, Lee C R 2014 *Nano Lett.* **14** 1537.
17. Tessarek C, Heilmann M, Butzen E, Haab A, Hardtdegen H, Dieker C, Spiecker E, Christiansen S 2014 *Cryst. Growth Des.* **14** 1486.
18. De Luna Bugallo A, Rigutti L, Jacopin G, Julien F H, Durand C, Chen X J, Salomon D, Eymery J, Tchernycheva M 2011 *Appl. Phys. Lett.* **98** 233107.
19. Jacopin G, De Luna Bugallo A, Lavenus P, Rigutti L, Julien F H, Zagonel L F, Kociak M, Durand C, Salomon D, Chen X J, Eymery J, Tchernycheva M 2012 *Appl. Phys. Express* **5** 014101.
20. Hersee S D, Sun X, Wang X 2006 *Nano Lett.* **6** 1808.
21. Wang X, Sun X, Fairchild M, Hersee S D 2006 *Appl. Phys. Lett.* **89** 233115.
22. Chen Y S, Shiao W Y, Tang T Y, Chang W M, Liao C H, Lin C H, Shen K C.,Yang C C, Hsu M C, Yeh J H, Hsu T C 2009 *J. Appl. Phys.* **106** 023521.
23. Tang T Y, Shiao W Y, Lin C H, Shen K C, Huang J J, Ting S Y, Liu T C, Yang C C, Yao C L, Yeh J H, Hsu T C, Chen W C, Chen L C 2009 *J. Appl. Phys.* **105** 023501.
24. Liao C H, Chang W M, Chen H S, Chen C Y, Yao Y F, Chen H T, Su C Y, Ting S Y, Kiang Y W, Yang C C 2012 *Opt. Express* **20** 15859.
25. Liao C H, Chang W M, Yao Y F, Chen H T, Su C Y, Chen C Y, Hsieh C, Chen H S, Tu C G, Kiang Y W, Yang C C 2013 *J. Appl. Phys.* **113** 054315.
26. Bergbauer W, Strassburg M, Kölper C, Linder N, Roder C, Lähnemann J, Trampert A, Fündling S, Li S F, Wehmann H H, Waag A 2011 *J. Cryst. Growth* **315** 164.
27. Bergbauer W, Strassburg M, Kölper C, Linder N, Roder C, Lähnemann J, Trampert A, Fündling S, Li S F, Wehmann H H, Waag A 2010 *Nanotechnology* **21** 305201.
28. Wang X, Li S F, Mohajerani M S, Ledig J, Wehmann H H, Mandl M, Strassburg M, Steegmüller U, Jahn U, Lähnemann J, Riechert H, Griffiths I, Cherns D, Waag A 2013 Cr*yst Growth Des.* **13** 3475.
29. Liao C H, Tu C G, Chang W M, Su C Y, Shih P Y, Chen H T, Yao Y F, Hsieh C, Chen H S, Lin C H, Yu C K, Kiang Y W, Yang C C 2014 *Opt. Express* **22** 17303.
30. Lin Y T, Yeh T W, Dapkus P D 2012 *Nanotechnology* **23** 465601.
31. Yeh T W, Lin Y T, Stewart L S, Dapkus P D, Sarkissian R, O'Brien J D, Ahn B, Nutt S R 2012 *Nano Lett.* **12** 3257.
32. Lin Y T, Yeh T W, Nakajima Y, Dapkus P D 2014 *Adv. Funct. Mater.* **24** 3162.
33. Jung B O, Bae S Y, Kato Y, Imura M, Lee D S, Honda Y, Amano H 2014 *CrystEngComm* **16** 2273.
34. Jung B O, Bae S Y, Kim S Y, Lee S, Lee J Y, Lee D S, Kato Y, Honda Y, Amano H 2015 *Nano Energy* **11** 294.
35. Chen H S, Yao Y F, Liao C H, Tu C G, Su C Y, Chang W M, Kiang Y W, Yang C C 2013 *Opt. Lett.* **38** 3370.
36. Tu C G, Liao C H, Yao Y F, Chen H S, Lin C H, Su C Y, Shih P Y, Chen W H, Zhu E, Kiang Y W, Yang C C 2014 *Opt. Express* **22** A1799.
37. Chang J R, Chang S P, Li Y J, Cheng Y J, Sou K P, Huang J K, Kuo H C, Chang C Y 2012 *Appl. Phys. Lett.* **100** 261103.
38. Koester R, Hwang J S, Salomon D, Chen X, Bougerol C, Barnes J P, Dang D L S, Rigutti L, de Luna Bugallo A, Jacopin G, Tchernycheva M, Durand C, Eymery J 2011 *Nano Lett.* **11** 4839.
39. Riley J R, Padalkar S, Li Q, Lu P, Koleske D D, Wierer J J, Wang G T, Lauhon L J 2013 *Nano Lett.* **13** 4317.
40. Tchernycheva M, Lavenus P, Zhang H, Babichev A V, Jacopin G, Shahmohammadi M, Julien F H, Ciechonski R, Vescovi G, Kryliouk O 2014 *Nano Lett.* **14** 2456.
41. Kuykendall T R, Schwartzberg A M, Aloni S 2015 *Adv. Mater*. **27** 5805.
42. Chen C P, Ganguly A, Lu C Y, Chen T Y, Kuo C C, Chen R S, Tu W H, Fischer W B, Chen K H, Chen L C 2011 *Anal. Chem.* **83** 1938.
43. Li Y, Xiang J, Qian F, Gradecak S, Wu Y, Yan H, Blom D A, Lieber C M 2006 *Nano Lett.* **6** 1468.
44. Tchernycheva M, Messanvi A, de Luna Bugallo A, Jacopin G, Lavenus P, Rigutti L, Zhang H, Halioua Y, Julien F H, Eymery J, Durand C 2014 Nano Lett. **14** 3515.
45. Hugues M, Shields P A, Sacconi F, Mexis M, Auf der Maur M, Cooke M, Dineen M, Di Carlo A, Allsopp D W E, Zuniga-Perez J 2013 *J. Appl. Phys.* **114** 084307.
46. Li S, Waag A 2012 *J. Appl. Phys.* **111** 071101.
47. Wu Y R, Chiu C H, Chang C Y, Yu P C, Kuo H C 2009 *IEEE J. Sel. Top. Quant. Electron.* **15** 1226.
48. Tu C G, Yao Y F, Liao C H, Su C Y, Hsieh C, Weng C M, Lin C H, Chen H T, Kiang Y W, Yang C C 2015 *Opt. Express* **23** 21919.

Table 1 CL and PL measurement results of samples S and T1-T3.

Sample	S	T1	T2	T3
CL spectral peak wavelength at location 1 (nm)	472	488	506	532
CL spectral peak wavelength at location 2 (nm)	470	478	498	516
CL spectral peak wavelength at location 3 (nm)	468	466	468	486
CL spectral peak difference between locations 1 and 3 (nm)	4	22	38	46
PL spectral peak wavelength (nm)	476.1	490.1	504.9	523.5
PL spectral FWHM (nm)	54.1	64.6	72.8	92.6

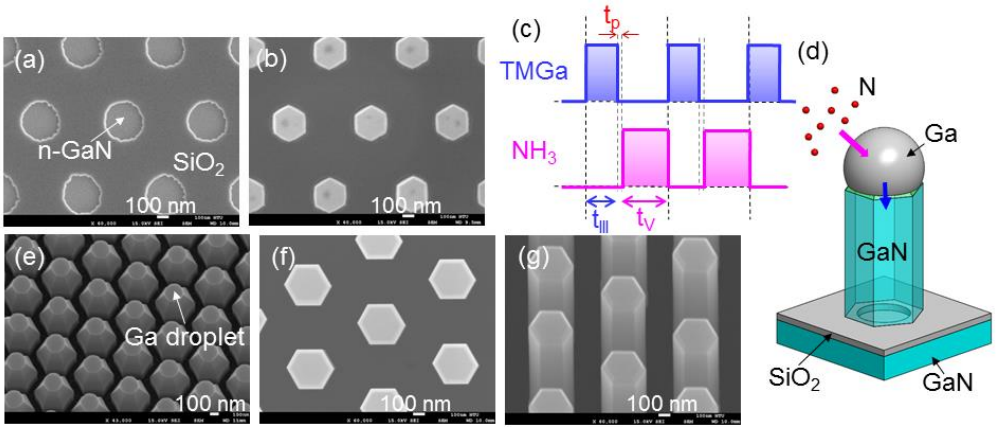

Fig. 1 (a): Plan-view SEM image of a hole pattern for selective growth. (b): Plan-view SEM image of an NR-growth template after the hole-filling process. (c): Modulated supply patterns of TMGa and NH_3 in pulsed growth for an NR of a uniform cross section. (d): Schematic demonstration of the pulsed growth process with a Ga droplet at the top of a GaN NR for serving as the growth catalyst. (e): Tilted SEM image showing a Ga droplet at the top of an NR during the early stage of pulsed growth. (f) and (g): Plan-view and tilted SEM images, respectively, of a single-section n-GaN NR array.

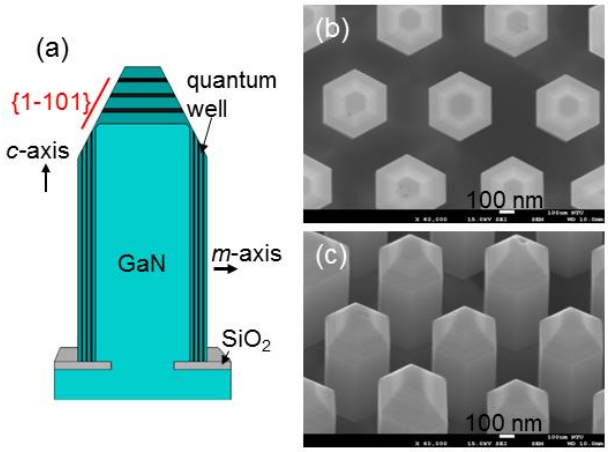

Fig. 2 (a): Schematic demonstration of an NR after QW deposition, including *c*-plane top-face QWs and *m*-plane sidewall QWs. (b) and (c): Plan-view and tilted SEM images, respectively, of a QW NR array.

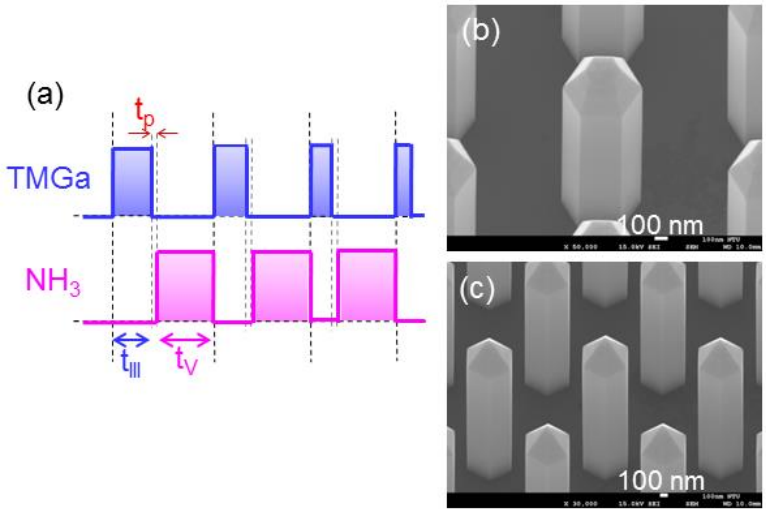

Fig. 3 (a): Modulated supply patterns of TMGa and NH_3 in pulsed growth for tapering an NR. (b): Tilted SEM image of an n-GaN NR with a tapering top formed with 3 cycles of 15-sec, 3 cycles of 10-sec, and then 6 cycles of 5-sec TMGa supplies. (c): Tilted SEM image of an n-GaN NR with a tapering top formed with 3 cycles of 15-sec, 3 cycles of 10-sec, and then 20 cycles of 5-sec TMGa supplies.

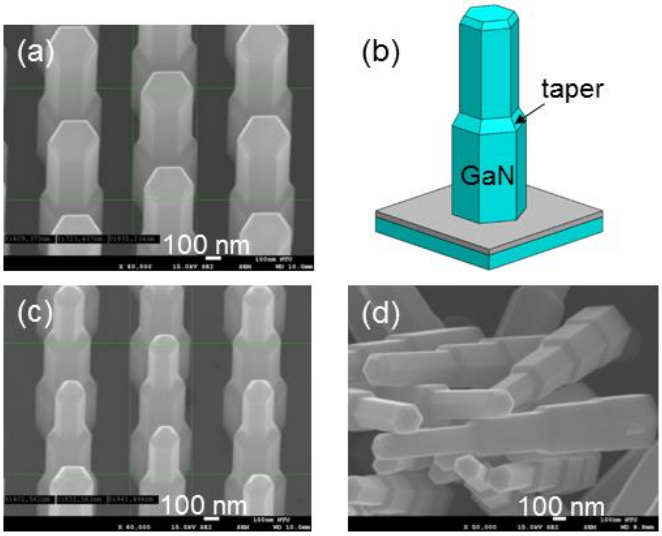

Fig. 4 (a): Tilted SEM image of a 2-section n-GaN NR array. (b): Schematic demonstration of a 2-section NR. (c): Tilted SEM image of a 3-section n-GaN NR array. (d): SEM image of fallen 4-section n-GaN NRs.

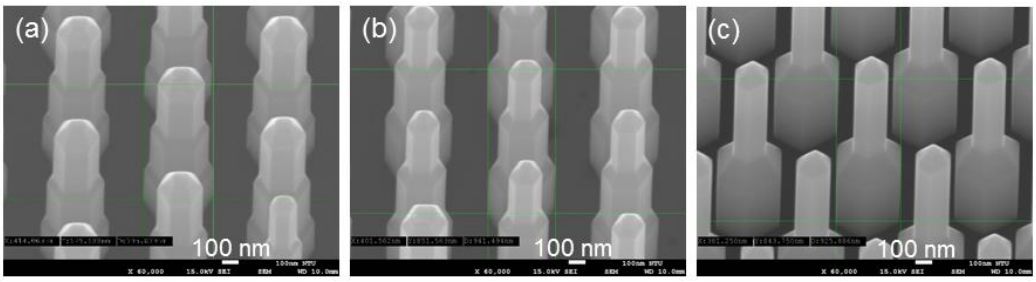

Fig. 5 (a): Tilted SEM image of a 3-section n-GaN NR array with each of the three tapering portions (including the top one) formed with 3 cycles of 15-sec, 3 cycles of 10-sec, and then 3 cycles of 5-sec TMGa supplies. (b): Similar to that in part (a) except that the 5-sec TMGa supply cycle number is 6. (c): Similar to that in part (a) except that the 5-sec TMGa supply cycle number is 9.

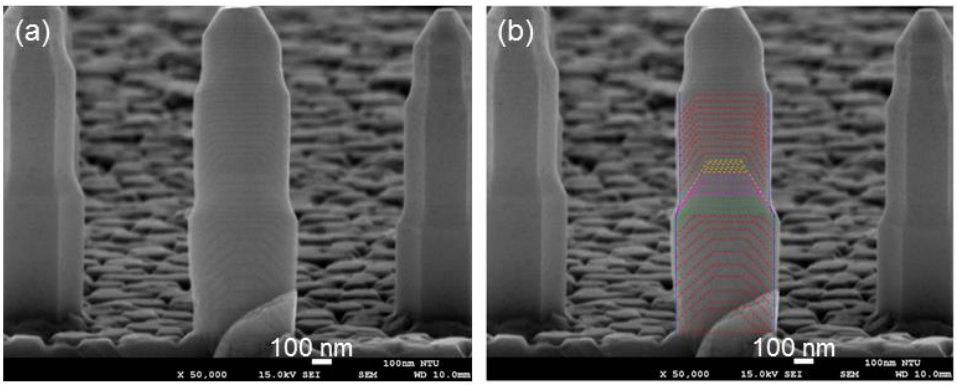

Fig. 6 (a): Cross-sectional SEM image of three 3-section QW NRs with the central one bisected to show the line-markers inside the NR. (b): Same SEM image as part (a) except that the line-markers are traced with dashed lines.

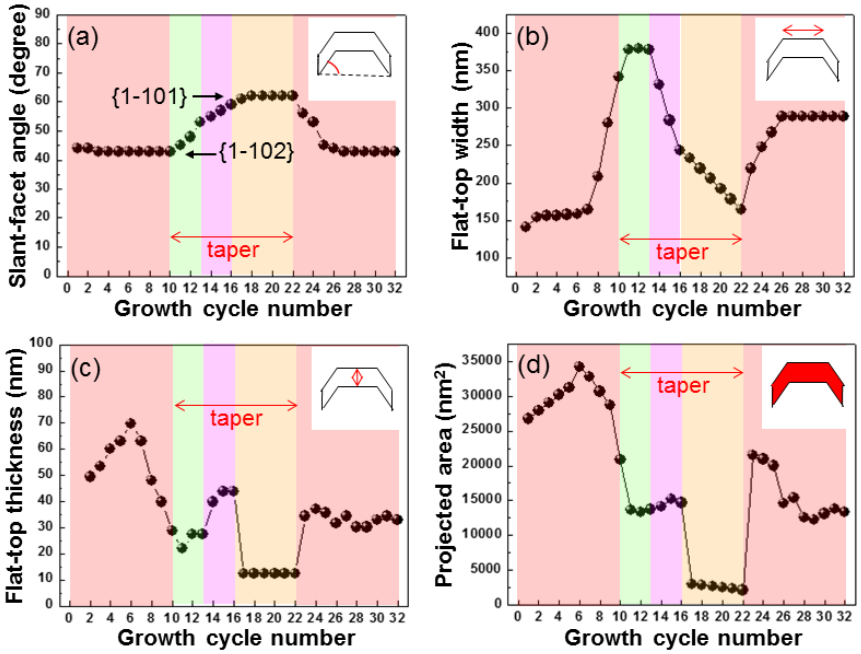

Fig. 7 (a)-(d): Variations of the slant-facet angle, flat-top width, flat-top thickness, and projected area, respectively, during the NR growth from the first to the second uniform section.

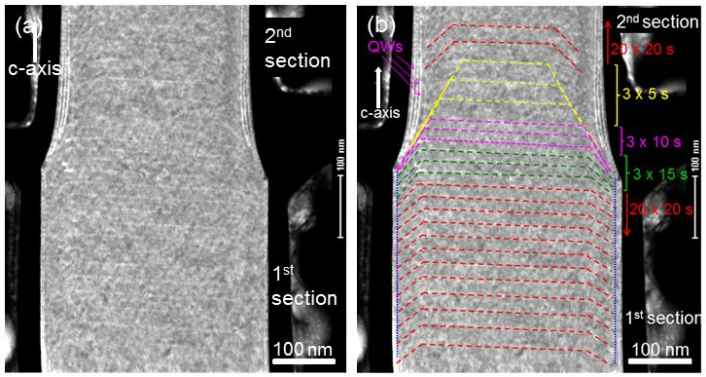

Fig. 8 (a): TEM HAADF image around the first tapering portion of a 3-section QW NR. The tapering process includes 3 cycles of 15-sec, 3 cycles of 10-sec, and then 3 cycles of 5-sec TMGa supplies. Each uniform section consists of 20 cycles of 20-sec TMGa supply. (b): Same TEM HAADF image as part (a) except that the white line-markers are traced with dashed lines.

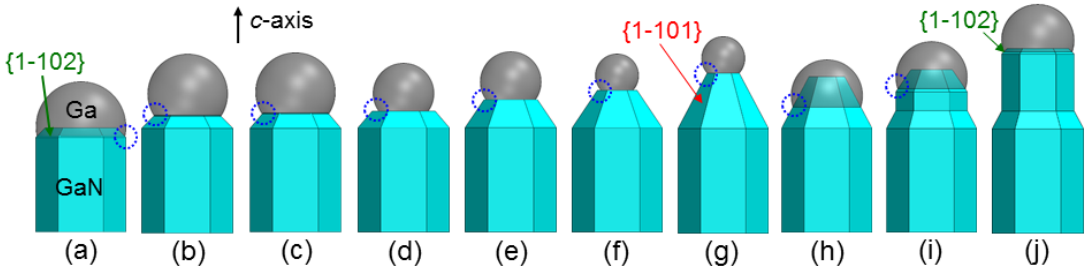

Fig. 9 (a)-(j): Schematic demonstration of the morphology evolution of an NR with the speculated Ga droplet geometry during the tapering process shown in Fig. 6(b).

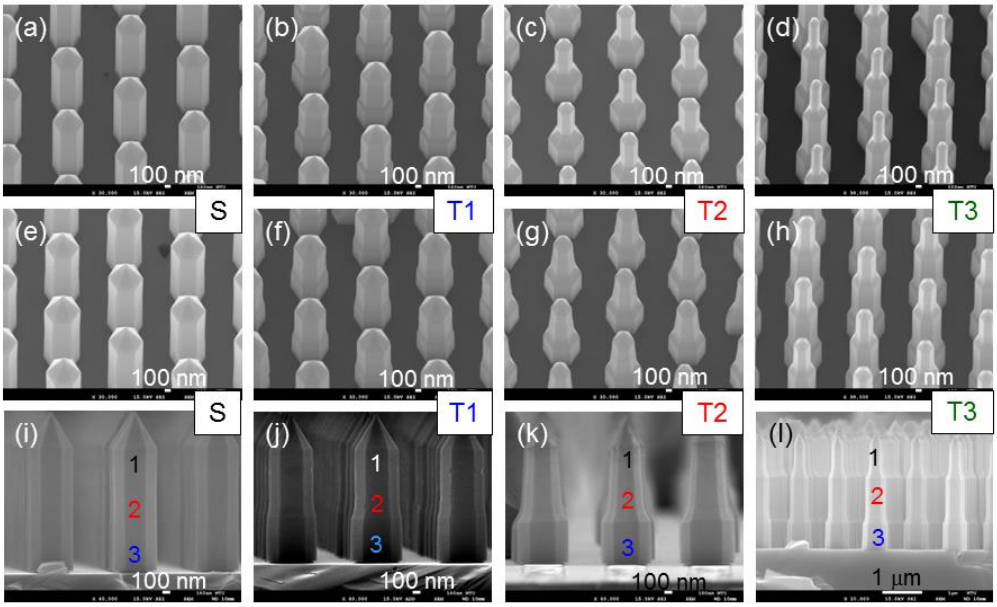

Fig. 10 (a)-(d): Tilted SEM images of a single-section (sample S), two 2-section (samples T1 and T2), and one 3-section (sample T3) n-GaN NR arrays. (e)-(h): Tilted SEM images after three periods of InGaN/GaN QWs are grown on the sidewalls of the n-GaN NRs in samples S and T1-T3, respectively. (i)-(l): Cross-sectional SEM images of the QW NR arrays in samples S and T1-T3, respectively. Numbers 1-3 are marked for indicating the locations of local CL measurements.

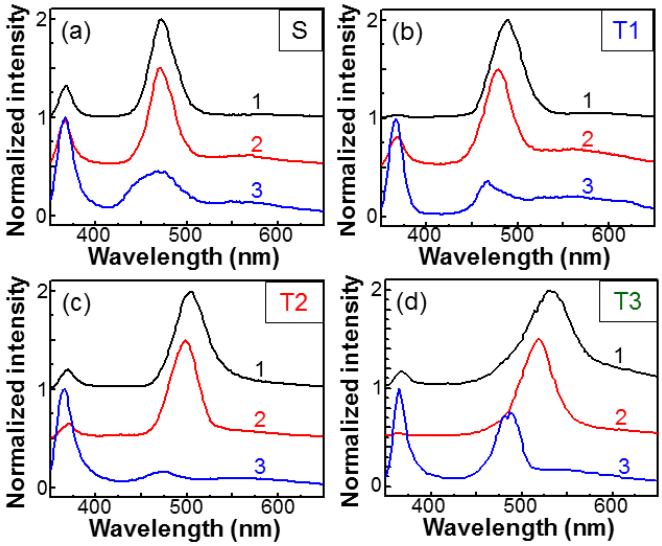

Fig. 11 (a)-(d): Local CL spectra at the three locations for samples S and T1-T3, respectively.

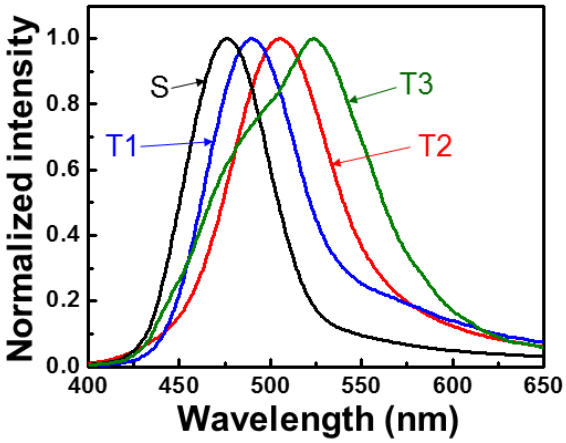

Fig. 12 Normalized PL spectra of the QW NR arrays in samples S and T1-T3.

Chapter 3: Growth model of a GaN nanorod with the pulsed-growth technique of metalorganic chemical vapor deposition

1. Introduction

Semiconductor nanorods (NRs) of high crystal quality are regarded as promising building blocks of future nanoelectronics [1], nanophotonics [2], and nanosensing [3] devices. GaN NRs with randomly distributed and regularly patterned structures have been grown with molecular beam epitaxy [4, 5] and metalorganic chemical vapor deposition (MOCVD) [6-10]. Among different techniques, the self-catalytic or self-induced NR formation is an attractive approach, in which the metal of the targeted nanorod material itself plays the function of catalyst. The self-induced approach is advantageous in many aspects. First, self-induced NRs do not suffer from a few drawbacks of the vapor-liquid-solid (VLS) growth mode, such as crystallographic polytypism [11, 12] and extrinsic-catalyst contamination [13]. Second, the self-induced approach can lead to a radical decrease of dislocation density caused by lattice mismatch [14, 15]. Although the self-induced method has been widely used for growing GaN NRs or nanowires, its growth mechanism has not been well understood yet. With the aforementioned advantages of the self-induced method, it deserves more advanced modeling for the growth process, particularly the nucleation steps, such that a better understanding can help in further growth development.

It has recently been shown that the GaN formation with self-induced nucleation starts the growth in the form of three-dimensional nanoislands, which subsequently evolve into NRs for energetic reasons. The anisotropy of surface energy has been identified as the predominant driving force such that the nucleation phase is expected to be driven by thermodynamics [16, 17]. A theoretical model that explains the growth and nucleation processes of GaN NR was proposed [18]. However, this model can only be applied to the self-induced continuous growth mode. By introducing the pulsed growth and selective-area growth techniques, a uniform array of GaN NR with an individually uniform cross-section and precise position control can be obtained [6-8, 19-21]. The influences of growth temperature, precursor injection, and interruption duration on NR location, orientation, length, and diameter have been studied experimentally. Under these growth conditions, although schematic pictures for GaN NR growth have been demonstrated, no physical modelling or quantitative evaluation was reported [21].

In this chapter, we propose a theoretical model for interpreting the experimental observation of self-induced GaN NR formation based on the selective-area and pulsed growth techniques with MOCVD [6, 7, 9, 22-25]. In such a growth result, quasi-periodic dark line-markers distributed along the NR growth direction were discovered in scanning electron microscopy (SEM) observation [25]. The line-markers provide us with a precise chronology of NR growth. Many NR growth details can be derived from the distribution of the line-markers. In this study, the variations of the radius and aspect ratio of the self-catalytic gallium droplet with time in a growth cycle are modeled and numerically demonstrated. The volume increment of GaN NR in each growth cycle is calculated based on our model and compared with the experimental data. Meanwhile, the angle variation of an NR slant facet during a tapering process is analyzed.

2. Experimental observation and growth model

In the pulsed mode for GaN NR growth, the gallium and nitrogen sources are switched on and off alternatively. During gallium supply, a gallium droplet is formed at the top of an NR. The melting gallium droplet absorbs nitrogen and precipitates GaN at its bottom for increasing the height of the NR during nitrogen supply. When the supply durations of both gallium and nitrogen are individually kept constants, a single-section NR of a uniform cross section can be fabricated. If we decrease the gallium supply duration while maintaining a constant nitrogen supply duration, a tapering section of decreasing cross-sectional size is formed. Based on such a tapering process, a multi-section NR with different cross-sectional sizes in different seections can be fabricated [24, 25]. From the cross-sectional scanning electron microscopy image of an NR, quasi-periodic dark line-markers can be observed in a uniform NR section with the periodicity in coincidence with the NR growth cycles [25]. The line-markers provide us with the information about the morphology evolution during the pulsed growth process. They can give us the clues for investigating the growth mechanism of such an NR structure.

Based on the experimental observations, we propose a growth model as schematically demonstrated in Figs. 1(a) and 1(b). Figure 1(a) shows the formation process of the gallium droplet during gallium supply. The diffusion of gallium adatoms from the substrate and NR sidewalls to the droplet surface is schematically shown. The region on the substrate in the NR gap region, in which gallium adatoms can migrate onto the NR sidewalls, is limited to a circular area with a length of λ_s

outreaching from the center of a sidewall in the bottom plane. The gallium droplet serves as a gallium reservoir for interacting with arriving nitrogen species. To formulate the growth model, the incident gallium flux is defined as J_{Ga}, the radius of the NR cross-sectional circumscription is defined as R (the same as the width of one of the six sidewalls), the height of the gallium droplet is designated as h_L, as depicted in Fig. 1(b). During gallium supply, a sphere-like gallium droplet is formed at the NR top with a fixed contact angle β with respect to the NR top face, i.e., the c-plane, but with an increasing radius r [see Fig. 1(b)], which is defined in the circular area at the interface between NR and gallium droplet. As shown in Fig.1(a), it is assumed that at the end of a gallium supply duration, the gallium droplet just covers the entire NR top, including the flat c-plane face and the slant facets ({1-102}-plane). This assumption is reasonable since the cross-sectional size of the NR can be self-adjusted at the beginning of NR growth for reaching this condition. During nitrogen supply, GaN can be precipitated for increasing the height of an NR. According to Glas's model [26], GaN nucleation starts from the three-phase junction, i.e., the edge of the NR top. During GaN growth, the lateral size of the gallium droplet is preserved while the aspect ratio, defined as $\eta = h_L / r$, and contact angle β decrease. Therefore, the gallium droplet inflates and deflates periodically in the pulsed growth mode. During nitrogen supply, GaN precipitation at the flat interface between NR and gallium droplet occurs when the supersaturation condition of nitrogen in liquid gallium is reached. This behavior implies that the top facet is stabilized as long as the difference in chemical potential between the liquid droplet and top facet is smaller than the nucleation barrier [27, 28]. Once the nucleation event on the top facet occurs, the supersaturation in liquid droplet builds up slowly again until the next nucleation event takes place. At the end of a nitrogen supply duration, a GaN layer, covering the top flat face and the slant facets at the edge, is formed.

In the puled-growth process, the NR growth results from the combined effect of both VLS and VS mechanisms. During nitrogen supply, the gallium droplet deflates as nitrogen atoms impinge onto the droplet surface for precipitating GaN. This process proceeds with the VLS growth mode. However, there is no diffusion of nitrogen adatoms from the NR sidewalls into the droplet due to the highly volatile character of group V species [26]. When the gallium droplet is depleted, residual nitrogen atoms exist around an NR. Such residual nitrogen atoms can lead to the formation of a gallium-rich line-marker during gallium supply in the next cycle, as explained in the following. After gallium supply is turned on, an incubation time is required before a surface deposition can occur at the NR top facet. During the incubation period, gallium atoms impinge onto and desorb from an NR and the substrate without creating a substantial semiconductor or metal island [29]. In situ surface observation of X-ray diffraction [30] revealed the dominant desorption of gallium adatoms from sample surface and negligible incorporation during the incubation stage. As to our GaN NR growth, gallium adatoms are quickly accumulated at the NR top through direct flux impingement and sidewall diffusion to the NR top facet during the incubation period. The gallium adatom accumulation leads to the gallium-rich condition on the NR top facet. Then, the gallium adatoms interact with the residual N atoms for growing a gallium-rich GaN line-marker layer via the VS growth mechanism. In this process, the more and more accumulated gallium adatoms form a gallium droplet on the top of the deposited gallium-rich line-marker. The size of the gallium droplet increases with the coverage area of the gallium-rich line-marker layer. In other words, the gallium droplet inflates together with the expansion of the VS-grown line-marker area. Such a process in a growth cycle is schematically demonstrated in Figs. 2(a)-2(f). Because of the symmetry nature, the formation of the gallium droplet starts from the center of the NR top facet. In this situation, the droplet maintains its aspect ratio during its growth under gallium supply. However, the aspect ratio of the droplet decreases while fixing its base radius under nitrogen supply, as experimentally observed by other groups [31, 32]. Figures 2(a)-2(c) show the process of gallium-droplet deflation for GaN precipitation through the VLS mode during nitrogen supply. Figures 2(d)-2(f) show the processes of line-marker formation through the VS mode and then the inflation of gallium droplet. In Figs. 2(g)-2(i), we schematically demonstrate the coverage ranges of the gallium droplets at the ends of the gallium supply durations of 5, 10/15, and 20 sec, respectively.

3. Formulations and numerical results of GaN growth

In the pulsed growth process, the gallium (TMGa) and nitrogen (NH_3) sources are switched on and off alternatively, as schematically demonstrated in Fig. 3. Although many parameter values may vary with temperature, for simplicity, we assume a fixed growth temperature throughout our analysis. To model such a growth process, the time-dependent nitrogen supply pattern can be described by a square-wave function with the Heaviside step function, $u(t)$, as

$$W(t)=\sum_{n=0}^{N}\left\{u\left[t-(n+1)T_i+t_V\right]-u[t-(n+1)T_i\right\} \quad (1)$$

Here, T_i stands for a growth cycle duration and t_V is the duration of NH_3 supply in one cycle. In other words, $T_i = t_{III} + t_V + t_p$, where t_{III} and t_p are the supply duration of TMGa and the duration of the supply pause between TMGa and NH3 supplies, respectively. In our model, we neglect the supply pause duration, t_p (~1 sec). The gallium supply pattern is 1 – W(t). Because of the low solubility of group V species in group III liquids, nitrogen is dissolved in the melting gallium only with a small concentration [26]. Therefore, GaN precipitation is mainly controlled by the nitrogen supply condition. The addition of nitrogen to the gallium droplet is determined by the factors of its flux impinging onto the gallium droplet surface and NR environment. On the other hand, the annihilation of absorbed nitrogen from the droplet, which occurs through precipitation of GaN and evaporation, is determined by the nitrogen concentration in the droplet and temperature. As for the VS growth mode, the equivalent growth rate in the radial direction is the same as that of gallium droplet expansion. In this situation, the temporal variation of the total number of GaN bi-atom in solid state grown through the VS mode, $N_{GaN,VS}$, can be expressed as

$$\frac{dN_{GaN,VS}}{dt}\approx\frac{2\pi r h_s}{\Omega_{GaN}}\frac{dr}{dt}\left[1-W(t)\right]. \quad (2)$$

Here, h_s is the line-maker thickness, r is the time-dependent droplet radius, and Ω_{GaN} is the volume of a GaN pair. For simplicity, we assume that the VS growth rate linearly increases with time. In the process of time-dependent inflation of gallium droplet during gallium supply, the number of gallium atoms in the droplet, N_{Ga}, is given by

$$\frac{dN_{Ga}}{dt}=\left[k_{Ga,L}J_{Ga}f_S(\beta)\pi r^2+N_{diff}\left(1-\frac{\theta_l}{\theta_f}\right)-J_{Ga}^{e}f_S(\beta)\pi r^2\right]\left[1-W(t)\right]-\frac{dN_{GaN,VS}}{dt}. \quad (3)$$

Because the decrease rate of gallium atom in the droplet equals to the increment rate of GaN atom-pair in the solid state through the VLS mode, $N_{GaN,VLS}$, we can write

$$\frac{dN_{Ga}}{dt}=-\frac{dN_{GaN,VLS}}{dt}=-\left[k_{N,L}J_N(1+\varepsilon)-J_N^e-J_{Ga}^e\right]f_S(\eta)\pi R_b^2W(t). \quad (4)$$

Here, $R_b=r(t_{III})$ is the droplet radius at t_{III}, i.e., at the end of a gallium supply duration. The diffusion-induced term $N_{diff}\approx k_{Ga,S}J_{Ga}(3\sqrt{3}R^2/2-\pi r^2)+k_{Ga,S}J_{Ga}6R\lambda_{Ga}$ contains the contributions of the impingements of gallium atoms onto the top facet (the first term) and sidewalls (the second term) with gallium diffusion length λ_{Ga}. The notations $k_{Ga,L}$, $k_{N,L}$, and $k_{Ga,S}$ represent the sticking probabilities of gallium and nitrogen atoms to the gallium liquid droplet (subscript L) and NR sidewall surface (subscript S), respectively. Meanwhile, J_{Ga} and J_N (J_N^e and J_{Ga}^e) are the impinging (desorbing) fluxes of gallium and nitrogen atoms, respectively, onto (from) the droplet. The ratio of gallium activities in the liquid phase (θ_l) and on the NR sidewalls (θ_f) accounts for the reverse diffusion flux from the droplet [15, 18]. The surface area of the gallium droplet with the contact angle β or aspect ratio η is given by $\pi r^2 f_S(\beta)=2(\sin\beta)^{-2}(1-\cos\beta)\pi r^2=\pi r^2(1+\eta^2)$, where $f_S(\beta)$ is a geometrical function for the droplet surface. Also, the geometric function for the droplet volume is $f_V(\beta)=(1-\cos\beta)(2+\cos\beta)/[(1+\cos\beta)\sin\beta]$ or $f_V(\eta)=\eta(3+\eta^2)/2$. The coefficient ε takes the competing factor for atom adsorption against the neighboring NRs (the shadowing effect) into account. The liquid volume of the gallium droplet is given by $V_{Ga}=\Omega_{Ga}N_{Ga}=(\pi r^3/3)f_V(\beta)$, where Ω_{Ga} is the volume of a gallium atom in liquid phase, which equals to $\Omega_{Ga}=0.02nm^3$. Using equations (3) and (4), we obtain the equations for the volume of the gallium droplet during droplet inflation as

$$\frac{dV_{Ga}}{dt}=\Omega_{Ga}\left[\left(k_{Ga}J_L-\overline{G}aJ^e\right)f_{Ga}(\beta)\pi r^2+N_{diff}\left(1-\frac{\theta_l}{\theta_f}\right)-\frac{2\pi r h_s}{\Omega_{GaN}}\frac{dr}{dt}\right]\left[1-W(t)\right], \quad (5)$$

and during droplet deflation as

$$\frac{dV_{Ga}}{dt}=-\Omega_{Ga}\left[k_{N,L}J_N(1+\varepsilon)-J_N^e-J_{Ga}^e\right]f_S(\eta)\pi R_b^2W(t). \quad (6)$$

By introducing the effective flux $J_3=k_{Ga,L}J_{Ga}$, $J_5=k_{N,L}J_N(1+\varepsilon)-J_N^e$ and the weighted coefficient of gallium diffusion flux $D=k_{Ga,S}(1-\theta_l/\theta_f)/k_{Ga,L}$, and by considering the relation of

$dV_{Ga}/dt = \pi r^2 f_V(\beta)\, dr/dt$ or $dV_{Ga}/dt = \pi R_b^3 \left(1+\eta^2\right) d\eta/2dt$, equations (5) and (6) can be simplified to become

$$\frac{dr}{dt} = \left[A\left(1 - \frac{J_{Ga}^e}{J_3}\right) + \frac{B}{r^2}(3\sqrt{3}R^2/2 - \pi r^2 + 6R\lambda_{Ga}) \right] / \left(\frac{C}{r}+1\right)\left[1 - W(t)\right] \tag{7}$$

and

$$\frac{d\eta}{dt} = -\frac{2v_{Ga}}{R_b}\left(\frac{J_5}{J_3} - \frac{J_{Ga}^e}{J_3}\right) W(t) \cdot \tag{8}$$

Here, coefficients *A*, *B*, and *C* are defined as

$$A = \frac{v_{Ga} f_S(\beta)}{f_V(\beta)}, \quad B = \frac{D v_{Ga}}{\pi f_V(\beta)}, \text{ and } \quad C = \frac{2\Omega_{Ga} h_s}{\Omega_{GaN} f_V(\beta)}, \tag{9}$$

where $v_{Ga} = J_3 \Omega_{Ga}$ is the effective deposition rate of gallium.

In Fig. 4, we show the numerical results of the gallium droplet radius, *r*, (with the left ordinate and continuous curves) and aspect ratio, η, (with the right ordinate and dashed curves) as functions of time under the TMGa supply process of 20 sec in duration for 3 cycles, 15 sec for 3 cycles, 10 sec for 3 cycles, 5 sec for 5 cycles, and then 20 sec in duration for 3 cycles with the TMGa flow rate reduced to 70 % while the supply duration of NH_3 of a constant flow rate is fixed at 30 sec. The results are obtained from equations 7 and 8. This TMGa supply process has been used for an experimental implementation to grow a multi-section GaN NR [25]. In Fig. 4, we can see that the growth rate of the gallium droplet is very high at the early stage of gallium supply due to the gallium adatom diffusion from the NR top facet into the droplet at the top-facet center. As the droplet inflates, the un-occupied area of the top facet decreases such that the contribution of diffused gallium adatom from the top facet diminishes, resulting in the slow-down of droplet growth. At the end of a gallium supply duration of 20 sec, the base radius of the droplet reaches 250 nm, which is close to the radius of NR cross-section, *R*. This result means that all the six slant facets are covered by the gallium droplet. Also, at the end of such a gallium supply duration, the aspect ratio of the droplet is 0.25. The aspect ratio almost linearly decreases to zero with time during nitrogen supply with the fixed base radius at its maximum value (not shown in Fig. 4) [31, 32]. It is assumed that the gallium droplet is completely used up in a nitrogen supply duration. This is the case in experimental implementations, in which the length of a grown NR is not increased when t_V is set to be larger than 30 sec.

The TMGa and NH_3 supply processes shown in Fig. 3 can result in the growth of a tapering section for the transition from a uniform section to another of a smaller cross section size. As shown in Fig. 4, in the tapering process, the maximum base radius of the gallium droplet decreases with gallium supply duration. In this situation, the area of the flat top facet is reduced and that of a slant facet is increased. As shown in Fig. 4, the maximum base radii for the 5 cycles of 5-sec gallium supply are marked with small red circles. The decreasing trend of the marked maximum base radius is caused by the reduction of the gallium adatom collection area from NR sidewalls since its sidewall diffusion length, λ_f, is fixed and the slant facet becomes larger. Also, as shown in Fig. 4, different from that with 20-sec gallium supply in the first three cycles, the aspect ratios in all cycles of 15-, 10-, 5-, and 20-sec (with 70 % flow rate) gallium supplies are all the same at 0.19. This is so because under those conditions, the gallium droplet becomes smaller and does not cover the slant facets. In this situation, the contact angle, β, related to the aspect ratio becomes smaller and is fixed.

As mentioned earlier, the growth of a GaN NR in each cycle is a combined effect of the VS and VLS modes. The volume of grown GaN, V_{GaN}, can be expressed as

$$\begin{aligned} \frac{dV_{GaN}}{dt} &= \Omega_{GaN}\left(\frac{dN_{GaN,VS}}{dt} + \frac{dN_{GaN,VLS}}{dt}\right) \\ &= 2\pi r h_s \frac{dr}{dt}\left[1 - W(t)\right] - \frac{\Omega_{GaN}}{\Omega_{Ga}}\left(\frac{J_5}{J_3} - \frac{J_{Ga}^e}{J_3}\right) v_{Ga} f_S(\eta) \pi R_b^2 W(t) \end{aligned} \tag{10}$$

where $\Omega_{GaN} = 0.0225 nm^3$. Figure 5 shows the numerical results (represented by the diamond symbols) of the GaN volume grown per growth cycle, obtained from equation (10). The vertical bars represent the corresponding data obtained from experiment [25]. The parameters used for numerical computation include $v_{Ga} = 2.4 nm/s$, $J_5/J_3 = 3.2$, $J_{Ga}^e/J_3 = 0.3$, $\lambda_{Ga} = 28 nm$, β = 27° and 20° for t_{III} =20 sec and t_{III} = 15, 10, 5 sec, respectively. Here, the numerical results are quite consistent with the experimental data. Figure 6 shows the contribution percentages of the VS mode to the total grown GaN volumes in

various growth cycles. Here, one can see that the VS-growth contribution percentage generally increases with decreasing gallium supply duration or TMGa flow rate. This is so because the gallium droplet becomes smaller when the gallium supply duration is reduced or TMGa flow rate is decreased such that the VLS-growth contribution becomes smaller. Although the area of the VS-growth line-marker is also reduced with the size of the gallium droplet based on our model, if the line-marker thickness is fixed, the square-dependence of the line-marker area is less sensitive to dimension change, when compared to the cubic-dependence of the gallium-droplet volume or VLS-grown GaN volume. Therefore, as the gallium droplet size is reduced, the relative contribution of VS-growth becomes larger. The clear increasing trend of VS-growth contribution among the five 5-sec gallium supply cycles in Fig. 6 is consistent with the corresponding decreasing trend of the maximum droplet base radius shown in Fig. 4.

4. Angle variation of nanorod slant facet

A multi-section GaN NR of different cross-sectional sizes in different sections can be formed by changing the gallium supply duration while fixing the nitrogen supply duration. The formation of the tapering section is crucially important for the growth of the next uniform section. During the tapering process, the tilt angle of a slant facet, φ, changes from ~43º to ~62º, i.e., transition from the {1-102}- to {1-101}-plane, as observed in our previous experimental work [25]. In the following, a physical model is established for explaining this process. The gallium adatom concentration on a slant facet of a GaN NR, denoted as $n(w)$ along the w coordinate (see Fig. 7), obeys the diffusion equation in the form of

$$D\frac{\partial^2 n(w)}{\partial w^2}-\frac{n(w)}{\tau}=0\,. \tag{11}$$

Here, D is the diffusion coefficient, and $-n(w)/\tau$ is the gallium adatom sink through either desorption or incorporation. Therefore, the effective lifetime is given by $1/\tau = 1/\tau_{des} + 1/\tau_{inc}$, where τ_{des} and τ_{inc} are the lifetimes of gallium adatom on a slant facet before desorption and incorporation, respectively. As shown in Fig. 7, the boundary conditions of the diffusion equation are chosen to be

$$J_{Ga}^{-}=-D6r(w,t)\partial n(w)/\partial w\big|_{w=0},\ n(w=L)=0. \tag{12}$$

Here, J_{Ga}^{-} is the desorption flux of gallium from the slant facet, and L is the distance between the droplet edge and the intersection point of the slant facet and an m-plane sidewall. With these boundary conditions, the solution for $n(w)$ is given by

$$n(w)=\frac{J_{Ga}^{-}\lambda}{6Dr_0}\left[\tanh\left(\frac{L}{\lambda}\right)\cosh\left(\frac{w}{\lambda}\right)-\sinh\left(\frac{w}{\lambda}\right)\right]. \tag{13}$$

Here, $\lambda=\sqrt{D\tau}$ is the gallium adatom diffusion length on the slant facet, r_0 is the horizontal distance from the NR center to the droplet edge. The increment of the grown GaN volume on the slant facet at the distance w from the droplet edge is given by

$$\frac{6r(w,t)d[r(w,t)\sin\varphi(t)]dw}{\Omega_{GaN}}=\frac{n(w)}{\tau_{inc}}6r(w,t)dwdt\,. \tag{14}$$

As a result, we have the following equation for the GaN growth rate on a slant facet as

$$\frac{\partial[r(w,t)\sin\varphi(t)]}{\partial t}=\frac{\Omega_{GaN}}{\tau_{inc}}n(w) \tag{15}$$

The integration of equation (15) with the boundary conditions $r(0,0)=r_0$ and $r(w,0)=r_0+w\cos\varphi_0$ gives the expression for the NR radius with coordinate w at the instant t as

$$r(w,t)=r_0+w\cos\varphi_0+\frac{\Omega_{GaN}}{\sin\varphi(t)\tau_{inc}}\int_0^t n(w)dt' \tag{16}$$

With $J_{Ga}^{-}=6r_0C_{Ga}hD/(\Omega_{GaN}\lambda)$,[33] Eq. (16) can be rewritten as

$$r(w,t)=r_0+w\cos\varphi_0+\frac{hC_{Ga}t}{\sin\varphi(t)\tau_{inc}}\left[\tanh\left(\frac{L}{\lambda}\right)\cosh\left(\frac{w}{\lambda}\right)-\sinh\left(\frac{w}{\lambda}\right)\right] \tag{17}$$

Hence, the tilt angle of the slant facet with respect to the horizontal plane due to the incorporation of diffused gallium adatoms on the surface is calculated to give

$$\varphi(t_V)=\varphi_0+\arctan\left[\frac{r(0,t_V)-r_0}{L}\right]=\varphi_0+\arctan\left[\frac{hC_{Ga}t_V}{\sin\varphi(t_V)\tau_{inc}L}\tanh\left(\frac{L}{\lambda}\right)\right] \tag{18}$$

Here, $C_{Ga} \approx 1$ is the volume concentration of gallium atom in the droplet, $\varphi_0 = 43°$ is the initial angle of the slant facet before surface nucleation takes place, $h = 0.259$ nm is the GaN monolayer thickness, $t_V = 30$ sec is the duration of NH_3 supply, $L \approx 60$ nm is one-half the estimated length of a slant facet, $\lambda = 28$ nm is the gallium adatom diffusion length on a slant facet, and $\tau_{inc} = 3.1$ sec is the gallium adatom lifetime through incorporation. The continuous blue curve in Fig. 8 shows the numerical result of the slant facet angle at the end of a growth cycle, φ, as a function of growth cycle number during a transition process. Here, one can see that the angle increases from ~43 to ~62 degrees in 6 tapering growth cycles. The results are consistent with the experimental data, which are shown with red diamonds in Fig. 8 [25].

5. Summary

In summary, we have built a theoretical model for interpreting the VLS/VS-combined growth process of a GaN NR based on the pulsed growth mode with MOCVD. In particular, the VS-growth mechanism for forming the gallium-rich line-markers, which provided us with the growth chronology of an NR, was proposed by introducing an incubation time before surface deposition. The evolutions of gallium-droplet base radius and aspect ratio and the increase of precipitated GaN volume during the transition process of a two-section NR were formulated and numerically studied to show the consistent results with experimental data. The inflation of gallium droplet was governed by the direct impingement flux of gallium onto the droplet surface and adatom adsorption and diffusion on the substrate and vertical sidewalls. The droplet deflation or GaN precipitation was controlled by nitrogen influx onto the droplet surface. The relative contributions of the VLS and VS growths in such a transition process were also demonstrated. In fitting the numerical results with experimental data, a few important kinetic parameters could be deduced, including the effective diffusion length of gallium adatoms on an NR vertical sidewall at ~28 nm and the droplet contact angle at $\beta = 27°$ and 20° when $t_{III} = 20$ sec and $t_{III} = 15$, 10, 5 sec, respectively. Besides, the experimentally observed decrease of the slant-facet angle in transition from the {1-102}- to {1-101}-plane was modeled, formulated, and numerically simulated. The variation of the slant-facet angle was mainly controlled by the gallium desorption from the droplet and diffusion toward the NR sidewalls during the tapering process.

References

1. Bjork, M. T.; Ohlsson, B. J.; Thelander, C.; Persson, A. I.; Deppert, K.; Wallenberg, L. R.; Samuelson, L. *Appl. Phys. Lett.* **2002**, *81*, 4458.
2. Gradecak, S.; Qian, F.; Li, Y.; Park, H. G.; Lieber, C. M. *Appl. Phys. Lett.* **2005**, *87*, 173111.
3. Hayden, O.; Zheng, G. F.; Agarwal, P.; Lieber, C. M. *Small* **2007**, *3*, 2048.
4. Guo, W.; Zhang, M.; Banerjee, A.; Bhattacharya, P. *Nano Lett.* **2010**, *10*, 3355.
5. Kawakami, Y.; Suzuki, S.; Kaneta, A.; Funato, M.; Kikuchi, A.; Kishino, K. *Appl. Phys. Lett.* **2006**, *89*, 163124.
6. Liao, C. H.; Chang, W. M.; Chen, H. S.; Chen, C. Y.; Yao, Y. F.; Chen, H. T.; Su, C. Y.; Ting, S. Y.; Kiang, Y. W.; Yang, C. C. *Opt. Express* **2012**, *20*, 15859-15871.
7. Liao, C. H.; Chang, W. M.; Yao, Y. F.; Chen, H. T.; Su, C. Y.; Chen, C. Y.; Hsieh, C.; Chen, H. S.; Tu, C. G.; Kiang, Y. W.; Yang, C. C.; Hsu, T. C. *J. Appl. Phys.* **2013**, *113*, 054315.
8. Ra, Y. H.; Navamathavan, R.; Park, J. H.; Lee, C. R. *Nano Lett.* **2013**, *13*, 3506-3516.
9. Liao, C. H.; Tu, C. G.; Chang, W. M.; Su, C. Y.; Shih, P. Y.; Chen, H. T.; Yao, Y. F.; Hsieh, C.; Chen, H. S.; Lin, C. H.; Yu, C. K.; Kiang, Y. W.; Yang, C. C. *Opt. Express* **2014**, *22*, 17303-17319.
10. Wang, X.; Li, S.; Mohajerani, M. S.; Ledig, J.; Wehmann, H. H.; Mandl, M.; Strassburg, M.; Steegmüller, U.; Jahn, U.; Lähnemann, J.; Riechert, H.; Griffiths, I.; Cherns, D.; Waag, A. *Cryst. Growth Des.* **2013**, *13*, 3475.
11. Persson, A. I.; Larsson, M. W.; Stengstrom, S.; Ohlsson, B. J.; Samuelson, L.; Wallenberg, L. R. *Nature Mater.* **2004**, *3*, 677.
12. Moewe, M.; Chuang, L. C.; Dubrovskii, V. G.; Chang-Hasnain, C. *J. Appl. Phys.* **2008**, *104*, 044313.
13. Perea, D. E.; Allen, J. E.; May, S. J.; Wessels, B. W.; Seidman, D. N.; Lauhon, L. J. *Nano Lett.* **2006**, *6*, 181.
14. Rigutti, L.; Jacopin, G.; Largeau, L.; Galopin, E.; Bugallo, A. D.; Julien, F. H.; Harmand, J. C.; Glas, F.; Tchernycheva, M. *Phys. Rev. B* **2011**, *83*, 155320.
15. Zhang, X.; Dubrovskii, V. G.; Sibirev, N. V.; Ren, X. *Cryst. Growth Des.* **2011**, *11*, 5441.
16. Consonni, V.; Knelangen, M.; Geelhaar, L.; Trampert, A.; Riechert, H. *Phys. Rev. B* **2010**, *81*, 085310.
17. Consonni, V.; Hanke, M.; Knelangen, M.; Geelhaar, L.; Trampert, A.; Riechert, H. *Phys. Rev. B* **2011**, *83*, 035310.

18. Consonni, V.; Dubrovskii, V. G.; Trampert, A.; Geelhaar L.; Riechert, H. *Phys. Rev. B* **2012**, *85*, 155313.
19. Yeh, T. W.; Lin, Y. T.; Stewart, L. S.; Dapkus, P. D.; Sarkissian, R.; O'Brien, J. D.; Ahn B.; Nutt, S. R. *Nano Lett.* **2012**, *12*, 3257.
20. Lin, Y. T.; Yeh, T. W.; Nakajima, Y.; Dapkus, P. D. *Advanced Functional Materials* **2014**, *24*, 3162.
21. Jung, B. O.; Bae, S. Y.; Kato, Y.; Imura, M.; Lee, D. S.; Honda, Y.; Amano, H. *CrystEng Comm.* **2014**, *16*, 2273.
22. Tu, C. G.; Liao, C. H.; Yao, Y. F.; Chen, H. S.; Lin, C. H.; Su, C. Y.; Shih, P. Y.; Chen, W. H.; Zhu, E.; Kiang, Y. W.; Yang, C. C. *Opt. Express* **2014**, *22*, A1799-A1809.
23. Tu, C. G.; Su, C. Y.; Liao, C. H.; Hsieh, C.; Yao, Y. F.; Chen, H. T.; Lin, C. H.; Chen, H. S.; Kiang, Y. W.; Yang, C. C. *Superlattices and Microstructures* **2015**, *83*, 329-341.
24. Tu, C. G.; Yao, Y. F.; Liao, C. H.; Su, C. Y.; Hsieh, C.; Weng, C. M.; Lin, C. H.; Chen, H. T.; Kiang, Y. W.; Yang, C. C. *Opt. Express* **2015**, *23*, 21919-21930.
25. Tu, C. G.; Su, C. Y.; Liao, C. H.; Hsieh, C.; Yao, Y. F.; Chen, H. T.; Lin, C. H.; Weng, C. M.; Kiang, Y. W.; Yang, C. C. *Nanotechnology* **2016**, *27*, 025303.
26. Glas, F.; Ramdani, M. R.; Patriarche, G.; Harmand, J. C. *Phys. Rev. B* **2013**, *88*, 195304.
27. Glas, F. *Phys. Rev. B* **2014**, *90*, 125406.
28. Krogstrup, P.; Jørgensen, H. I.; Johnson, E.; Madsen, M. H.; Sørensen, C. B.; Morral, A. F.; Aagesen, M.; Nygård, J.; Glas, F. *J. Phys. D: Appl. Phys.* **2013**, *46*, 31300.
29. Ristic, J.; Calleja, E.; Fernandez-Garrido, S.; Cerutti, L.; Trampert, A.; Jahn, U.; Ploog, K. H. *J. Cryst. Growth* **2008**, *310*, 4035.
30. Hestroffer, K.; Leclere, C.; Cantelli, V.; Bougerol, C.; Renevier, H.; Daudin, B. *Appl. Phys. Lett.* **2012**, *100*, 212107.
31. Kim, Y. H.; Park, D. W.; Lee, S. J. *Appl. Phys. Lett.* **2012**, *100*, 033117.
32. Jacobsson, D.; Panciera, F.; Tersoff, J.; Reuter, M. C.; Lehmann, S.; Hofmann, S.; Dick, K. A.; Ross, F. M. *Nature* **2016**, *531*, 317.
33. Dubrovskii, V. G. *Technical Phys. Lett.* **2016**, *42*, 3.

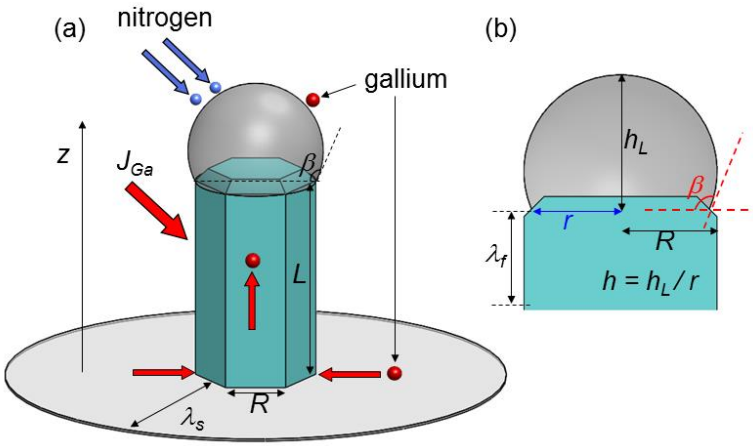

Fig. 1 (a): Schematic demonstration of the formation process of the gallium droplet during gallium supply, including the diffusion of gallium adatoms from the substrate and NR sidewalls to the droplet surface. (b): Demonstration of a sphere-like gallium droplet formed at the NR top with a fixed contact angle β with respect to the NR top face but with an increasing radius r.

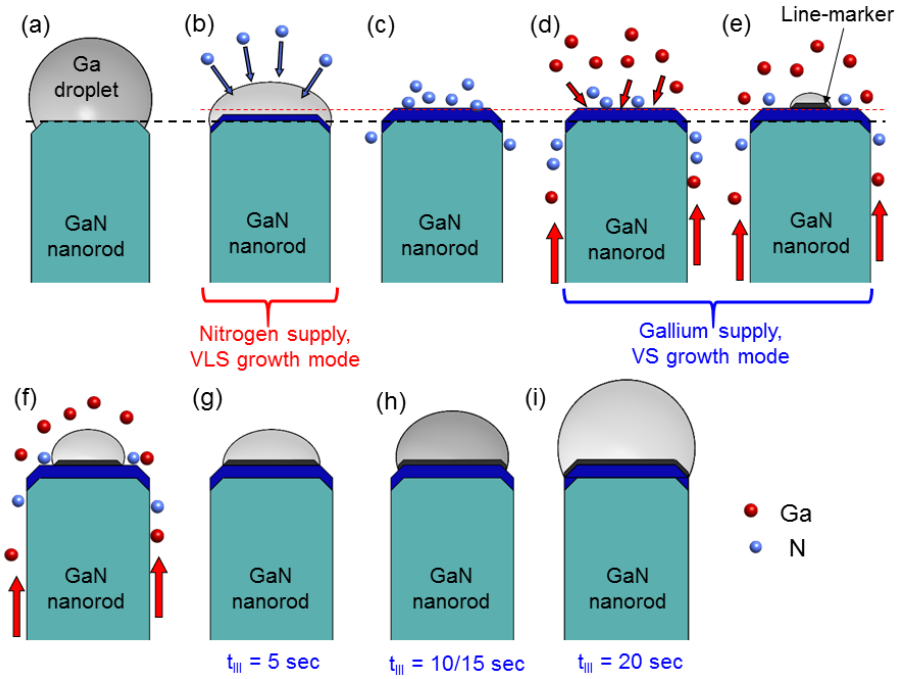

Fig. 2 (a)-(f): Schematic demonstrations of the processes of gallium droplet inflation and deflation, and the formation of the line-marker in a growth cycle. (g)-(i): Schematic demonstrations of the maximum gallium droplet sizes when the gallium supply durations are 5, 10/15, and 20 sec, respectively.

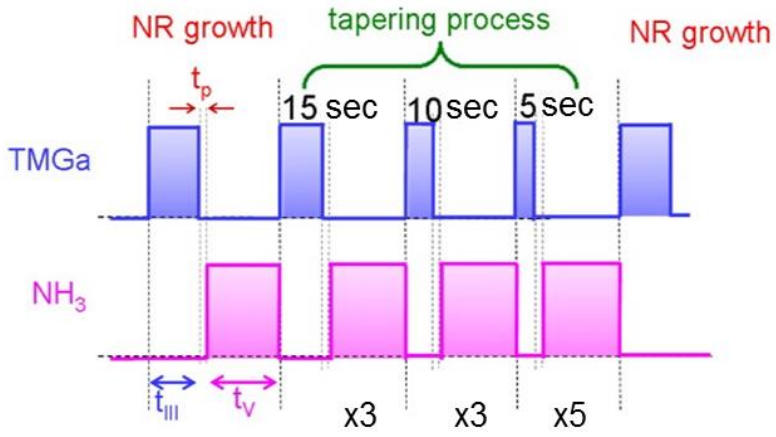

Fig. 3 Schematic demonstrations of the flow patterns of TMGa and HN_3 in the pulsed growth process.

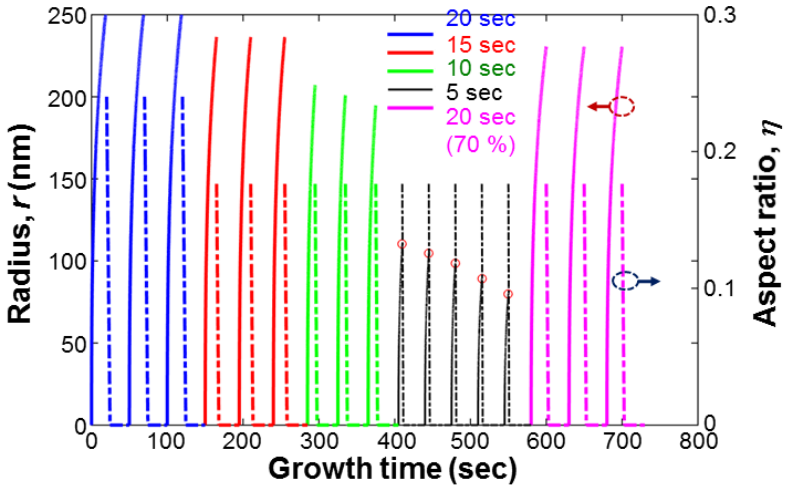

Fig. 4 Numerical results of the gallium droplet radius, r, (with the left ordinate and continuous curve) and aspect ratio, η, (with the right ordinate and dashed curve) as functions of time under the TMGa supply process of 20 sec in duration for 3 cycles, 15 sec for 3 cycles, 10 sec for 3 cycles, 5 sec for 5 cycles, and then 20 sec in duration for 3 cycles with the TMGa flow rate reduced to 70 % while a supply duration of NH_3 is fixed at 30 sec.

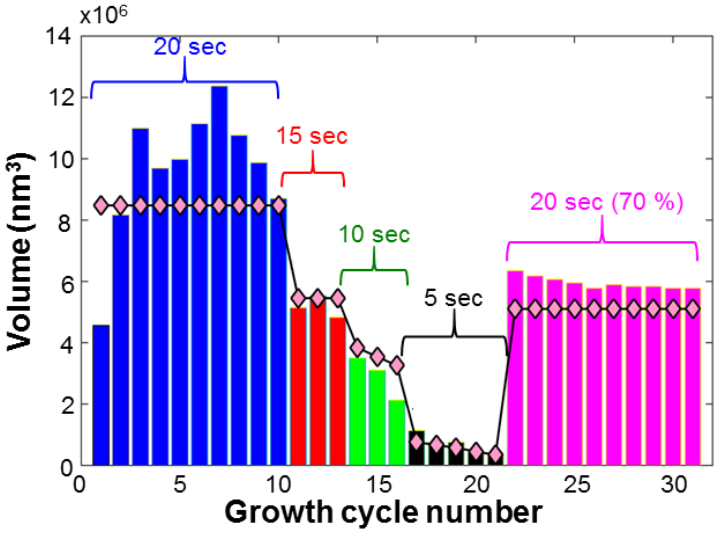

Fig. 5 Numerical results (represented by the diamond symbols) of the GaN volume grown per growth cycle, obtained from equation (10). The vertical bars represent the corresponding data obtained from experiment.

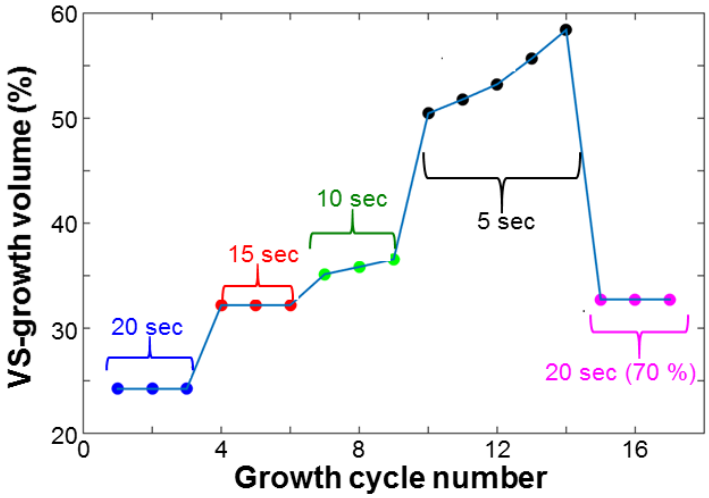

Fig. 6 Evaluated contribution percentages of the VS mode to the total grown GaN volumes in various growth cycles.

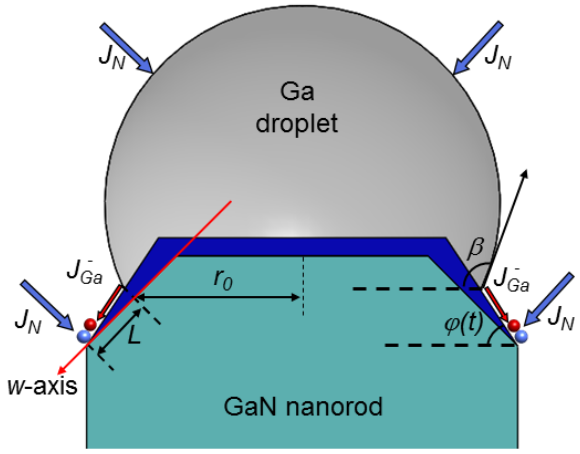

Fig. 7 Schematic demonstration of the model for describing the change of the tilt angle of a slant facet.

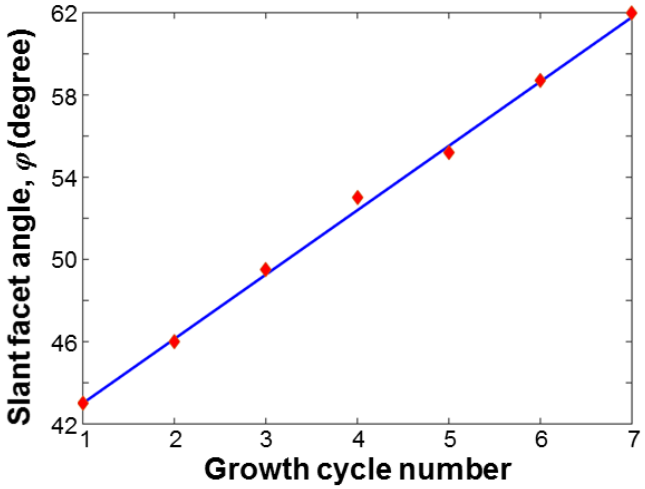

Fig. 8 Evaluated slant facet angle (continuous curve) at the end of a growth cycle, φ, as a function of growth cycle number during a transition process for comparison with the experimental data (red diamonds).

Chapter 4: Anti-reflection behavior of a surface Ga-doped ZnO nanoneedle structure and the controlling factors

1. Introduction

Besides the structure of single- or multiple-layer surface coating [1, 2], surface nanostructures have been widely used for generating the anti-reflection effects in photovoltaic devices. Various Si surface nanostructures on Si solar cells have been fabricated to show strong anti-reflection effects [3-10]. Based on the effective refractive-index model in a surface Si nanostructure, the gradient change of effective refractive index can lead to very low reflection in a Si solar cell. Such a low reflection level is partly attributed to the same surface nanostructure material as the solar cell material. However, with a Si nanostructure on the surface of a Si solar cell, it is usually difficult to fabricate a metal contact on it. Also, normally a transparent conductive oxide (TCO) or passivation layer is needed. Recently, surface metal nanoparticles (NPs) for inducing surface plasmon (SP) resonance have been used for enhancing the sunlight absorption of solar cells [9, 10]. Also, nanostructured TCOs, including ZnO [11-14] and TiO_2 [15], have been widely applied to solar cell for generating the anti-reflection effects. In particular, due to its low growth temperature, low growth selectivity, and high growth speed along its c-axis, ZnO nanowires have been widely used for this purpose [16-19]. For increasing its conductivity, Ga or Al has been doped into ZnO in fabricating nanowire structures. By using such highly transparent and conductive nanowires for generating the anti-reflection effects, the fabrication process of a solar cell can be much simplified. Also, with the electron concentration as high as 10^{21} cm^{-3} in highly Al-doped ZnO or Ga-doped ZnO (GaZnO), its SP resonance behaviors in the spectral range beyond 1000 nm have also been considered for solar cell applications [20, 21]. In this regard, efforts have been made for transferring the energies of SP-resonance induced GaZnO absorption and strong nearby electromagnetic field into photocurrent [22, 23]. Such an effect equivalently increases the anti-reflection function in a solar cell.

For fabricating the Al-doped ZnO or GaZnO nanowires, the vapor-liquid-solid (VLS) growth mode is a commonly used technique [24-26]. In this technique, certain metal NPs are used as growth catalyst. At a high growth temperature, a metal NP is melted for absorbing the constituent atoms of the nanowire to be grown. When the supersaturation condition is reached, the constituent atoms precipitate at the bottom of the melted metal NP for forming the nanowire. To grow GaZnO nanowires of a high Ga-doping concentration for increasing electron concentration and conductivity, normally the growth temperature needs to be lower than 450 ^oC [27-29]. At such a low growth temperature, an Ag NP of a couple tens nm in size cannot be completely melted for serving as growth catalyst. Only the upper portion of such an Ag NP is melted for absorbing the constituent atoms of GaZnO. In this situation, GaZnO precipitates onto the un-melted lower portion of an Ag NP. Therefore, the crystal structure and orientation of a GaZnO nanowire are not directly influenced by the growth template. Because the atoms of the catalytic Ag NP portion mix into the precipitated GaZnO, this Ag NP portion shrinks its size as it is lifted up along the nanowire growth. In this process, the cross section of the nanowire becomes smaller and smaller along the growth until the catalytic Ag is exhausted. Hence, the geometry of a nanoneedle (NN) is formed. Such an NN array can produce an effective anti-reflection function based on the model of effective refractive index. However, the effectiveness of the anti-reflection function depends on the NN geometries and more importantly the NN orientations.

In this chapter, we study the anti-reflection function of a surface nanostructure, including transparent conductive GaZnO NNs, a GaZnO thin film, and buried Ag NPs, on GaN and Si templates through the combination of the effects of gradient effective refractive index, index matching, and the SP resonances in the visible and infrared ranges. The GaZnO thin film at the NN bottom is formed simultaneously with the growth of NNs. The buried Ag NPs on the template surface correspond to the un-melted portions of the originally prepared Ag NPs. We first demonstrate the relations between the anti-reflection behaviors and the morphologies, including the orientation, length, and width of GaZnO NNs grown under different conditions of molecular beam epitaxy (MBE) on c-plane GaN and Si (100) templates. A sample with thinner and mostly vertical NNs with respect to the template surface leads to a stronger anti-reflection effect. Then, we investigate the microscopic mechanism of determining the orientation of a GaZnO NN under a certain growth condition. It is found that a GaZnO NN is always grown along its c-axis [(002) direction], which is always aligned with the local Ag (111) orientation of the un-melted Ag NP portion. The Ag (111) orientation of the un-melted Ag NP portion is influenced by the crystal structure of the used template and the planar density of Ag NPs. The roles of the GaZnO thin film and buried residual Ag NPs in the anti-reflection function are also elucidated. In section 2 of

this chapter, we describe the MBE growth conditions for forming GaZnO NNs. Then, in section 3, we describe the morphologies of the GaZnO NNs in the samples under study. The behaviors of reflection, transmission, and scattering of those GaZnO NN samples are presented in section 4. In section 5, the study results of the microscopic mechanism determining the NN orientation is reported. Discussions about the results are made in section 6. Finally, the conclusions are drawn in section 7.

2. Sample growth conditions and characterization methods

GaZnO NNs are formed based on the VLS growth mode using Ag NPs as growth catalyst on c-plane, Ga-polar GaN and Si (100) templates in an RF-plasma assisted MBE reactor. In a GaN template, a 3-μm GaN layer is deposited on c-plane sapphire substrate with metalorganic chemical vapor deposition. GaZnO is grown under the Zn-rich conditions of 320 ºC in Zn effusion cell temperature, 900 ºC in Ga effusion cell temperature, 1 sccm in O_2 flow rate, 350 W in RF-plasma power, and 350 or 450 ºC in substrate temperature. During the GaZnO growth, besides the formation of NNs, a GaZnO thin film covering the residual Ag NPs is deposited through the vapor-solid growth mode. The Ag NPs are formed by first depositing an Ag layer of 1-1.6 nm in thickness on a template followed by a thermal annealing process at 160-300 ºC for 30 min with ambient nitrogen. The technique of selected area electron diffraction (SAED) based on transmission electron microscopy (TEM) observation is used for identifying the local crystalline orientations of Ag NP, GaZnO NN, GaN, and Si templates to understand their relations.

3. Morphologies of GaZnO nanoneedles and sample designations

Figure 1(a1) shows the tilted scanning electron microscopy (SEM) image of Ag NPs on a GaN template formed by first depositing an Ag layer presumably of ~1.6 nm in thickness. Without any thermal annealing process, Ag NPs of 3.13 x 10^{11} cm^{-2} in planar particle density are formed. Figures 1(a2) and 1(a3) show the SEM images of GaZnO NNs with different magnifications grown at 350 ºC for 80 min on the Ag NP template shown in Fig. 1(a1). This GaZnO NN sample on GaN grown at 350 ºC is referred to as sample GaN/NN-A. Figures 1(b1)-1(b3) show the SEM images similar to Figs. 1(a1)-(a3), respectively, with the GaZnO NNs grown based on a different Ag NP template, which is formed by depositing Ag of ~1.6 nm in thickness and then thermal annealing at 160 ºC for 30 min with ambient nitrogen. As shown in Fig. 1(b1), the planar particle density of the Ag NPs (2.83 x 10^{11} cm^{-2}) becomes lower after thermal annealing. This GaZnO NN sample on GaN template grown at 350 ºC is referred to as sample GaN/NN-B. Figures 1(c1)-1(c3) show the SEM images similar to Figs. 1(b1)-(b3), respectively, with the GaZnO NNs grown on an Ag NP template formed by depositing Ag of ~1.0 nm in thickness and then thermal annealing at 200 ºC for 30 min with ambient nitrogen. With the thinner Ag deposition and the higher annealing temperature, the planar density of the Ag NPs in Fig. 1(c1) becomes even smaller (2.60 x 10^{11} cm^{-2}). This GaZnO NN sample on GaN grown at 350 ºC is referred to as sample GaN/NN-C. Figures 2(a1)-2(a3) show the SEM images similar to Figs. 1(c1)-(c3), respectively, with the GaZnO NNs grown on an Ag NP template formed under the same conditions, but the MBE growth temperature is increased to 450 ºC. This GaZnO NN sample on GaN grown at 450 ºC is referred to as sample GaN/NN-D. Figures 2(b1)-2(b3) show the SEM images similar to Figs. 1(c1)-(c3), respectively, with the GaZnO NNs grown on an Ag NP template, which is formed on a double-side polished Si (100) substrate by depositing Ag of ~1.4 nm in thickness and then thermal annealing at 300 ºC for 30 min with ambient nitrogen. The substrate temperature for growing GaZnO NNs is 350 ºC in this case. This GaZnO NN sample on Si grown at 350 ºC is referred to as sample Si/NN.

By comparing the NN morphologies between Figs. 1(a2)-1(c2) or between Figs. 1(a3)-1(c3), one can see that when the planar density of Ag NPs is reduced, more GaZnO NNs are vertically oriented with respect to the template surface. Many NNs in sample GaN/NN-A tilt almost along the template surface. Although it is difficult to estimate the lengths and base widths of the NNs in those samples, we can still see that generally the NN length increases and the base width decreases with decreasing Ag NP density in samples GaN/NN-A, GaN/NN-B, and GaN/NN-C. By increasing the growth temperature from 350 to 450 ºC, the NNs in sample GaN/NN-D become thinner and longer, when compared with those in sample GaN/NN-C. Although some of the thin NNs bend in sample GaN/NN-D, they are essentially vertically oriented with respect to the template surface. In sample Si/NN, the orientations of grown NNs are randomly distributed although many of them are vertically oriented with respect to the template surface.

During the growth of NNs, a GaZnO thin film of ~150 nm in thickness is simultaneously deposited at the bottom of the NNs. Also, residual (un-melted) Ag NPs lie at the interface between GaZnO and the used template. To observe the effects on the anti-reflection function of the GaZnO thin film and

residual Ag NPs, we prepare a sample of a ~150-nm GaZnO thin film on GaN with a growth temperature at 350 ºC, which is designated as sample GaN/GZO, for comparison. Meanwhile, on Si (100), we prepare a sample with surface Ag NPs covered by a ~150-nm GaZnO thin film. To avoid the formation of NNs, the GaZnO growth temperature is reduced to 250 ºC. This sample of Ag NPs covered by a GaZnO thin film is designated as sample Si/NP/GZO. In addition, another sample of a ~150-nm GaZnO thin film without Ag NP, which is also grown at 250 ºC, is prepared and designated as sample Si/GZO. In the following optical behavior studies, GaN and Si templates are also used and designated as samples GaN and Si, respectively.

4. Optical behaviors of GaZnO nanoneedles

For understanding the behaviors of reflection, transmission, and scattering of those GaZnO NN samples, we measure the line-of-sight transmission (transmittance), the specular reflection (reflectance), the total scattered power integrated over the incidence half-space, and the total scattered power integrated over the transmission half-space. In all measurements, the incident angle is 5 degrees. Figure 3 shows the spectral variations of transmittance of those NN samples grown on GaN. For comparison in this figure, we also plot the transmittance spectra of samples GaN and GaN/GZO. Here, the slight oscillation in the transmittance curve for the GaN template is caused by the Fabry-Perot effect. After depositing the GaZnO thin film on the GaN template, the transmittance is slightly increased, particularly on the short-wavelength side. Among the NN samples, sample GaN/NN-A of highly tilted NNs does not show enhanced transmission, when compared with that of the GaN template. The transmittance is enhanced in the spectral range between 700 and 1400 nm in sample GaN/NN-B. In samples GaN/NN-C and GaN/NN-D, the spectral windows of enhanced transmittance are even larger and the maximum transmittance levels are further increased. In other words, the transmittance is generally higher when light passes through more vertically oriented GaZnO NNs. In sample GaN/NN-D, the transmittance can reach 85 % in the spectral range between 1000 and 1400 nm. The decreasing transmittance beyond 1200 nm in samples GaN/NN-A, GaN/NN-B, and GaN/NN-C is due to the SP resonance induced absorption of GaZnO NNs and thin film because of the relatively lower growth temperature (350 ºC) and hence higher electron concentration. Because the growth temperature is higher (450 ºC) and hence the electron concentration is lower in sample GaN/NN-D, the SP resonance in the concerned spectral range is weaker such that the transmittance is higher beyond 1200 nm. Figure 4 shows the spectral variations of reflectance corresponding to the transmittance data in Fig. 3. Here, we can see that by depositing a GaZnO thin film or forming GaZnO NNs on GaN, the reflectance can be more or less reduced. Among the NN samples, the reflectance is generally lower when light is reflected from more vertically oriented GaZnO NNs.

Figure 5 shows the power percentages integrated over the transmission half-space corresponding to the transmittance data shown in Fig. 3. Here, one can see that the spectral variations among different samples are similar to the corresponding curves in Fig. 3. However, by including the scattered light power in the directions deviated from the line-of-sight, the collected light power is enhanced in each sample. Figure 6 shows the power percentages integrated over the incidence half-space corresponding to the data shown in Fig. 5. Again, the spectral variations among different samples are similar to the corresponding curves in Fig. 4. However, by including the scattered light power in the directions deviated from the specular angle, the collected light power is enhanced in each sample. With the power percentages collected in the transmission and incidence half-spaces in Figs. 5 and 6, respectively, we can evaluate the absorbance spectra of those samples to give the results in Fig. 7. Here, the increased absorbance below 600 nm in the NN samples are due to the SP-resonance induced absorption of the residual Ag NPs. The increased absorbance beyond 1400 nm in those samples is caused by the SP-resonance induced absorption of GaZnO.

Figure 8 shows the spectral variations of transmittance (T) and reflectance (R) of samples Si/NN, Si/NP/GZO, Si/GZO, and Si. Because of the strong Si absorption below 900 nm, the transmittance of either sample is almost zero below this wavelength. Due to the absorption caused by the SP resonance of GaZnO, the transmittance of sample Si/NN is lower than that of the Si template beyond 1000 nm. The even stronger SP-resonance induced absorptions in samples Si/NP/GZO and Si/GZO result in the even lower transmittance levels beyond 1100 nm. The stronger SP resonance in either sample Si/NP/GZO or sample Si/GZO is attributed to the lower GaZnO growth temperature. At the lower growth temperature of 250 ºC, the electron concentration of GaZnO becomes higher and hence the SP resonance becomes stronger, when compared with the cases of 350 and 450 ºC in growth temperature [27, 28]. With the anti-reflection effect of GaZnO NNs in sample Si/NN, the reflectance of this sample is significantly reduced, when compared with sample Si. The reflectance levels of samples Si/NP/GZO

and Si/GZO lie between those of samples Si/NN and Si below 1300 nm. They increase fast with wavelength beyond 1000 nm. The reflectance level of sample Si/NP/GZO is lower than that of sample Si/GZO, indicating that the Ag NPs contribute significantly to the anti-reflection function. In Fig. 9, we show the power percentages collected over the incidence (R) and transmission (T) half-spaces corresponding to the reflectance and transmittance results in Fig. 8. The spectral variations of the power percentages collected over the incidence and transmission half-spaces are similar to those of reflectance and transmittance, respectively, shown in Fig. 8. However, the power levels are all increased. In particular, beyond 1000 nm, the power percentage collected over the transmission half-space in sample Si/NN is significantly higher than the transmittance level, indicating that the strong scattering of GaZnO NNs deviates light propagation from the line-of-sight when light passes through the sample. Figure 10 shows the spectral variations of sample absorbance obtained from the data in Fig. 9. Below 1000 nm, due to the reduced returned power percentage, the Si absorption is significantly increased in sample Si/NN. In this spectral range, the Si absorbance levels in samples Si/NP/GZO and Si/GZO are also enhanced due to their anti-reflection functions. Beyond 1100 nm, the high absorbance levels of samples Si/NP/GZO and Si/GZO are caused by the SP-resonance induced absorption of the GaZnO thin films.

5. Microscopic mechanism determining GaZnO nanoneedle orientation

Figure 11(a) shows the TEM image of an NP-like body on a GaN template in a sample similar to sample GaN/NN-C, but the MBE growth duration is only 10 min. Here, we plot the horizontal (pink) dotted line to show the top boundary of GaN. Figures 11(b1), 11(b2), and 11(d1)-11(d4) [11(c1)-11(c4)] show the SAED patterns of the circled regions in Fig. 11(a) together with the dashed-line indicators of the Ag (111) [ZnO (002)] orientation. Figure 11(e) shows the similar result of a GaN region with the GaN (002) orientation. Here, we can see that the NP-like body consists of three layers with the major contents of Ag, ZnO, and Ag. In all layers, the Ag (111) and ZnO (002) orientations are the same as that of GaN (002) in the template. The crystal structure in this NP-like body shows an early-stage condition of the VLS growth for forming a GaZnO NN. The top layer corresponds to the melted Ag portion for serving as growth catalyst and absorbing Ga and Zn atoms. Under the supersaturation condition, Ga and Zn atoms precipitate at the bottom of the melted Ag portion to interact with oxygen atoms coming from the triple-phase line (the boundary between melted and un-melted Ag and vapor) for forming GaZnO on the un-melted, lower Ag portion [30]. Therefore, a layer of GaZnO is sandwiched by the top and bottom Ag layers. For further understanding the composition distribution of this NP-like body, we perform line-scan energy-dispersive X-ray spectroscopy (EDX) measurement along the three vertical lines, 1-3, in Fig. 12(a), which is duplicated from Fig. 11(a). The EDX signal profiles of Ga, Zn, and Ag along lines 1-3 are shown in Figs. 12(b)-12(d), respectively. Along all lines, Ga content increases essentially monotonically along depth. Along each line-scan, there is a Zn distribution peak roughly in the 15-30 nm range in depth. Also, we can see two Ag distribution portions roughly in the ranges of 0-18 and 28-35 nm in each line-scan. The Ag content is lower in the range of 0-18 nm along line-scan 3 because of the thin NP structure around this corner. In each line-scan, small amounts of Ga and Zn atoms exit in the range of 1-15 nm. From these EDX line-scan results, we can conclude that GaZnO is formed in the range around 15-30 nm, as indicated in Fig. 12(a). In the layer above the GaZnO layer, residual Ga and Zn atoms mix with Ag atoms, confirming that this is the melted portion of the Ag NP for absorbing Ga and Zn to form GaZnO below. The range of 35-40 nm in depth of each line-scan corresponds to the GaN template.

Figure 13(a) shows the cross-sectional TEM image of the GaZnO NNs on GaN in a sample similar to sample GaN/NN-C, but the growth duration is only 10 min. Here, one can see essentially vertical NNs with an Ag NP at the top of each NN. The bottom Ag clusters come from the mixture of the un-melted portions of Ag NPs. Figure 13(b) shows the TEM image of a single NN, which is essentially vertical to the template surface. We magnify the circled top and bottom portions of the NN to give the TEM images in Figs. 13(c) and 13(d), respectively. The top Ag NP has a single-crystal structure with the SAED pattern and Ag (111) orientation shown in Fig. 13(c1). Near its top, the grown GaZnO NN shows a quasi-single-crystal structure with its SAED pattern and ZnO (002) orientation shown in Fig. 13(c2). In Fig. 13(d), one can see that an Ag layer of 15-20 nm in thickness separates the GaZnO NN and GaN template. Here, we demonstrate the SAED patterns and the key crystalline orientations of the GaZnO NN, Ag layer, and GaN template in Figs. 13(d1)-13(d3), respectively. One can see that the orientations of Ag (111) in the top Ag NP, ZnO (002) in the GaZnO NN near its top, ZnO (002) in the GaZnO NN near its bottom, Ag (111) in the bottom Ag layer, and GaN (002) in the template are all the same and vertically aligned.

Figure 14(a) shows the TEM image of a few GaZnO NNs on GaN in a sample similar to sample

GaN/NN-A, but the growth duration is only 10 min. Here, we can see two NNs of different orientations grown from a cluster of Ag NP. Figure 14(b) shows the magnified TEM image of the circled bottom portion of the two NNs. As shown in the SAED patterns of Figs. 14(c1)-14(c3), the ZnO (002) orientation of the vertical NN on the left and the Ag (111) orientations in the Ag portion close to the bottom of this NN and in the bottom Ag portion close to GaN all align with GaN (002) orientation in the template [see Fig. 14(e)]. On the other hand, as shown in Figs. 14(d1) and 14(d2), the ZnO (002) orientation of the tilted NN on the right and the Ag (111) orientation in the Ag portion close to the bottom of this NN are the same and are different from those of other image portions. Such results indicate that the growth direction of a GaZnO NN follows the local crystalline orientation of an Ag NP by aligning the ZnO (002) direction with the Ag (111) orientation of the growth base. Because of the high growth speed of ZnO along its (002) direction, the NN growth follows the direction of Ag (111) of the un-melted residual Ag portion used as the base for NN growth. Figure 15(a) shows the TEM image of the GaZnO NNs on Si (100) in sample Si/NN. Here, we focus our analysis on the tilted NN circled by the pink square, particularly its bottom portion. Figure 15(b) shows the magnified TEM image around the bottom of this NN. Here, the dark portion near the center of this image corresponds to an Ag NP. Figures 15(c)-15(e) show the SAED patterns together with the individual orientation indications of Zn (002), Ag (111), and Si (400), respectively, in the circled regions. The Si (400) orientation is the same as that of Si (100), confirming the crystal structure of the used Si template. Although the Ag NP directly contacts the Si template, the Ag (111) orientation deviates from the Si (100) direction. Influenced by this Ag (111) orientation, the growth of the GaZnO NN tilts along a direction close to the Ag (111) orientation.

In the hexagonal structure of ZnO or GaN, its (002) plane has seven closely packed Zn or Ga atoms (O or N atoms). The nearest atomic distance in such a hexagonal, closely packed ZnO (GaN) structure, i.e., the *a* constant, is 0.325 nm (0.318 nm). Ag crystal has a face-centered cubic structure. On its (111) plane, it also shows a hexagonal, closely packed structure of seven Ag atoms with the nearest atomic distance at 0.288 nm. Although the nearest atomic distances of Ag (111) and ZnO (002) [or GaN (002)] are slightly different, their similar lattice structures of hexagonal, closely packed arrangements can lead to the minimum energy by aligning the Ag (111) and ZnO (002) [or GaN (002)] orientations. Therefore, on a c-plane GaN template, Ag NPs with Ag (111) orientation aligned with GaN (002) are formed when the template temperature is high enough for Ag crystal reorganization. Similarly, the ZnO (002) orientation of the grown GaZnO NN is the same as the Ag (111) direction of the Ag portion, onto which GaZnO is formed. On a Si (100) template, because there is no crystalline matching condition between Si and Ag, the Ag NPs have poly-crystalline structures of random orientations with respect to Si (100) direction. Following the local Ag (111) orientations, the grown GaZnO NNs become randomly oriented.

6. Discussions

The anti-reflection effect of a surface nanowire structure is usually interpreted with the effective refractive-index model, i.e., the gradual change of the laterally average dielectric constant along the nanowire length. Based on this model, a sample of vertically oriented GaZnO NNs can result in a gradual decrease of effective refractive-index along depth. Therefore, the reflectance (transmittance) and power percentage collected in the incidence (transmission) half-space are the lowest (highest) in sample GaN/NN-C, followed by sample GaN/NN-B, and then sample GaN/NN-A, among the three samples grown at 350 ^{o}C on GaN. With the growth temperature increased to 450 ^{o}C, the thinner and longer NNs of essentially vertical orientations lead to even lower (higher) reflectance (transmittance) and power percentage collected in the incidence (transmission) half-space in sample GaN/NN-D. When GaZnO NNs are grown on a Si (100) template, the random distribution of NN orientation reduces the anti-reflection effect. However, the overall anti-reflection effect is also related to the refractive-index difference between the template and NN materials. In a GaZnO NN sample, a GaZnO thin film is simultaneously deposited at the bottom of NNs. In other words, light penetrating into the NNs can be reflected at the interface between the GaZnO thin film (refractive-index at ~1.8) and the template (refractive-index at ~2.4 in GaN and >3 in Si). Therefore, the power percentage collected over the incidence half-space in sample Si/NN (either below or beyond 1000 nm) is higher, when compared with samples GaN/NN-C and GaN/NN-D, because of the larger refractive-index difference between GaZnO and Si.

As shown in Figs. 13 and 14, a less dense Ag NP distribution with a larger NP separation on GaN can lead to the growth of vertically oriented GaZnO NNs for a stronger anti-reflection effect. The vertical orientation of an NN on c-plane GaN is due to the crystalline matching between ZnO (002), Ag (111), and GaN (002). On a Si template, because of the lack of such a crystalline matching condition

between Si and Ag, the orientation of an NN is controlled by the local Ag crystal orientation, which is randomly distributed. Therefore, the NNs on Si are randomly oriented. One possible solution for making the GaZnO NNs vertical as possible is to first deposit a buffer layer, which has the crystal structure similar to GaZnO with its c-axis in the vertical direction, on Si. On such a buffer layer, the Ag (111) orientation of the formed Ag NPs can be aligned in the vertical direction such that the GaZnO NNs grown on them can be vertically aligned. For Si photovoltaic applications, this buffer layer needs to be transparent and conductive. A GaZnO thin film can be a good choice for this buffer layer. However, it needs efforts for finding the optimized growth condition to form such a favored buffer layer on Si.

As shown in Figs. 4, 6, 8, and 9, a GaZnO thin film on the template in either sample GaN/GZO or sample Si/GZO can reduce the reflectance and the power percentage collected over the incidence half-space based on the effect of index matching except in the long-wavelength range, in which the SP resonance of GaZnO changes the reflection behavior. Under the SP resonance condition of GaZnO, both reflection and absorption increase. The absorption of GaZnO can contribute to the photocurrent of a solar cell through the process of hot carrier generation [21, 22]. The strong electromagnetic field produced near a GaZnO nanostructure at SP resonance can enhance the solar cell absorption beyond 1000 nm [20]. This is particularly useful for a Si solar cell because the Si absorption coefficient decreases significantly beyond 1000 nm. The buried Ag NPs can also induce SP resonance in the visible range. It has been shown that such an SP resonance behavior can scatter incident sunlight into the forward direction such that the solar cell absorption can be enhanced [23]. The SP resonance and non-coherent scattering of Ag NPs lead to the enhanced anti-reflection function of sample Si/NP/GZO, when compared with sample Si/GZO, as shown in Figs. 8 and 9. The residual Ag NPs in sample Si/NN and the NN samples on GaN should also make the similar contributions to the anti-reflection function even though their Ag NP densities can be lower, when compared with that in sample Si/NP/GZO.

7. Summary

In summary, we have compared the morphology, particularly the orientation, and the anti-reflection behaviors of GaZnO NNs formed under different MBE growth conditions and with different catalytic Ag NP distributions on c-plane GaN and Si (100) templates based on the VLS growth method. For understanding the microscopic mechanism of controlling the GaZnO NN orientation, we analyzed the relations of crystal structure between the GaZnO NN, catalytic Ag NP, and growth template. It was found that the c-axis direction of a GaZnO NN was controlled by the local Ag (111) orientation of the un-melted portion of an Ag NP, which was influenced by the crystal structure of the growth template. On c-plane GaN, by using small and separate Ag NPs as catalyst, the alignment of GaN (002), Ag (111), and ZnO (002) could lead to the growth of mostly vertical NNs for producing a strong anti-reflection effect. On Si (100), no crystal matching condition could be used such that the grown NNs were randomly oriented, leading to a weaker anti-reflection effect. Besides the effects of NNs, the contributions of the simultaneously grown GaZnO thin film and buried Ag NPs through SP resonances to the anti-reflection function were also illustrated.

References

1. Y. F. Makableh, R. Vasan, J. C. Sarker, A. I. Nusir, S. Seal, and M. O. Manasreh, "Enhancement of GaAs solar cell performance by using a ZnO sol-gel anti-reflection coating," Sol. Energy Mater. Sol. Cells **123**, 178-182 (2014).
2. D. Li, D. Wan, X. Zhu, Y. Wang, Z. Han, S. Han, Y. Shan, and F. Huang, "Broadband antireflection TiO_2-SiO_2 stack coatings with refractive-index-grade structure and their applications to Cu(In,Ga)Se_2 solar cells," Sol. Energy Mater. Sol. Cells **130**, 505-512 (2014).
3. S. K. Srivastava, D. Kumar, P. K. Singh, M. Kar, V. Kumar, and M. Husain, "Excellent antireflection properties of vertical silicon nanowire arrays," Sol. Energy Mater. Sol. Cells **94**, 1506-1511 (2010).
4. J. Zhu, Z. Yu, G. F. Burkhard, C. M. Hsu, S. T. Connor, Y. Xu, Q. Wang, M. McGehee, S. Fan, and Y. Cui, "Optical absorption enhancement in amorphous silicon nanowire and nanocone arrays," Nano Lett. **9**, 279-282 (2009).
5. P. Pignalosa, H. Lee, L. Qiao, M. Tseng, and Y. Yi, "Graded index and randomly oriented core-shell silicon nanowires for broadband and wide angle antireflection," AIP Advances **1**, 032124 (2011).
6. A. Rahman, A. Ashraf, H. Xin, X. Tong, P. Sutter, M. D. Eisaman, and C. T. Black, "Sub-50-nm self-assembled nanotextures for enhanced broadband antireflection in silicon solar cells," Nat. Commun. **6**, 5963 (2015).

7. F. Hui, L. Xudong, S. Shuang, X. Ying, and Z. Jing, "Fabrication of slantingly-aligned silicon nanowire arrays for solar cell applications," Nanotechnology **19**, 255703 (2008).
8. L. Zeng, X. Yu, Y. Han, and D. Yang, "Performance of silicon nanowire solar cells with phosphorus-diffused emitters," J. Nanomaterials **2012**, 156986 (2012).
9. S. H. Baek, S. B. Kim, J. K. Shin, and J. Hyun Kim, "Preparation of hybrid silicon wire and planar solar cells having ZnO antireflection coating by all-solution processes," Sol. Energy Mater. Sol. Cells **96**, 251-256 (2012).
10. X. Liang, L. Shu, H. Lin, M. Fang, H. Zhang, G. Dong, S. Yip, F. Xiu, and J. C. Ho, "Inverted silicon nanopencil array solar cells with enhanced contact structures," Sci. Rep. **6**, 34139 (2016).
11. T. H. Wu, R. W. Chuang, C. Y. Huang, C. Y. Cheng, C. Y. Huang, Y. C. Lin, and Y. K. Su, "ZnO nanoneedles/ZnO:Al film stack as an anti-reflection layer for high efficiency triple junction solar cell," Electrochem. Solid-State Lett. **15**, H208-H210 (2012).
12. R. J. Chung, Z. C. Lin, C. A. Lin, and K. Y. Lai, "Study of an antireflection surface constructed of controlled ZnO nanostructures," Thin Solid Films **570**, 504-509 (2014).
13. R. Dalvand, S. Mahmud, J. Rouhi, and C. H. R. Ooi, "Well-aligned ZnO nanoneedle arrays grown on polycarbonate substrates via electric field-assisted chemical method," Mater. Lett. **146**, 65-68 (2015).
14. J. Y. Chen and K. W. Sun, "Growth of vertically aligned ZnO nanorod arrays as antireflection layer on silicon solar cells," Sol. Energy Mater. Sol. Cells **94**, 930-934 (2010).
15. J. W. Leem, J. Su Yu, D. H. Jun, J. Heo, and W. K. Park, "Efficiency improvement of III-V GaAs solar cells using biomimetic TiO_2 subwavelength structures with wide-angle and broadband antireflection properties," Sol. Energy Mater. Sol. Cells **127**, 43-49 (2014).
16. Y. F. Yao, C. H. Shen, W. F. Chen, P. Y. Shih, W. H. Chou, C. Y. Su, H. S. Chen, C. H. Liao, W. M. Chang, Y. W. Kiang, and C. C. Yang, "Void structures in regularly patterned ZnO nanorods grown with the hydrothermal method," J. Nanomaterials **2014**, 756401 (2014).
17. M. Sakurai, Y. G. Wang, T. Uemura, and M. Aono, "Electrical properties of individual ZnO nanowires," Nanotechnology **20**, 155203 (2009).
18. Z. Zheng, Z. S. Lim, Y. Peng, L. You, L. Chen, and J. Wang, "General route to ZnO nanorod arrays on conducting substrates via galvanic-cell-based approach," Sci. Rep. **3**, 2434 (2013).
19. S. Xu and Z. L. Wang, "One-dimensional ZnO nanostructures: Solution growth and functional properties," Nano Research **4**, 1013-1098 (2011).
20. G. V. Naik, V. M. Shalaev, and A. Boltasseva, "Alternative plasmonic materials: beyond gold and silver," Adv. Mater. **25**, 3264-3294 (2013).
21. C. Clavero, "Plasmon-induced hot-electron generation at nanoparticle/metal-oxide interfaces for photovoltaic and photocatalytic devices," Nat. Photon. **8**, 95-103 (2014).
22. F. Wang and N. A. Melosh, "Plasmonic energy collection through hot carrier extraction," Nano Lett. **11**, 5426-5430 (2011).
23. F. J. Tsai, J. Y. Wang, J. J. Huang, Y. W. Kiang, and C. C. Yang, "Absorption enhancement of an amorphous Si solar cell through surface plasmon-induced scattering with metal nanoparticles," Opt. Express **18**, A207-A220 (2010).
24. V. Bhosle, A. Tiwari, and J. Narayan, "Electrical properties of transparent and conducting Ga doped ZnO," J. Appl. Phys. **100**, 033713 (2006).
25. H. M. Chiu, H. J. Tsai, W. K. Hsu, and J. M. Wu, "Experimental and computational insights in the growth of gallium-doped zinc oxide nanostructures with superior field emission properties," CrystEngComm **15**, 5764-5775 (2013).
26. C. H. Hsu and D. H. Chen, "Synthesis and conductivity enhancement of Al-doped ZnO nanorod array thin films," Nanotechnology **21**, 285603 (2010).
27. Y. F. Yao, C. G. Tu, T. W. Chang, H. T. Chen, C. M. Weng, C. Y. Su, C. Hsieh, C. H. Liao, Y. W. Kiang, and C. C. Yang, "Growth of highly conductive Ga-doped ZnO nanoneedles," ACS Applied Materials & Interfaces **7**, 10525-10533 (2015).
28. Y. F. Yao, C. H. Lin, C. Hsieh, C. Y. Su, E. Zhu, S. Yang, C. M. Weng, M. Y. Su, M. C. Tsai, S. S. Wu, S. H. Chen, C. G. Tu, H. T. Chen, Y. W. Kiang, and C. C. Yang, "Multi-mechanism efficiency enhancement in growing Ga-doped ZnO as the transparent conductor on a light-emitting diode," Opt. Express **23**, 32274-32288 (2015).
29. C. H. Lin, Y. F. Yao, C. Y. Su, C. Hsieh, C. G. Tu, S. Yang, S. S. Wu, Y. W. Kiang, and C. C. Yang, "Thermal annealing effects on the performance of a Ga-doped ZnO transparent-conductor layer in a light-emitting diode," IEEE Trans. Electron Devices **62**, 3742-3749 (2015).
30. H. Simon, T. Krekeler, G. Schaan, and W. Mader, "Metal-seeded growth mechanism of ZnO

nanowires," Crystal Growth & Design **13**, 572-580 (2013).

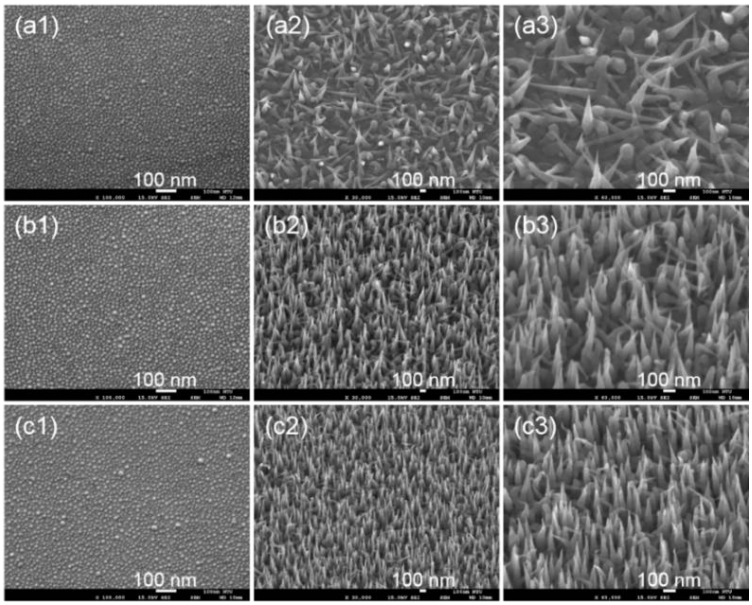

Fig. 1. (a1): Tilted SEM image of Ag NPs on a GaN template for growing sample GaN/NN-A. (a2) and (a3): SEM images of GaZnO NNs of sample GaN/NN-A with different magnifications. (b1)-(b3) [(c1)-(c3)]: SEM images similar to parts (a1)-(a3), respectively, for sample GaN/NN-B (GaN/NN-C).

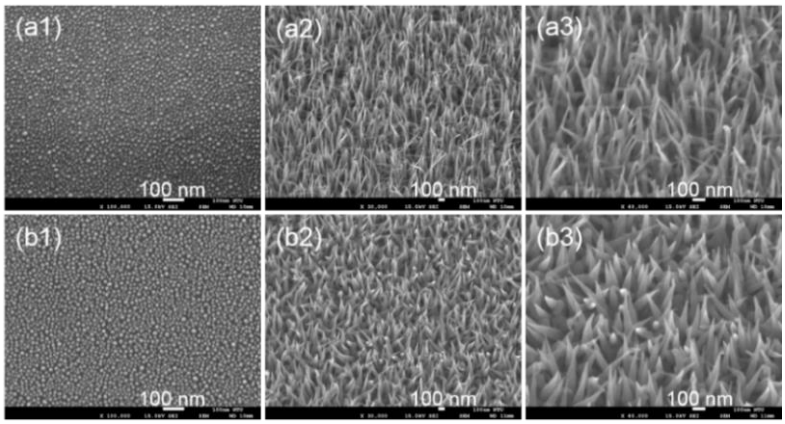

Fig. 2. (a1)-(a3) [(b1)-(b3)]: SEM images similar to Figs. 1(c1)-(c3), respectively, for sample GaN/NN-D (Si/NN).

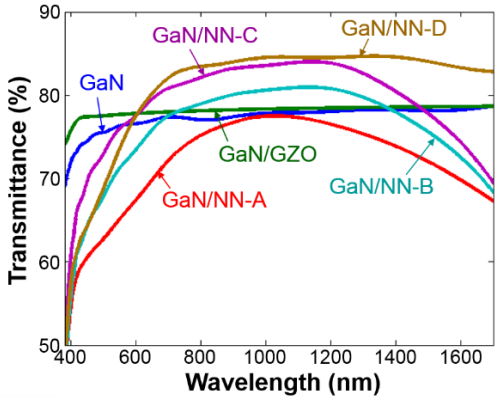

Fig. 3. Spectral variations of transmittance of samples GaN, GaN/GZO, GaN/NN-A, GaN/NN-B, GaN/NN-C, and GaN/NN-D.

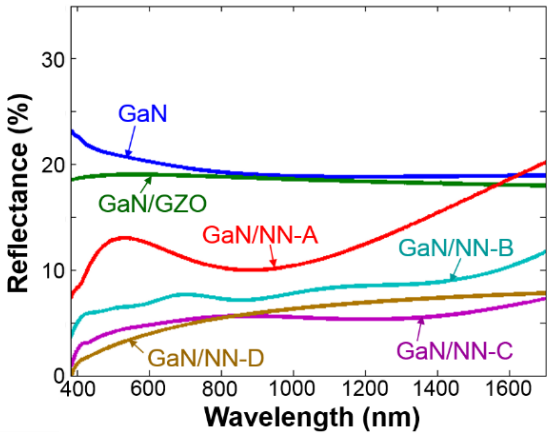

Fig. 4. Spectral variations of reflectance of samples GaN, GaN/GZO, GaN/NN-A, GaN/NN-B, GaN/NN-C, and GaN/NN-D.

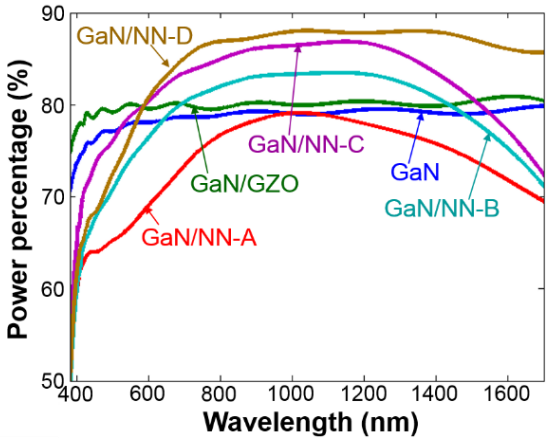

Fig. 5. Spectral variations of the power percentage collected over the transmission half-space of samples GaN, GaN/GZO, GaN/NN-A, GaN/NN-B, GaN/NN-C, and GaN/NN-D.

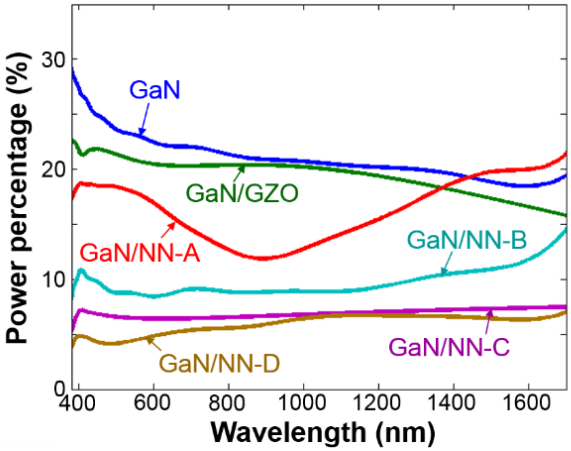

Fig. 6. Spectral variations of the power percentage collected over the incidence half-space of samples GaN, GaN/GZO, GaN/NN-A, GaN/NN-B, GaN/NN-C, and GaN/NN-D.

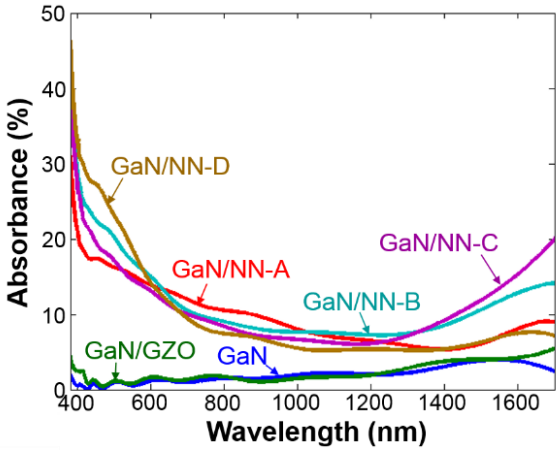

Fig. 7. Spectral variations of absorbance of samples GaN, GaN/GZO, GaN/NN-A, GaN/NN-B, GaN/NN-C, and GaN/NN-D.

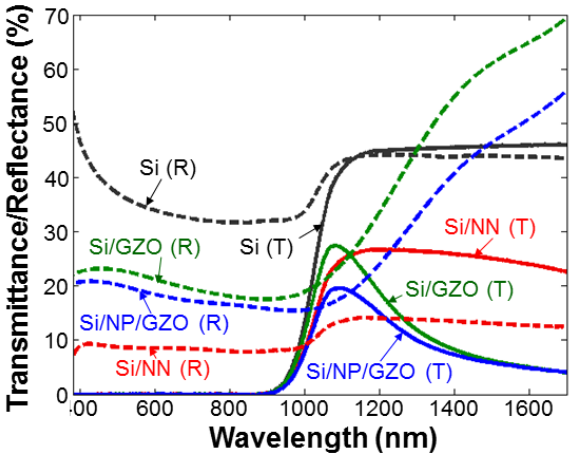

Fig. 8. Spectral variations of transmittance (T) and reflectance (R) of samples Si, Si/NP/GZO, Si/GZO, and Si/NN.

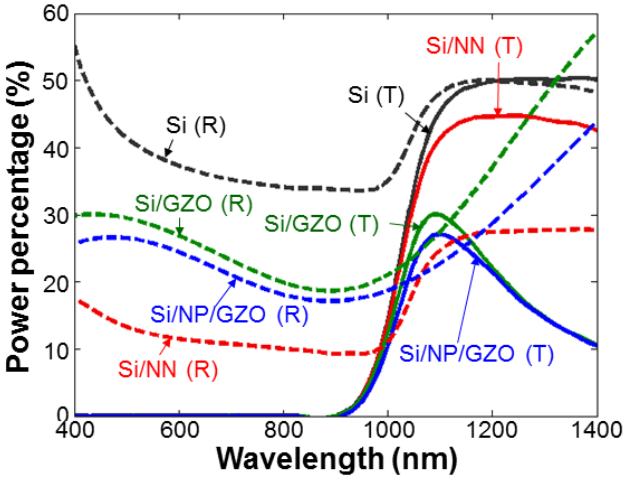

Fig. 9. Spectral variations of the power percentages collected over the incidence (R) and transmission (T) half-spaces of samples Si, Si/NP/GZO, Si/GZO, and Si/NN.

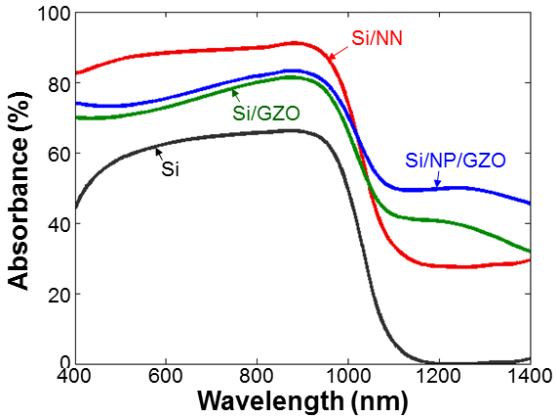

Fig. 10. Spectral variations of absorbance of samples Si, Si/NP/GZO, Si/GZO, and Si/NN.

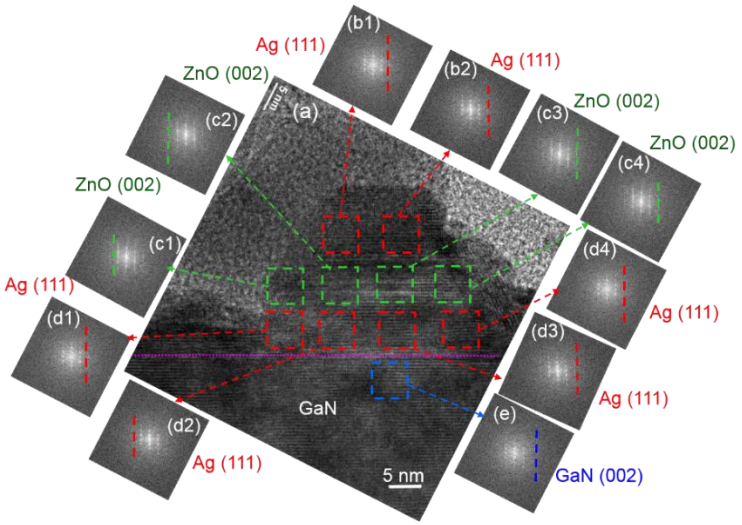

Fig. 11. (a): Cross-sectional TEM image of an NP body on a GaN template. The pink dotted line plots the boundary between Ag and GaN. (b1), (b2), (c1)-(c4), (d1)-(d4), and (e): SAED patterns together with the dashed-line indicators of the Ag (111), ZnO (002), and GaN (002) orientations in the circled regions of part (a).

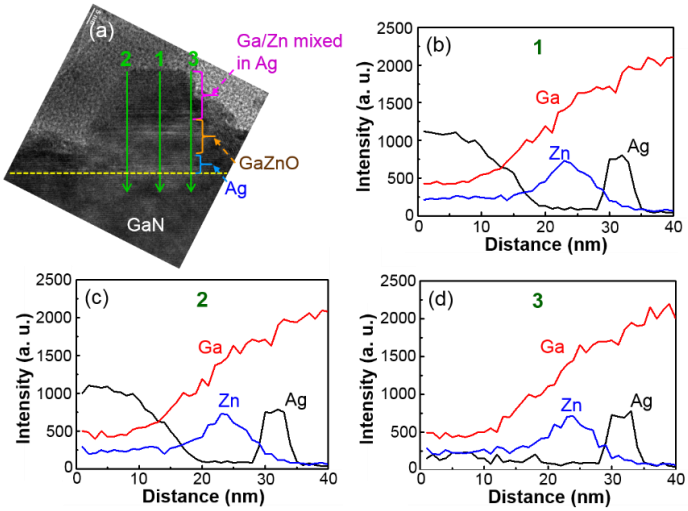

Fig. 12. (a): TEM image duplicated from Fig. 11(a) with three vertical green arrows drawn for EDX line scans. (b)-(d): Line-scan EDX signal profiles of Ga, Zn, and Ag along arrows 1-3, respectively, shown in part (a).

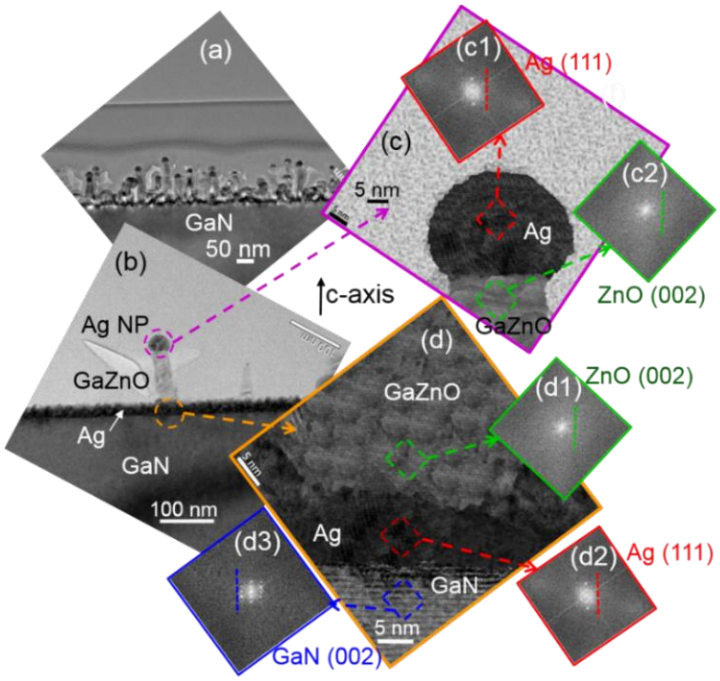

Fig. 13. (a): Cross-sectional TEM image of the GaZnO NNs on GaN in a sample similar to sample GaN/NN-C, but the growth duration is only 10 min. (b): TEM image of a single NN. (c) and (d): Magnified TEM images in the circled top and bottom portions, respectively, of the NN in part (b). (c1), (c2), and (d1)-(d3): SAED patterns of the designated areas and the corresponding Ag (111), ZnO (002), and GaN (002) orientations.

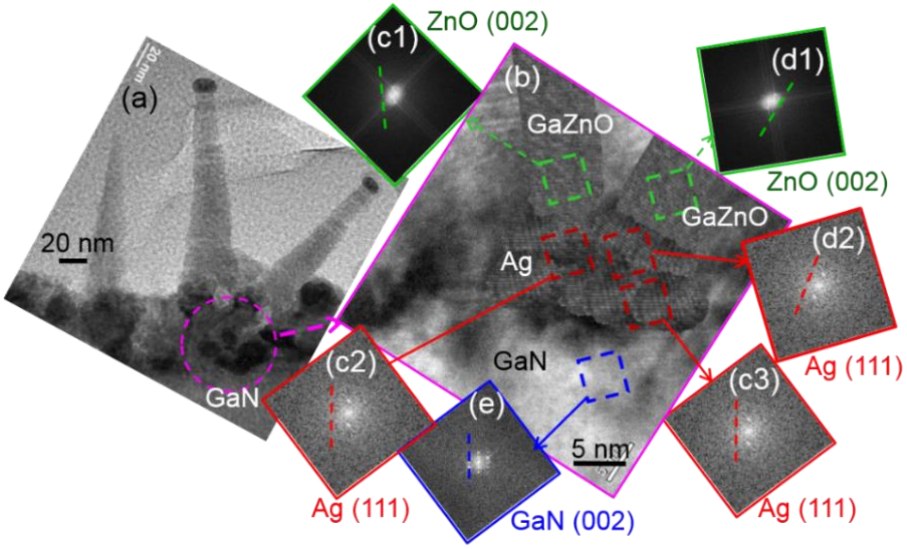

Fig. 14. (a): Cross-sectional TEM image of the GaZnO NNs on GaN in a sample similar to sample GaN/NN-A, but the growth duration is only 10 min. (b): Magnified TEM image of the circled bottom portion of the two NNs. (c1)-(c3), (d1), (d2), and (e): SAED patterns of the designated areas and the corresponding Ag (111), ZnO (002), and GaN (002) orientations.

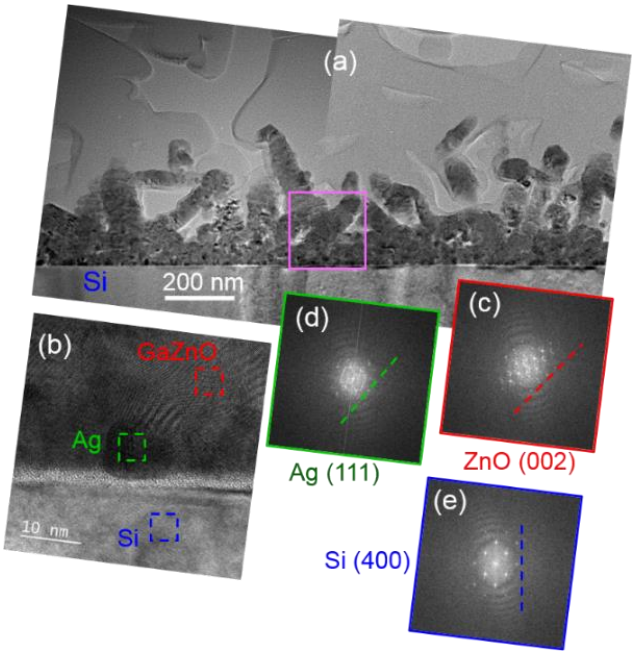

Fig. 15. (a): Cross-sectional TEM image of the GaZnO NNs on Si in sample Si/NN. (b): Magnified TEM image around the bottom of the circled NN in part (a). (c)-(e): SAED patterns together with the individual orientation indications of ZnO (002), Ag (111), and Si (400), respectively, in the circled regions.

List of Publications Acknowledging AOARD Support: (October 2014 - November 2017)

SCI journal papers:

1. Yu-Feng Yao, Shaobo Yang, Huang-Hui Lin, Keng-Ping Chou, Chi-Ming Weng, Jia-Yu Liao, Chun-Han Lin, Hao-Tsung Chen, Chia-Ying Su, Charng-Gan Tu, Yean-Woei Kiang, and C. C. Yang, "Anti-reflection behavior of a surface Ga-doped ZnO nanoneedle structure and the controlling factors," Optical Materials Express, Vol. 7, No. 11, pp. 4058-4072, 1 November 2017.
2. Chia-Ying Su, Meng-Che Tsai, Keng-Ping Chou, Hsin-Chun Chiang, Huang-Hui Lin, Ming-Yen Su, Yuh-Renn Wu, Yean-Woei Kiang, and C. C. Yang, "Method for enhancing the favored transverse-electric-polarized emission of an AlGaN deep-ultraviolet quantum well," Optics Express, Vol. 25, No. 22, pp. 26365-26377, 30 October 2017.
3. Chia-Ying Su, Chun-Han Lin, Yu-Feng Yao, Wei-Heng Liu, Ming-Yen Su, Hsin-Chun Chiang, Meng-Che Tsai, Charng-Gan Tu, Hao-Tsung Chen, Yean-Woei Kiang, and C. C. Yang, "Dependencies of surface plasmon coupling effects on the p-GaN thickness of a thin-p-type light-emitting diode," Optics Express, Vol. 25, No. 18, pp. 21526-21536, 4 September 2017.
4. Chia-Ying Su, Charng-Gan Tu, Wei-Heng Liu, Chun-Han Lin, Yu-Feng Yao, Hao-Tsung Chen, Yuh-Renn Wu, Yean-Woei Kiang, and C. C. Yang, "Enhancing the hole-injection efficiency of a light-emitting diode by increasing Mg doping in the p-AlGaN electron-blocking layer," IEEE Transactions on Electron Devices, Vol. 64, No. 8, pp. 3226-3233, August 2017.
5. Hao-Tsung Chen, Chia-Ying Su, Charng-Gan Tu, Yu-Feng Yao, Chun-Han Lin, Yuh-Renn Wu, Yean-Woei Kiang, and C. C. Yang, "Combining high hole concentration in p-GaN and high mobility in u-GaN for high p-type conductivity in a p-GaN/u-GaN alternating-layer nanostructure," IEEE Transactions on Electron Devices, Vol. 64, No. 1, pp. 115-120, January 2017.
6. Xu Zhang, Charng-Gan Tu, Yean-Woei Kiang, and C. C. Yang, "Structure variation of a sidewall quantum well on a GaN nanorod," Nanotechnology, Vol. 28, No. 4, p. 045203, 27 January 2017.
7. Chun-Han Lin, Charng-Gan Tu, Yu-Feng Yao, Sheng-Hung Chen, Chia-Ying Su, Hao-Tsung Chen, Yean-Woei Kiang, and C. C. Yang, "High Modulation Bandwidth of a Light-emitting Diode with Surface Plasmon Coupling," IEEE Transactions on Electron Devices, Vol. 63, No. 10, pp. 3989-3995, October 2016.
8. Chia-Ying Su, Chun-Han Lin, Pei-Ying Shih, Chieh Hsieh, Yu-Feng Yao, Charng-Gan Tu, Hao-Tsung Chen, Horng-Shyang Chen, Yean-Woei Kiang, and C. C. Yang, "Coupling Behaviors of Surface Plasmon Polariton and Localized Surface Plasmon with an InGaN/GaN Quantum Well," Plasmonics, Vol. 11, No. 3, pp. 931-939, June 2016.
9. Charng-Gan Tu, Chia-Ying Su, Che-Hao Liao, Chieh Hsieh, Yu-Feng Yao, Hao-Tsung Chen, Chun-Han Lin, Chi-Ming Weng, Yean-Woei Kiang, and C. C. Yang, "Regularly patterned multi-section GaN nanorod arrays grown with a pulsed growth technique," Nanotechnology, Vol. 27, No. 2, p. 025303, 15 January 2016.
10. Yu-Feng Yao, Chun-Han Lin, Chieh Hsieh, Chia-Ying Su, Erwin Zhu, Shaobo Yang, Chi-Ming Weng, Ming-Yen Su, Meng-Che Tsai, Shang-Syuan Wu, Sheng-Hung Chen, Charng-Gan Tu, Hao-Tsung Chen, Yean-Woei Kiang, and C. C. Yang, "Multi-mechanism efficiency enhancement in growing Ga-doped ZnO as the transparent conductor on a light-emitting diode," Optics Express, Vol. 23, No. 25, pp. 32274-32288, 14 December 2015.
11. Yang Kuo, Wen-Yen Chang, Chun-Han Lin, C. C. Yang, and Yean-Woei Kiang, "Evaluating the blue-shift behaviors of the surface plasmon coupling of an embedded light emitter with a surface Ag nanoparticle by adding a dielectric interlayer or coating," Optics Express, Vol. 23, No. 24, pp. 30709-30720, 30 November 2015.
12. Chun-Han Lin, Yu-Feng Yao, Chia-Ying Su, Chieh Hsieh, Charng-Gan Tu, Shaobo Yang, Shang-Syuang Wu, Hao-Tsung Chen, Yean-Woei Kiang, and C. C. Yang, "Thermal annealing effects on the performance of a Ga-doped ZnO transparent-conductor layer in a light-emitting diode," IEEE Transactions on Electron Devices, Vol. 62, No. 11, pp. 3742-3749, November 2015.
13. Chun-Han Lin, Chung-Hui Chen, Yu-Feng Yao, Chia-Ying Su, Pei-Ying Shih, Horng-Shyang Chen, Chieh Hsieh, Yang Kuo, Yean-Woei Kiang, and C. C. Yang, "Behaviors of surface plasmon coupled light-emitting diodes induced by surface Ag nanoparticles on

dielectric interlayers," Plasmonics, Vol. 10, No. 5, pp. 1029-1040, October 2015.

14. Yang Kuo, Chia-Ying Su, Chieh Hsieh, Wen-Yen Chang, Chi-An Huang, Yean-Woei Kiang, and C. C. Yang, "Surface plasmon coupling for suppressing p-GaN absorption and TM-polarized emission in a deep-UV light-emitting diode," Optics Letters, Vol. 40, No. 18, pp. 4229-4232, 15 September 2015.
15. Charng-Gan Tu, Yu-Feng Yao, Che-Hao Liao, Chia-Ying Su, Chieh Hsieh, Chi-Ming Weng, Chun-Han Lin, Hao-Tsung Chen, Yean-Woei Kiang, and C. C. Yang, "Multi-section core-shell InGaN/GaN quantum-well nanorod light-emitting diode array," Optics Express, Vol. 23, No. 17, pp. 21919-21930, 24 August 2015.
16. Charng-Gan Tu, Chia-Ying Su, Che-Hao Liao, Chieh Hsieh, Yu-Feng Yao, Hao-Tsung Chen, Chun-Han Lin, Horng-Shyang Chen, Yean-Woei Kiang, and C. C. Yang, "Regularly-patterned Nanorod Light-emitting Diode Arrays Grown with Metalorganic Vapor-phase Epitaxy," Superlattices and Microstructures, Vol. 83, pp. 329-341, July 2015. **(Invited)**
17. Chun-Han Lin, Chia-Ying Su, Erwin Zhu, Chieh Hsieh, Charng-Gan Tu, Yu-Feng Yao, Hao-Tsung Chen, Che-Hao Liao, Horng-Shyang Chen, Yean-Woei Kiang, and C. C. Yang, "Thermally induced variations of strain condition and emission behavior in flat and bendable light-emitting diodes on different substrates," Optics Express, Vol. 23, No. 12, pp. 15491-15503, 15 June 2015.
18. Yu-Feng Yao, Charng-Gan Tu, Ta-Wei Chang, Hao-Tsung Chen, Chi-Ming Weng, Chia-Ying Su, Chieh Hsieh, Che-Hao Liao, Yean-Woei Kiang, and C. C. Yang, "Growth of Highly Conductive Ga-doped ZnO Nanoneedles," ACS Applied Materials & Interfaces, Vol. 7, No. 19, pp. 10525-10533, 20 May 2015.
19. David C. Look, Eric R. Heller, Yu-Feng Yao, and C. C. Yang, "Significant mobility enhancement in extremely thin highly-doped ZnO films," Applied Physics Letters, Vol. 106, No. 15, p. 152102, 13 April 2015.
20. Chun-Han Lin, Chia-Ying Su, Erwin Zhu, Yu-Feng Yao, Chieh Hsieh, Charng-Gan Tu, Hao-Tsung Chen, Yean-Woei Kiang, and C. C. Yang, "Modulation behaviors of surface plasmon coupled light-emitting diode," Optics Express, Vol. 23, No. 6, pp. 8150-8161, 23 March 2015.
21. Charng-Gan Tu, Che-Hao Liao, Yu-Feng Yao, Horng-Shyang Chen, Chun-Han Lin, Chia-Ying Su, Pei-Ying Shih, Wei-Han Chen, Erwin Zhu, Yean-Woei Kiang, and C. C. Yang, "Regularly patterned non-polar InGaN/GaN quantum-well nanorod light-emitting diode array," Optics Express, Vol. 22, No. S7, pp. A1799-A1809, 15 December 2014.
22. Duanjun Cai, Na Lin, Hongmei Xu, Che-Hao Liao, and C. C. Yang, "Extraordinary N atom tunneling in formation of InN shell layer on GaN nanorod m-plane sidewall," Nanotechnology, Vol. 25, No. 49, p. 495705, 12 December 2014.

Invited presentations at international conferences:

1. "Orientation and Polarity of Transparent Conductive Ga-doped ZnO Nanoneedle and Its Application to Solar Cell Anti-reflection," The 18th International Conference of the Union of Materials Research Societies in Asia (IUMRS-ICA 2017), Taipei, Taiwan, November 5-9, 2017.
2. "Surface Plasmon Coupled Light-emitting Diodes," The 8th Asia-Pacific Workshop on Widegap Semiconductors (APWS 2017), Qingdao, China, September 24-27, 2017.
3. "Growth of Ga-doped ZnO Nanowires and Their Applications," The 26th Annual Meeting of MRS-J (2016), Yokohama Port Opening Plaza, Yokohama, Japan, December 19-22, 2016.
4. "Surface Plasmon Resonance Behaviors of Gold Nanoring and Their Application to Photothermal and Photodynamic Therapies," The 7th International Conference on Metamaterials, Photonic Crystals and Plasmonics (META'16), Torremolinos (Malaga), Spain, July 25-28, 2016.
5. "Fabrication of Multi-section Nanorod Light-emitting Diode Arrays," 2016 IEEE Photonics Society Summer Topicals Meeting on Nanowire Optoelectronics, Newport Beach Marriott Hotel & Spa, Newport Beach, CA, USA, July 11-13, 2016.
6. "Broad emission spectra of multi-section core-shell InGaN/GaN quantum-well nanorod light-emitting diode arrays," Photonics West 2016, San Franscico, US, February 13-18, 2016.
7. "Growth of highly conductive Ga-doped ZnO and its applications," Photonics West 2016, San Franscico, US, February 13-18, 2016.

8. “Simulation study on surface plasmon coupled light-emitting diode,” The 15th International Conference on Numerical Simulation of Optoelectronic Devices (NUSOD), Taipei, Taiwan, September 7-11, 2015.
9. “Nanostructured light-emitting diodes,” The 11th International Conference on Nitride Semiconductors (ICNS-11), Beijing, China, August 31-September 5, 2015.
10. “Nitride Light-emitting Diode Grown on Patterned Si (110) Substrate,” The International Conference on Materials for Advanced Technologies, ICMAT 2015, Singapore, June 28-July 3, 2015.
11. “MOCVD growth of III-nitride core-shell-structured nanorod with flexible geometry,” ISPlasma 2015, Nagoya, Japan, March 26-31, 2015.
12. “Regularly patterned non-polar InGaN/GaN quantum-well nanorod light-emitting diode array,” Photonics West 2015, San Francisco, US, February 7-12, 2015.
13. “Surface Plasmon Coupled Light-emitting Diode,” OSA Light, Energy and the Environment Conference, Canberra, The Australian Capital Territory, Australia, December 2-5, 2014.
14. “Development of Nitride Nanorod Light-emitting Diode Array,” AVS 61st International Symposium and Exhibition (AVS-61), Baltimore, US, November 9-14, 2014.

Collaborations with AFRL (Dr. Kent Averett):

(1) Delivering GaN nanorod and GaZnO nanoneedle samples to the collaborator at AFRL/RXAP, Dr. Kent Averett.
(2) Meeting with Dr. Kent Averett at the four conferences for discussions of collaborating research, including the results and future work.
(3) Receiving SiC substrates of Si and C faces from Dr. Kent Averett.
(4) Receiving nano-imprint stamps from Dr. Kent Averett.